DELFT UNIVERSITY OF TECHNOLOGY

MASTER THESIS

A Dynamic Multilevel Multiscale Framework for Accurate and Efficient Simulation of CO_2-Brine Multiphase Flow in Heterogeneous Porous Media

---

Author:
Jeroen RIJNTJES

Supervisors:
Dr. Hadi HAJIBEYGI
Matteo CUSINI

A thesis submitted in fulfillment of the requirements
for the degree of ***Master of Science***

in

Applied Earth Sciences

to be defended publicly on
Friday July 13, 2018

A Dynamic Multilevel Multiscale Framework for Accurate and Efficient Simulation of CO_2-Brine Multiphase Flow in Heterogeneous Porous Media

by

J.C. Rijntjes

to obtain the degree of Master of Science
at the Delft University of Technology,
to be defended publicly on Friday 13th of July.

Student number:	4180348	
Project duration:	July 1, 2017 – July 13, 2018	
Thesis committee:	Dr. H. Hajibeygi,	TU Delft, Advisor
	Prof. dr. ir. C. Vuik,	TU Delft, Committee member
	Dr. ir. O. Leeuwenburgh	TU Delft - TNO, Committee member
	Dr. S.Y.F. Vincent-Bonnieu	TU Delft - Shell, Committee member

This thesis work is performed at Delft Advanced Reservoir Simulation (DARSim) group.

This thesis is confidential and cannot be made public until July 13, 2018

TU Delft

Abstract

One of the most important challenges facing academic, industrial and policy-making sectors is meeting with the increasing energy demand while preserving the affordability of the energy and maintaining the quality of the planet earth (including the environment, specially by reducing its greenhouse gas footprint). This global challenge demands for exploiting the subsurface formations as giant storage space for industrial by products, e.g., CO_2, while a future utilisation is found for them. Exploitation of subsurface formations for CO_2 storage depends on our capacity to "accurately" and "efficiently" simulate the multiphase nonlinear flow in heterogeneous large-scale natural formations. An accurate and efficient simulation would allow for proper predictive understanding for several operational aspects including: (1) capacity of the storage; (2) life-time long behaviour of the injected CO_2 in the subsurface formation, and (3) safety and integrity of the capturing procedure. The challenge of extreme scale dissimilarity between the heterogeneous coefficients (rock conductivity and fluid physics, e.g., mixing) and the reservoir has been known in the scientific literature as one of the main simulation challenges. Classically, to resolve this mismatch, reservoir models have been excessively upscaled to a resolution which can be solved affordably with the state-of-the-art commercial-grade simulators. However, as the rapid extension of the computational capacity, as well as the newly developed multiscale scalable nonlinear solvers, one needs to revisit our simulation frameworks to provide a scalable (to field scale) and accurate CO_2 simulation framework. This thesis work focuses on extension of the recently developed Algebraic Dynamic Multilevel Method (ADM) to highly-nonlinear simulations of CO_2-Brine multiphase flow problems. ADM maintains simulation scalability by imposing fine-scale grids only where needed; and imposing coarser grids paired with accurate prolongation operators far from the sub-domains with sharp gradients. In this work, to provide a systematic study, the developed ADM framework is formulated such that it allows for both multiscale-based basis functions and also upscaling-based procedure. This is crucially important as it reveals how the "solution-based" interpolations based on fine-scale heterogeneity can impact the simulation results; compared with the "effective-coefficient-based" approach.

In brief, the novelty and contribution of this research is two fold: (1) development of a multiscale-based ADM method for CO_2-Brine simulator and (2) systematic study to find the best model order reduction strategy when it comes to complex multiphase characteristics and rock heterogeneity. Two different classes of simulations are studied: (1) injection and evolution of the injected CO_2 phase into the brine with capillary effects; and (2) miscible mixing process in which resolving front fingers into the residing less-mobile fluid imposes computational challenges. The study, as such, intends to reveal the details in "upscaling-based" vs. "multiscal-based" approach; and tends to provide a generic framework in which the scalability of the simulations are preserved by employing fine-scale grids only where and when needed.

Several challenging sensitivity analysis are performed in which fine-scale solutions are compared with the multi-scale ADM and upscaling ADM solutions for immiscible and miscible fluid flow displacement. From these numerical experiments can be concluded that Multiscale-ADM outperforms the Upscaling-based ADM approach. More precisely with similar active grid cells, it provides a more accurate simulation method. As such, Multiscale-ADM casts a promising approach for next-generation simulators for CO_2-Brine systems.

Acknowledgement

By presenting this thesis an end comes to a period in my life to which I look back with great joy. In this acknowledgement I would like to thank everyone that helped me throughout this unforgettable period and some people in specific.

Dear Dr. H. Hajibeygi, dear Hadi, in the first year of the master during the course Rock Fluid Physics you enhanced my knowledge and interest for the physics related to fluid flow in the subsurface. Your passion and enthusiasm during the lectures were a great inspiration. During the process of coming to the results presented in this thesis your creativity and willingness to help in times of need is of an unmatchable degree of kindness. Besides your strengths in teaching Rock Fluid Physics and Reservoir Simulation, the lessons you thought me how reservoir simulations can be related to life lessons are memories I will cherish. Relating reservoir simulation to flying air planes, running businesses and even how Sir Alex Ferguson managed his football team are lessons I will not forget. During this period I asked a great amount of your patience which you always returned with fruitful discussions and interesting insights, because of this I have the utmost confidence that you will make a great father!

Secondly, I would like to take this opportunity to thank Matteo Cusini for all the support related to implementation of the code. During the periods in Delft regardless of your own busy schedule you always made time for questions to this thesis. Even during your stay in California sessions over skype or whatsapp where easily arranged irrespective of the different time-zones. Thank you for everything.

Lastly, I would like to thank all my friends and family that supported me throughout this process. It helped me a lot coming to these results and finishing the report. It has been a memorable journey and I am very excited what the future holds for all of us.

Thank you,

J.C. Rijntjes
Delft, 13-07-2018

Contents

List of Figures

List of Tables

1

Introduction

Climate change is seen as one of the most important challenges of the coming century. In 2015 the United Nations Framework Climate Change Convention (UFCCC) set up the Paris agreement which stated that the global temperature increase should be kept well below a 2°C increase compared to pre-industrial levels with the target temperature set at 1.5°C. Besides the goals on temperature control, the agreement also set a long-term goal to realize a net zero emission society. Net zero emission refers to the idea of being carbon neutral and thus balancing the emission of carbon emission released into the atmosphere with the amount sequestered or offset. The net zero emission society should be reached by 2050 [30].

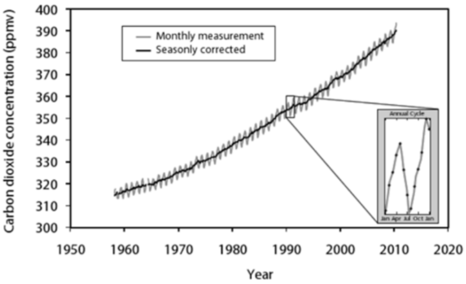

Figure 1.1: CO_2 increase over the last 60 years [16].

Capturing and long term storage of carbon dioxide (CO_2) in the subsurface is seen as a possible and much needed method to reduce the amount of greenhouse gasesin the atmosphere and to slow down and if possible reverse the climate change occurring. CO_2 accounts for 76% of the greenhouse gases emitted yearly [27]. In the past years great improvements have been made with respect to the technical knowledge about carbon capture and storage (CCS) . However, the public opinion is not developing in the same positive direction; skepticism dominates the public opinion. When zooming in on the Netherlands to understand the skepticism, the obvious conclusion can be drawn that the induced seismicity in northern Netherlands due to gas production is an important cause for the negative public opinion [7]. The public opinion is of utter importance when being opposed to CCS projects, an example is a project by Shell in Barendrecht where storage of CO_2 was planned in depleted gas reservoirs. Due to a lack of local support the project found so much resistance that the government canceled it. The lack of communication and not being able to convince the public that storage of CO_2 can be assured played a significant role [4, 10].

Improvements in numerical simulations will enhance the understanding of CO_2 behavior during injection and storage in the subsurface. Due to more accurate numerical simulation results CCS projects will become explainable and understandable for all different stakeholders. Besides the knowledge gap that will be crossed more easily, numerical simulations will be important during operations of a CCS project. Because of the relevance of accurate numerical models in this research the industry-used flow-based upscaling method is put into a dynamic multilevel framework, yet being tested against the newly developed multi-scale-based dynamic grid framework. Secondly, complex mixing dynamics on small scale will be introduced in the state-of-the-art in-house Matlab simulator DARSim2 [6]. This is done to capture and investigate all effects of fluid dynamics occurring during injection in field scale reservoirs. DARSim2 is based on an algebraic dynamic multilevel (ADM) fully-implicit simulation strategy for multiphase flow [6].

Simulation of field-scale reservoirs require significant amount of computational effort. To decrease the number of degrees of freedom, the detailed reservoir properties are often times excessively upscaled to effective "coarse-scale" reservoir properties at lower resolutions. The loss of detail of reservoir properties is a problem and has a big impact on the reliability of the solutions, and thus the operational decisions. In figure 1.2 the effect of decreasing the resolution can be observed. In the left column the saturation (volume fraction of the injected gas) is shown, while the right column depicts the "static-grid-based" permeability used to acquire this solution. There can be concluded that upscaling increases the error significantly, when applied in the global domain. In this thesis two methods are developed to investigate a next-generation framework, where (1) dynamic multilevel resolution is imposed during the simulation in order to capture the fronts and (2) a multiscale-ADM approach is developed to map the unknowns accurately across different scales. In addition, the developed multiascale-ADM method is compared with upscaling-based ADM approach to investigate the importance of the coarse-to-fine mapping procedure.

The philosophy behind the tested methods (upscaling vs multiscale based ADM) is to resolve the fine-scale permeability only at relevant locations such as the saturation front. The purpose of dynamically choosing where to use fine-scale simulations is to reduce the error in the results, at the same time obtain efficient simulations. Places of reduced interest such as where the saturation front has not reached yet can be solved on a coarser resolution, and as soon as the saturation front reaches this location the fine-scale problem can be solved to maintain accuracy and minimise loss of detail.

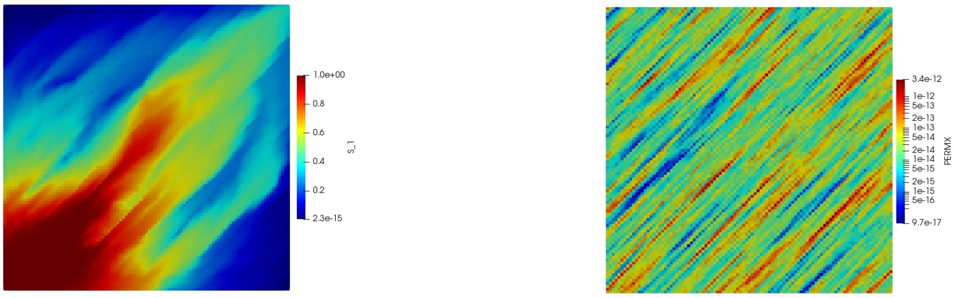

(a) Fine-scale saturation, 99x99 resolution

(b) Fine-scale permeability, 99x99 resolution

(c) Upscaled level 1 saturation, 33x33 resolution

(d) Upscaled level 1 permeability, 33x33 resolution

(e) Upscaled level 2 saturation, 33x33 resolution

(f) Upscaled level 2 permeability, 11x11 resolution

Figure 1.2: Fine-scale, level 1 and level 2 saturations and permeabilities.

1.1. The process of CCS

To store CO_2 in the subsurface, the process starts with capturing the CO_2. The capturing of CO_2 is often performed at centralized sources emitting constant vast volumes such as power and industrial sites. Power and industrial sites account for approximately 60% of the total CO_2 emission from the Organisation for Economic Co-operation and Developement (OECD) countries [14]. When focussing on the Netherlands these areas can be found in the harbour of Rotterdam or the steel production site of Tata Steel in IJmuiden. There are three main approaches of capturing CO_2: pre-combustion, oxy-fuel combustion and post-combustion. When captured, the CO_2 can be transported to the injection site in three phases: gas, liquid and solid. Transport is performed mostly by using pipelines, tanks and ships[24]. Because of the importance of reducing greenhouse gases in the atmosphere a variety of storage possibilities are being investigated. CO_2 storage is possible in deep saline aquifers, depleted oil and gas reservoirs or unminable coal seams. This research will focus on the storage in saline aquifers because of the worldwide availability and often being located in the same region as the emission sites [24]. Saline aquifers are characterized by brine filling up the pore space in between the grains. The top of the saline aquifer can be covered by a cap-rock which is impermeable to CO_2. Due to buoyancy forces when CO_2 is injected it will rise to the top of the reservoir, the cap-rock will prevent the CO_2 from migrating further vertically [3]. These reservoirs will be investigated because of the relevance of fine-scale physics on numerical simulations. The fine-scale physics have significant influence on the migration of the CO_2 plume through the reservoir; and on its life-time post-injection behaviour. The physics occurring during injection of CO_2 will be described in chapter 2.

1.2. Simulations

In this section an introductory assessment will be given about the various types of reservoir simulation. The goal of this paragraph is to get the reader acquainted with basic understanding of simulation strategies used in computational geo-sciences. The simulation of storage of CO_2 in the sub-surface is a computational challenge. The migration of CO_2 in saline aquifers is complex both in space and time aspects, as the formations span kilometres of length and several hundred meters in height while the geophysical properties of the reservoir are highly heterogeneous. Besides highly heterogeneous properties of the reservoir, the CO_2-brine interaction in the reservoir is of great importance to understand and to predict the migration of the CO_2 in the sub-surface. Furthermore, understanding different physical processes at their relevant time scales impose simulation times which are not only a few days long but targeted to predict the CO_2 dynamics over decades and centuries.

When injecting CO_2 in the sub-surface it will be often times in super-critical state. Super-critical is the state when a gas is at high pressure and temperature. The CO_2 when being in super-critical state is highly mobile and can easily travel great distances. When injecting CO_2 in aquifers there is often a difference in depth and thus resulting in a tilted reservoir layer in which the CO_2 is injected. The highly mobile state of the CO_2 and the difference in density between the CO_2 and the resident-brine result in gravity segregation, causing the raise of the CO_2-plume while being injected deep in the reservoir. In figure 1.3 a picture of a CO_2-plume is shown. On the top left side of the figure the instabilities occurring during migration in brine are shown. The occurrence of these viscous fingers at the displacement front are investigated in chapter 6 in a miscible displacement setting. The method most frequently used to simulate this vertical movement of CO_2 and to maintain minimal errors in the simulation results is the vertical-equilibrium approach. As the name implies, the main assumption in this simulation strategy is the presence of vertical equilibrium for the flow system. The vertical-equilibrium approach is especially useful in situations in which gravity segragation due to large density differences is present, such as during super-critical CO_2 injection in brine [21, 26]. Furthermore, vertical equilibrium is a useful method to decrease the degrees of freedom in the vertical dimension. During the vertical equilibrium-approach the mass conservation and velocity equations are vertically averaged to obtain vertical equilibrium [25].

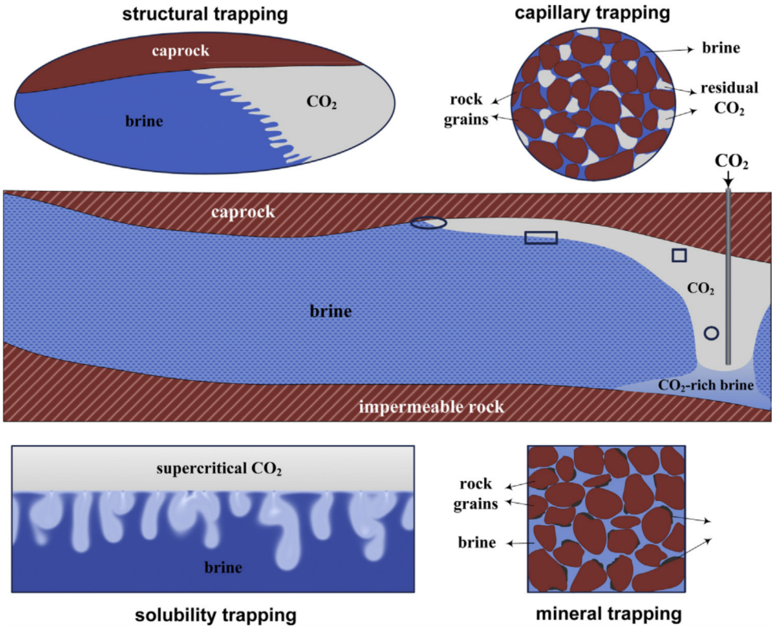

Figure 1.3: CO_2-plume developed during injection into brine [9].

Reservoirs in which sequestration of CO_2 will be performed can be of considerable dimensions, possibly spanning several kilometers in horizontal directions and tens to hundreds of meters in vertical length. Besides the immense scales in space, reservoirs are usually highly heterogeneous, implying large contrasts in geological properties such as permeability and porosity changing over small intervals. This level of detail over many spatial scales, pore-scale (micrometers to millimetres) to formation-scale (kilometres), exceeds the current computational power available and needed for reservoir simulations that take this level of detail into consideration. Besides varying spatial scales with respect to geological properties, complex physical processes such as viscous fingering [12] also take place at different scales. A trade off needs to be made between the level of detail taken into account and the enhancement of computational efficiency and cost. A technique used traditionally in reservoir simulation is flow-based upscaling fine-scaled properties to find properties at the grid sizes that can be treated efficiently by reservoir simulators. The goal of upscaling is to reduce the number of degrees of freedom, however the downside of upscaling is the loss of information and thus their reliability is under question [15].

In order to reduce the computational difficulties for large problems with spatially varying properties, multi-scale simulation strategies have been developed for fluid flow problems [15]. During multi-scale simulations global fine-scale properties are considered when developing a coarse-scale grid of several local problems used for simulations [33]. After simulations the coarse-scale results are reversely mapped to the fine-scale grid in order to maintain numerical accuracy and limit the loss of information. The usage of multi-scale simulation is useful in computational fluid dynamics because it is based on the laws of conservation of mass regarding fluid flow.

During a multi-level simulation strategy instead of solving a single coarse grid level, multiple levels of coarsening grids are used during simulation. A multi-level simulation strategy helps because it is able to solve larger problems (several millions to billions unknowns) compared to a multi-scale strategy (million unknowns) [6].

1.2.1. ADM & Upscaling

Simulation strategies has been advanced to rely less and less on the upscaling quantities by enhancing the computational efficiency using high grid resolutions only at places where and when necessary. Places of interest during simulation are, e.g., around the injection and production wells, and the location of the saturation front and complex reservoir geometries [13]. This strategy is called adaptive mesh refinement or dynamic local grid refinement (DLGR). The main goal of this strategy is to reduce the total amount of active fine-scale grid cells during simulation, and specify them to the locations of relevance. ADM is a newly state-of-the-art simulation strategy extending previous known mesh refinement strategies to fully-implicit simulations. During ADM the grid resolution is automatically determined on the basis of coarsening criterion set by an absolute threshold value determining the maximum saturation difference between the current cell and the four surrounding cells [6]. The difference however with the existing flow-based upscaling methods is that it maintains the fine-scale heterogeneities (instead of upscaling them) while it solves the system at multi-level dynamic grid resolution.

1.3. Research goals

The following research goals have been established.

- Develop a multiscale-based ADM approach for CO_2-brine multiphase flow system.
- Develop an upscaling-based ADM simulator (i.e., utilise flow-based upscaling within the dynamic grid framework) for CO_2-brine multiphase flow system.
- Investigate the performances of the multi-scale and upscaling-based ADM approaches (comparative study).
- Study how these two methods perform for mixing process; which takes place also in CO_2-brine systems.

1.4. Thesis layout

The physical background will be extensively reviewed in chapter 2. Two different subjects will be thoroughly examined, namely: the pore-scale physics and field-scale physics. In chapter 3 the governing equations on which the simulator is based will be discussed, followed by the numerical model used. After which in chapter 5 the simulation results on the synthetic data set will be discussed, in which a sensitivity study on various parameters is included. In chapter 6 the simulator is benchmarked in a miscible displacement setting in which complex mixing phenomena occur, both in homogeneous and heterogeneous media. In chapter 7 and chapter 8 the conclusions of the results are presented and possibilities regarding future work are investigated.

All the studies presented here are implemented in DARSim2 simulator; and can be used by the future students for further studies.

2

Theoretical Background

In this chapter the theory behind the process of CO_2 sequestration will be discussed briefly. Firstly the physical background of subsurface storage of CO_2 will be discussed. Subsequently an in depth review of the methodology of flow-based upscaling and multiscale based ADM will be presented.

2.1. Trapping mechanisms

In this section the general subsurface trapping mechanisms of CCS will be discussed. The mechanisms discussed are: structural trapping, residual trapping, solubility trapping and mineral trapping.

- **Structural Trapping:** When CO_2 is injected into a reservoir which is overlain by an impermeable to CO_2 cap-rock, the CO_2 is contained by a physical barrier. Due to buoyancy forces the CO_2 will migrate upwards until it is stopped by the impermeable layer. In 2.1 both structural trapping mechanisms are depicted.

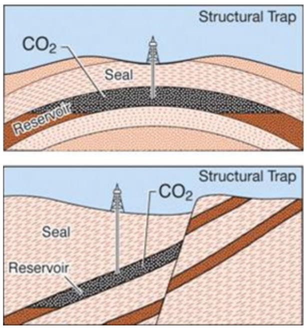

Figure 2.1: Structural trapping mechanisms, respectively [1].

- **Residual Trapping:** Residual trapping, often also called capillary trapping. During this process injected CO_2 is immobilized in the pore-space (void space between grains) while being surrounded by brine. Trapping occurs due to fluid physics and interfacial forces [19]. The CO_2 is immobilized during upward migration of the plume.

- **Solubility Trapping** During flow of CO_2 through the reservoir it partially dissolves into the brine that initially occupies the pore space. The dissolving process occurs due to mixing. When CO_2 is dissolved into the formation fluid upward migration is stopped due to the difference in density reducing the buoyancy [22].

- **Mineral Trapping** Lastly, the fourth trapping mechanisms is mineral trapping. This trapping mechanisms depends on the reaction between CO_2 and the reservoir rock causing the formation of minerals. This trapping mechanisms relies on geo-chemical reaction and thus a considerable timespan should be taken into account for this type of trapping [34].

In this thesis the influence of capillarity and mixing on the performance of upscaling-based ADM and multiscale-based ADM are examined. Mineral trapping and structural trapping are considered to be outside the scope of this research.

2.2. Pore-scale physics

After the previous general overview of trapping mechanisms a close up of pore-scale fluid phenomena occurring during CCS will be given.

2.2.1. Drainage & imbibition

Throughout injection and migration of CO_2 inside a saline reservoir the process is characterized by drainage and imbibition processes. Drainage occurs when the CO_2 displaces the brine resulting in a decreasing brine saturation. Imbibition is the opposite of this process, water fills up the pores previously occupied by CO_2 [5, 8].

2.2.2. Wetting properties during multiphase flow

During CO_2 injection the CO_2 displaces the brine, through out this process CO_2 is assumed to be the non-wetting fluid and the brine is the wetting fluid. Wettability indicates whether the reservoir rock is hydrophilic or hydrophobic to a specific phase, thus indicating the preference to bond or to repulse the respective fluid. During injection at the displacement front drainage takes place when the non-wetting fluid displaces the wetting fluid (decreasing water saturation), at the trailing edge of the CO_2 plume imbibition occurs (increasing water saturation).

2.2.3. Relative permeability

Relative permeability describes the level of interaction in a multiphase system while migrating through the reservoir, in this case between CO_2 and brine. During multiphase flow the presence of a second fluid creates resistance against flow of the other fluid. Relative permeability is described as the ratio of effective permeability of a phase to the permeability of the reservoir rock. The relative permeability usually increases with increasing saturation of the respective phase, and can be stated as

$$k_{r,i} = \frac{k_i}{k}, \tag{2.1}$$

where k_i and k are the effective and absolute permeabilities. Relative permeability curves are often obtained from laboratory experiments. Concluded from these experiments is that relative permeability is strongly depended on surface tension (capillarity) [20]. Without the presence of capillary forces, viscous forces would dominate the flow and the result would be two symmetrical curves intersecting at 50% saturation. When the influence of decreasing the wettability of a strongly wetting phase, the intersection point of the relative permeability curves in figure 2.2a will move to the left. If the influence of capillary pressure increases, in case of a lower capillary number, the relative permeability curves become straight lines.

During the numerical experiments performed two types of relative permeabilities where used. In the case of immiscible displacement quadratic relative permeabilities have been used, displayed in figure 2.2a. When performing the numerical experiments in a miscible displacement setting linear relative permeabilities have been used, depicted in figure 2.2b. Due to absence of surface forces in a miscible displacement, linear relative permeability curves can be used.

The capillary number can be found as

$$N_c = \frac{q\mu}{\gamma}, \tag{2.2}$$

where q is the flow-rate, μ is the viscosity of CO_2 and γ is the interfacial tension between the injected and resident fluid.

2.2.4. Capillary pressure

During multiphase flow in porous media the reservoir acts as a capillary system, meaning that the overall system is dominated by hydrostatic, gravity and capillary forces [8]. Capillary pressure (P_c) is the interfacial tension (σ) (mN m^{-1}) between two fluids and the contact angle (θ) measured in the wetting fluid phase. The pressure difference between the wetting and non-wetting phase is a result of the interfacial tension which describes the energy at the interface between the phases [2], this pressure is also known as capillary pressure.

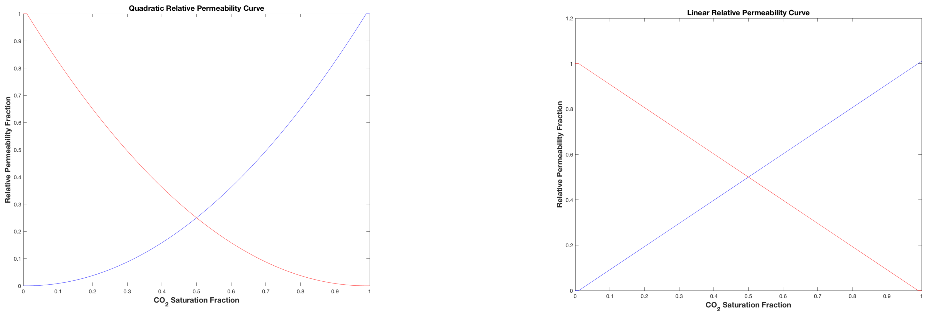

(a) Quadratic relative permeability.

(b) Linear relative permeability.

Figure 2.2: Relative permeability curves used during simulations.

Residual trapping is a result of capillary forces interacting between the injected CO_2 and brine resulting in immobilization of CO_2. An important property influencing this process is relative permeability.

The capillary pressure at pore-scale can be calculated by Equation 2.3 in which r is the radius.

$$p_{cap} = \frac{2\sigma cos(\theta)}{r} \tag{2.3}$$

The capillary pressure function used in the numerical experiments in the Leverett J-function, given by equation 2.4. In this formula p_w is the capillary pressure, S_w is the water saturation, k is the permeability, ϕ is the porosity, γ is the surface tension and θ is the contact angle.

$$J(S_w) = \frac{p_c(S_w\sqrt{k/\phi}}{\gamma\cos\theta} \tag{2.4}$$

2.2.5. Capillary trapping

The process of hysteresis is considered to be the main cause of residual (capillary) trapping. The effect of hysteretic behavior during imbibition (increase of wetting phase saturation) is that the relative permeability of CO_2 (non-wetting phase) can decrease to zero which will result in immobilization of CO_2 in the pore spaces [29]. At pore-scale three physical processes occur influencing the trapping and immobilization of CO_2 namely the piston-like advancement and co-operative pore filling and snap-off.

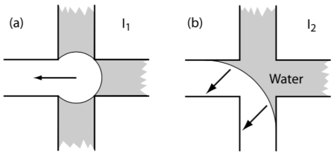

Figure 2.3: Water = grey, CO_2 = white, respectively [31].

Secondly, snap-off occurs by the wetting fluids that remained in the corners and on rough edges during the drainage process. Because the reservoir is water-wet (preferential to wetting phase, see subsection 2.2.2) it is possible that during imbibition the non-wetting phase loses contact with the reservoir rock due to the preference of the reservoir rock to bond with the wetting phase (brine). After which the surrounding pores and throats fill with brine trapping the CO_2 in the pores. The disconnection of blobs of CO_2 from the CO_2 plume remaining behind in pore space is a secondary trapping mechanisms and is extremely influential during the storage of CO_2 [24] [17] [19].

2.3. Field-scale physics

The field-scale processes occurring during CO_2 injection are the following:

- **Advection:** Describes the movement of fluids due to the presence of a pressure gradient. The movement follows the pressure gradient from a high value to a low value.

- **Buoyancy:** Flow movement due to a difference in density is called buoyancy driven, in our case the density difference between the injected CO_2 and the brine.
- **Diffusion:** Diffusive flow is based on a molecular concentration gradient difference from high to low concentration.

In this research diffusion and dispersion effects are investigated in a miscible flow setting during which a homogeneous and heterogeneous case are reviewed.

2.4. Mixing processes

In the first section of this research the developed calculation methods are tested and benchmarked in an immiscible flow displacement setting. In the second complex physics is added to the simulator. This physics includes mixing effects and dispersion. Miscible displacement settings are characterised by viscous fingering effect. As described in [12] the development and onset of instabilities of fluid displacement in porous media are often referred to as viscous fingers. These instabilities are frequently related to variations in viscosity due to mixing of the injected and resident fluid. In the following paragraphs the growth pattern will be discussed, in the next chapter where the governing equations are discussed.

The mechanisms related to the development of instabilities will be discussed in this paragraph. The onset of instabilities is related to the difference in viscosity and density of the injected and resident fluid. In the case being investigated the difference in viscosity is related to the miscibility of the injected fluid in the resident fluid. During the onset of instabilities three stages can be identified in the development, namely: spreading, tip splitting and shielding. Spreading refers to the movement of a lobe in the control volume resulting in instability at the font. Tip splitting occurs when at the tip of a viscous finger, the tip splits in two separate fingers. Subsequently shielding happens referring to the process after splitting when one of the two fingers developed at the tip outgrows the other finger. Shielding happens in the direction of the pressure gradient of the biggest finger, after which the finger outgrows and shields off its neighbouring finger from further growth.

In figure 2.4 the mechanism of spreading, tip splitting and shielding is observable. In the top of figure spreading can be seen, in the second figure tip splitting and in the third and fourth figure shielding can be seen. In the case of miscible displacement the presence of dispersion reduces the development of viscous fingers. The ratio of advective and diffusive transport phenomena is defined by the Péclet number. During field-scale simulations the Péclet number is usually very high, meaning that diffusion effects do not influence the fluid flow. When investigating physics at smaller scale and with low injection rates, specially at the post-injection long-term behaviour of the CO_2, the Péclet number is lower and fluid flow can be influenced by dispersion.

$$Pe = \frac{Advective \quad transport \quad rate}{Diffusive \quad transport \quad rate} \tag{2.5}$$

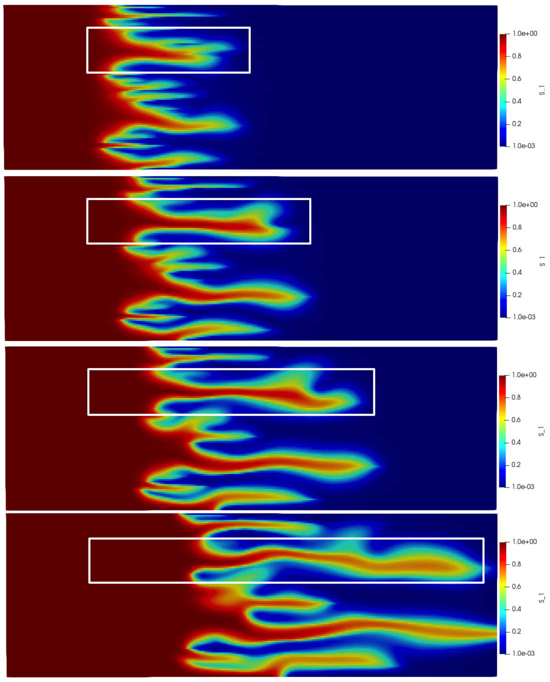

Figure 2.4: Overview of spreading, splitting and shielding of viscous fingers.

2.5. Numerical models

As can be concluded from the brief summary with respect to the physics occurring during CO_2 injection a great variety of processes are relevant to accurately simulate the migration of CO_2. The complexity of this problem increases due to the variety of scales at which these processes take place. As stated in chapter 1 and showed in 1.2 the challenge of reservoir simulation is to capture the fine-scale heterogeneities at the location where the complex physics described above occur. In this research two approaches are being compared: Upscaled-based ADM and ADM. The similarity between both simulation methods is that they solve the fine-scale system at places of high interest suchs as the saturation front. The difference between the two methods is that at places where no significant changes occur in saturation the upscaled-based ADM approach uses an effective permeability value while the multiscale-based ADM uses the fine-scale permeability field through local basis functions. More precisely, in the upscaling-based ADM constant pressure interpolators are used at all levels with flow-based effective permeabilities, while in the ADM method multilevel multi-scale basis functions are employed as the pressure interpolators.

3

Fine-Scale Governing Equations

3.1. Governing equations

The simulator used in this research is based on multi-phase multi-component flow with conservation of mass using Darcy's law, which reads:

$$\frac{\delta}{\delta t}(\phi S_\alpha) - \nabla \cdot (\lambda_\alpha \cdot \nabla p) = q_\alpha \qquad \forall \alpha \in \{1,...,N_{ph}\} \tag{3.1}$$

where ϕ, S_α, λ_α, p and q_α denote the porosity, the saturation and mobility of phase α, the pressure and the volumetric flow rate of the source term. The phase mobility reads, $\lambda_\alpha = \frac{K k_{ra}}{\mu_\alpha}$, where K is the rock permeability, k_{ra} is the relative permeability, and μ_α is the phade viscosity.

Equation 3.1 can be extended to compressible flows if the density is introduced in each term. In addition, mass balance equations are subject to the physical-assumption that the porous medium is filled with fluids, i.e., $\sum_{\alpha=1}^{N_{ph}} S_\alpha = 1$. Overall, this leads to $N_{ph}+1$ equations for $N_{ph}+1$ (N_{ph} saturations and 1 pressure) unknowns.

3.2. Fine-scale fully-implicit simulation framework

The discretization of equation 3.1 is based upon a fully-implicit discretization strategy. During the fully-implicit method the pressure- and saturation- dependent variables are discretized at the next time step $(n+1)$ and the residual $r_\alpha^{n+1}$is zero, which is given by equation 3.2.

$$r_\alpha^{n+1} = \frac{\phi}{\delta t}(S_\alpha^{n+1} - S_\alpha^{n}) - \nabla \cdot (\lambda_\alpha^{n+1} \cdot \nabla p^{n+1}) - q_\alpha^{n+1} = 0 \qquad \forall \alpha \in \{1,...,N_{ph}\} \tag{3.2}$$

Because the residual is non-linear dependent on the primary unknown $(P, S_1 ... S_{N_{ph-1}})$, the first step is to linearize N_{ph} equations of equation 3.2 using the Newton-Lemma procedure, given by equation 3.3. The previous time step is denoted by v and the next time step is given by $v+1$.

$$r^{n+1} \approx r^{v+1} = r^v + \frac{\partial r}{\partial p}\bigg|^v \partial p^{v+1} + \sum_{i=1}^{N_{ph}-1} \frac{\partial r}{\partial S_i}\bigg|^v \partial S_i^{v+1} \tag{3.3}$$

The linear system $\mathbf{J}^v \delta x^{v+1} = r^v$ is obtained and solved until convergence. In which δx denotes the vector of primary unknowns and $\mathbf{J}$ denotes the Jacobian matrix. In a two phase system containing the wetting (w) and non-wetting (nw) phase the linear system is as follows:

$$\underbrace{\begin{pmatrix} J_{nwp}^v & J_{nws}^v \\ J_{wp}^v & J_{ws}^v \end{pmatrix}}_{J^v} \underbrace{\begin{pmatrix} \delta p^{v+1} \\ \delta S^{v+1} \end{pmatrix}}_{\delta x^{v+1}} = - \underbrace{\begin{pmatrix} r_w^v \\ r_{nw}^v \end{pmatrix}}_{r^v} \tag{3.4}$$

The first row of the Jacobian belongs to the non-wetting (nw) phase and the second row to the wetting (w) phase, in which both primary unknowns (pressure and saturation) are represented by one entry per row. In the chapter the multi-scale based ADM and upscaling one are explained in detail. These methods are developed to allow for accurate and field-scale relevant (efficient) simulation.

3.3. Mixing processes during miscible displacement

The system of equations used to describe miscible displacement for two components (brine and solvent) including dispersion in porous media are given by 3.5 and 3.6 [28].

$$\nabla \cdot \underline{u} = q_{brine} + q_s \tag{3.5}$$

$$\phi \frac{\delta c}{\delta t} + \nabla \cdot \left(c\underline{u} \right) - \nabla \cdot \left(\phi \underline{\underline{D}} \Delta c \right) = q_s \tag{3.6}$$

In 3.6 the ϕ is the porosity, t is the time, c is the volumetric concentration of the solvent and q_{brine} and q_s are the source term for the brine and solvent. The Darcy velocity is given by 3.7.

$$\underline{u} = -\frac{\underline{\underline{K}}}{\mu_{mix}} \nabla p \tag{3.7}$$

As stated before the complex physics are related to a miscible displacement, when miscible displacement occurs no interfacial tension between fluids is present. The mixing of fluids is given by the quarter-power mixing rule [18]. The assumption of ideal mixing is made, meaning that no volume change occurs.

$$\mu_{mix}(c) = \left(\frac{c}{\mu_s^{\frac{1}{4}}} + \frac{1-c}{\mu_o^{\frac{1}{4}}} \right)^{-4} \tag{3.8}$$

During simulation the assumption is made that linear flow occurs in the x-direction, resulting in a diagonal dispersion tensor given by 3.9.

$$M = \begin{bmatrix} D_{xx} & 0 \\ 0 & D_{yy} \end{bmatrix} \tag{3.9}$$

In a two dimensional domain the longitudinal Peéclet number is given by 3.10.v In which q_{inj} is the volumetric injection rate, L_x is the length of the simulation domain, A is the crossectional area and the dispersion factor is given by D.

$$Pe_l = \frac{q_{inc} L_x}{A D_{xx}} \tag{3.10}$$

3.4. Error calculation

The accuracy of the simulator is addressed by calculating the error between the fine-scale simulation results and the results of the respective method of calculation (upscaling-based ADM or multiscale-based ADM). The error in the primary variables pressure and saturation is calculated as

$$\epsilon_p(t) = \frac{||p(t) - p_{ref}(t)||_2}{||p_{ref}(t)||_2} \tag{3.11}$$

and

$$\epsilon_S(t) = \frac{||S(t) - S_{ref}(t)||_2}{N_f}, \tag{3.12}$$

respectively. After the evaluation of the error per time-step the average error is calculated as

$$\epsilon_p = mean(\epsilon_p(t)) \tag{3.13}$$

and

$$\epsilon_S = mean(\epsilon_S(t)). \tag{3.14}$$

4

Numerical Models

In this chapter an in-depth review of multiscale-based ADM and upscaling-based ADM will be given.

4.1. ADM

When using the ADM strategy the goal is to reduce the computational costs compared to solving the complete simulation domain with a fine scale simulation strategy. The computational power required is reduced because of mapping linear system 3.4 on a dynamically defined grid. This is done in such a manner that the fine-scale resolution is only required in selective parts of interest of the domain, and in areas of reduced interest the grid resolution is increased. The coarsening ratio (number of fine cells in a single coarse cell) and the number of coarsening levels is predefined before simulation. The number of levels is defined by l ($l \in 0 \cdots n_l l$), which consists of $N_l = N_{lx} \cdot N_{ly}$. A higher value of l represents a coarser grid. The coarsening ratio is given by: $\gamma^l = \gamma_x^l \cdot \gamma_y^l = \frac{N_{fx}}{N_{lx}} \cdot \frac{N_{fy}}{N_{ly}}$.

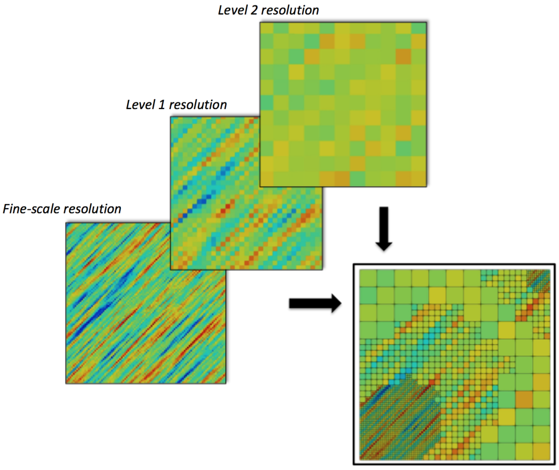

Figure 4.1: 3 levels of static grids, where effective properties are computed based on flow-based upscaling, combined during simulation to a dynamic grid.

During ADM simulations the fine scale solution is calculated by interpolating a coarse level ($l+1$) solution to a fine scale level (l) using a sequence of prolongation operators P_{l-1}^{l}. A serie of restriction operators R_l^{l-1} is used when a fine scale (l) solution needs to be interpolated to a coarser level ($l+1$). The restriction and prolongation operators are given by the block-diagonal matrices 4.1 and 4.2. The method of construction of the prolongation operator is discussed in [32].

$$\mathbf{R}_l^{l-1} = \begin{pmatrix} (R_p)_l^{l-1} & 0 \\ 0 & (R_s)_l^{l-1} \end{pmatrix}_{N_l \times N_{l-1}} \tag{4.1}$$

$$\mathbf{P}^l_{l-1} = \begin{pmatrix} (P_p)^l_{l-1} & 0 \\ 0 & (P_s)^l_{l-1} \end{pmatrix}_{N_{l-1}\times N_l} \tag{4.2}$$

The system of equations given by 3.4 can be calculated for each level given by equation 4.3. To maintain the laws of mass conservation a finite-volume restrictions operator is used for pressure and saturation.

$$\underbrace{R_l^{l-1}\cdots R_1^f J P_f^1 \cdots P_{l-1}^l}_{J_l} \delta x_l = \underbrace{R_l^{l-1}\cdots P_1^f r_f}_{r_l} \tag{4.3}$$

To preserve mass across different scales saturation interpolation is required, this means that the prolongation and restriction operator from coarse to fine and vice versa should have the same effect. This is given by equation 4.4, in which the superscript T indicates the transpose operator.

$$(P_S)^l_{l-1} = (R^{l-1}_l)^T \tag{4.4}$$

4.1.1. ADM procedure

At the start of the ADM simulation the resolution for the multi-level ADM grid is determined. The target areas where a fine solution is required is around the injection and production wells, at the saturation front and around complex geological features that can have significant impact on the flow regime. At areas of reduced interest a coarser grid cell size can be used during simulation. After the determination of grid resolution the ADM coarse system is constructed using a sequence of restriction and prolongation operators, i.e.,

$$\underbrace{\hat{R}_l^{l-1}\cdots \hat{R}_1^f J \hat{P}_f^1 \cdots \hat{P}_{l-1}^l}_{\hat{J}_l} \delta x_l^{ADM} = \underbrace{\hat{R}_l^{l-1}\cdots \hat{R}_1^f r_f}_{\hat{r}_l}, \tag{4.5}$$

where δx_l^{ADM} represents the solution at level l of the ADM grid. The fine scale solution can be then approximated by

$$\delta x_f \approx \delta x'_f = \hat{\mathbf{P}}^1_f \cdots \hat{\mathbf{P}}^l_{l-1}\, \delta x_l^{ADM}. \tag{4.6}$$

Ω^l is defined as the set of all ADM grid cells which are part of level l and the finer levels; and Γ^l is the set containing all cells at level l only. In addition, $\hat{\Pi}^l$ is defined as the collection of all cells within Ω^l that are located at the centre of a coarse node of level l. Therefore,

$$\Gamma^l = \Omega^l \cap \Pi^l. \tag{4.7}$$

For the usage of restriction operator of the sub-blocks in ADM procedure $(\hat{R}_p)^{l-1}_l = (\hat{R}_s)^{l-1}_l$ is valid. The Dirac delta function is represented by $\delta_{i,j}$ in the following conditional expression, i.e.,

$$(\hat{R}_p)^{l-1}_l(i,j) = \begin{cases} (R^{l-1}_p)(i,j) & if\ cell\ i \subset \Omega^l\ and\ cell\ j \subset \Omega^{l-1} \\ \delta_{ij} & otherwise \end{cases} \tag{4.8}$$

The prolongation operator $\hat{\mathbf{P}}^l_{l-1}$ is defined in a similar method, however to reach convergence during simulation one has to preserve the partition of unity. If that is the case the following conditional expression is valid

$$(\hat{P}_p)^l_{l-1}(i,j) = \begin{cases} (P_p)^l_{l-1}(i,j) & if\ cell\ i \subset \Gamma^{l-1}\ and\ cell\ j \subset \Pi^l \\ \delta_{ij} & otherwise \end{cases} \tag{4.9}$$

Because for saturation a constant interpolator is used, it holds that $(\hat{P}_S)^l_{l-1} = ((\hat{R}_S)^l_{l-1})^T$.

4.1.2. ADM grid resolution selection

As stated before the decreased computational power required to perform simulations compared to fine-scale simulations is one of the reasons behind the development of ADM. The decreased computational power is highly depended upon the coarsening of the grid at locations of reduced interest. The obvious conclusion that can be drawn is that the efficiency of ADM highly depends upon the criterion used for grid selection. Various studies have been done on identifying methods for applications of dynamic gridding [23]. In this research the error criterion used is based upon difference in phase saturation between cells, however the ADM simulator is compatible for different forms of criterion.

The procedure for grid resolution selection is based upon a threshold value set by the user for a maximum saturation difference between the considered cell and it's neighboring cells (in a 2D example being four) on the same level (l) and the maximum and minimum of the fine-scale cells ($l-1$) inside the considered coarse cell at level l. If the considered cell satisfies to this criterion it will be displayed in the ADM solution grid. This procedure is depicted in figure 4.2.

For the simulator to maintain accuracy an extra criteria is set to the transition of levels of neighboring cells. The maximum difference in levels between neighboring cells is set to 1. Meaning that the neighbors of the considered grid cell at level l can only be at level l, $l+1$ or $l-1$.

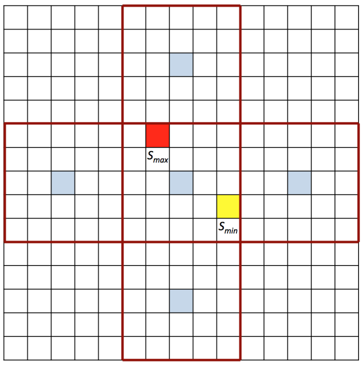

Figure 4.2: ADM coarsening criteria

4.1.3. Multiscale basis functions

To construct the multilevel basis functions, the elliptic (incompressible) part of the full pressure equation is extracted, i.e.,

$$-\nabla \cdot (\lambda \cdot \nabla p) = 0, \tag{4.10}$$

where λ is the mobility tensor at fine-scale resolution.

For a 2D problem to construct the multi-scale basis functions, the first step is to create two sets of coarse grids which are imposed on the fine grid, namely a primal and dual coarse grid. The primal coarse grid consists of the fine cells edged by the bold black line and are centered by a single vertex cell which can be seen in figure 4.3. While the dual coarse grid is cornered by four vertex cells and the boundaries are in the middle of the edge cells connecting the vertex cells. The grid can be divided into three categories: interior cells, edge cells and vertex cells. The primal coarse cells (Ω_i^C with i from $1,\ldots,N_C$) can be considered as control volumes while the dual coarse cells (Ω_j^D with j from $1,\ldots,N_D$) are used for localized domain calculations.

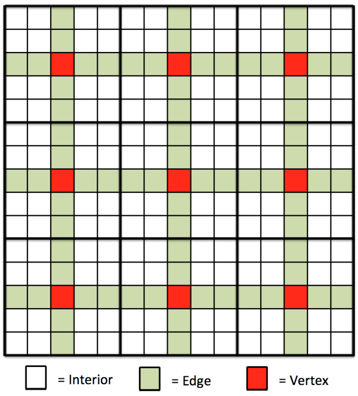

Figure 4.3: Primal and dual grid.

The basis functions are calculated by solving

$$\begin{cases} -\nabla\cdot(\lambda\cdot\nabla\phi_j^i)=0 & in\,\Omega_j^D \\ -\nabla_{||}\cdot(\lambda\cdot\nabla\phi_j^i)_{||}=0 & on\,\partial\Omega_j^D \\ \phi_j^i(x_k)=\delta_{ik} & \forall x_k\in 1,\ldots,N_C \end{cases} \tag{4.11}$$

where ϕ_j^i represents the basis function of coarse node i in dual coarse block Ω_j^D. In addition, subscript $||$ indicates the vector being tangential to the dual-coarse cell boundary, $\delta\Omega_j^D$.

4.2. Flow-Based upscaled ADM

In this research, the flow-based upscaling ADM and multiscale-based ADM are presented and investigated. As stated in the previous section, the main advantage of ADM is that it maintains the local heterogeneity of a coarse cell via locally-computed multiscale basis functions. While during the flow-based upscaling approach, an effective permeability is calculated at each level. Figure 4.4 illustrates the difference between the permeabiility fields that the both approach employ, at a time step. The permeability field of multiscale-based ADM shows that it maintains local heterogeneities while upscaling-based ADM shows how the effective permeability can look like for an upscaling-based approach.

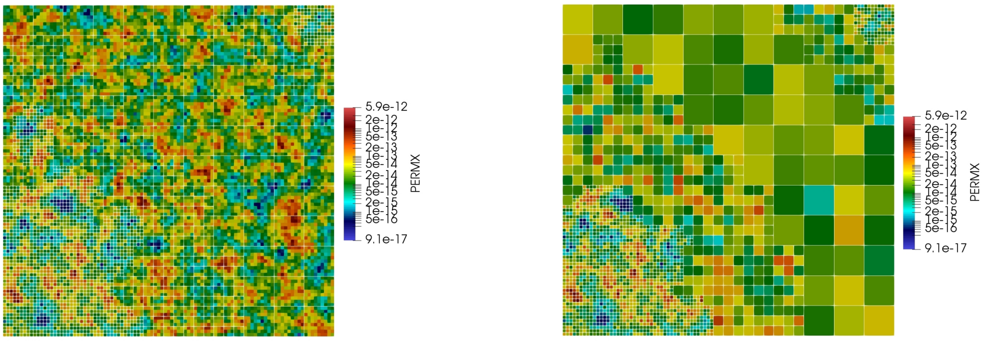

(a) ADM active permeability field at second time-step (b) Upscaled active permeability field at second time-step

Figure 4.4: Permeability field used in ADM and Upscaled-approach at the same time-step.

An important difference between ADM and the classical upscaling method is in the pressure interpolator (prolongation) operators they employ. Whole multiscale basis functions are used for multiscale-based ADM approach, constant interpolators are employed for upscaling-based ADM approach. The overall procedures of the two approaches are presented in figure 4.5.

4.2.1. Flow-based permeability upscaling

During the upscaling of permeability an effective permeability (K_{eff}) is calculated for each coarse cell at level $l+1$; based on the user-defined upscaling factor at level l. The upscaling procedure is illustrated in figure 4.6, where the effective permeability is calculated by solving local-flow problem in x and y directions, subject to no-flow Neumann boundary conditions at two sides and Dirichlet 1 and 0 at the others.

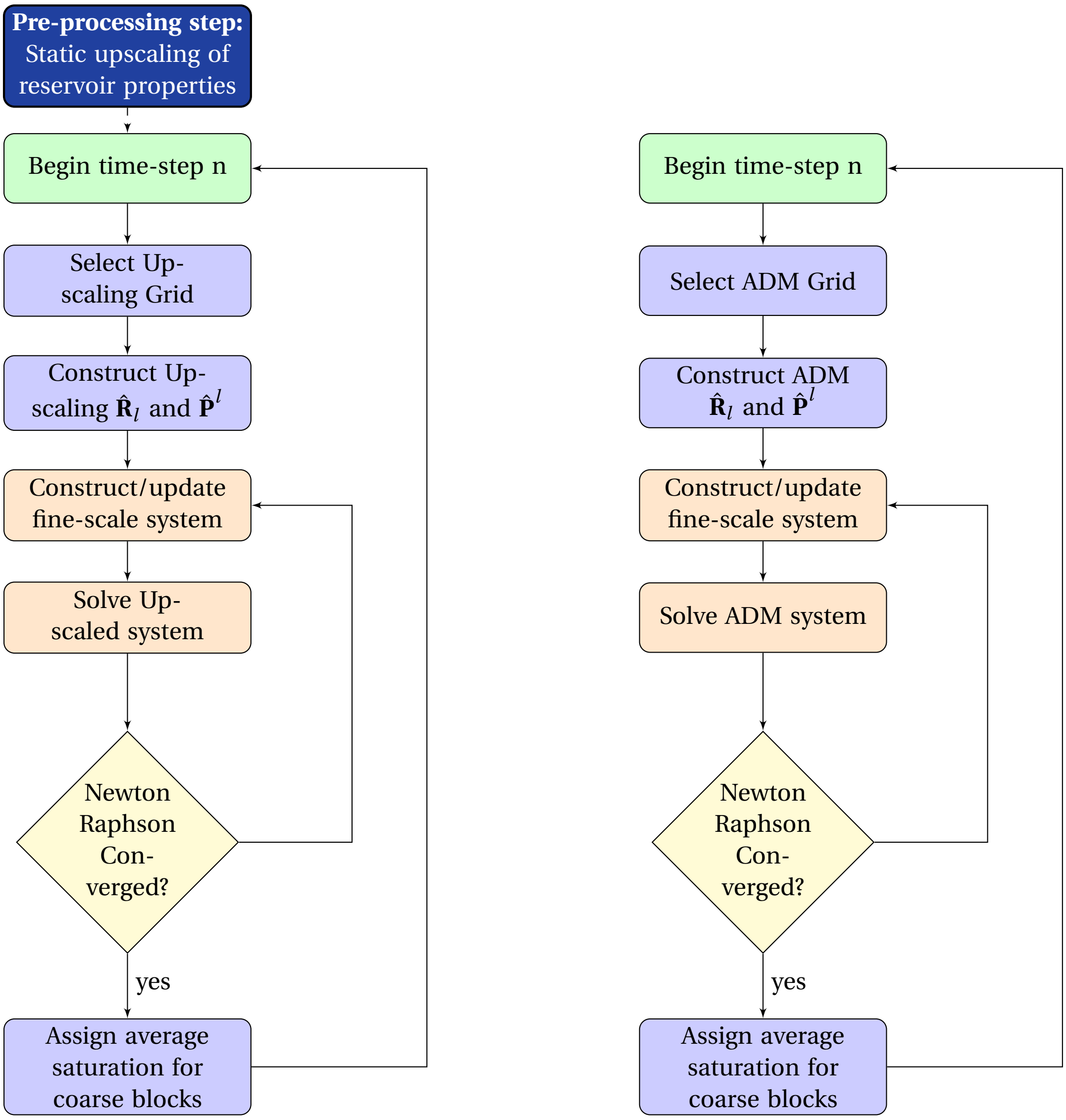

(a) Overview of upscaling-based ADM.

(b) Overview of multiscae-based ADM.

Figure 4.5: Overview of upscaling-based and multiscale-based ADM.

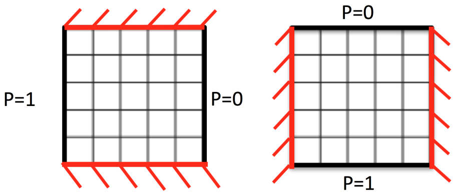

Figure 4.6: Local flow-based upscaling problem for finding effective permeability in x (left) and y (right) directions.

The effective permeability is then found using the cross-section velocity u_i as

$$u_i = \frac{K_{eff,\,i}}{\mu} \cdot \frac{(P_{c1} - P_{c2})}{\Delta x_C}. \tag{4.12}$$

Here, the subscript i indicates the flow direction (x or y), $K_{eff,i}$ is the effective upscaled permeability in i direction, and Δx_c is the coarse cell size. Figure 4.7 illustrates a possible multilevel upscaled permeability field.

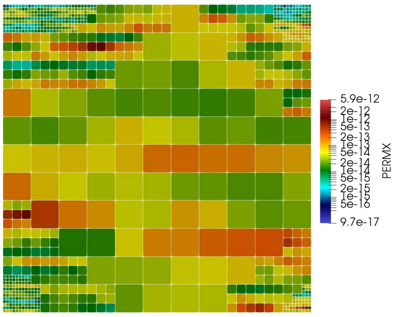

Figure 4.7: Upscaled K_x permeability field.

4.2.2. Upscaled-based ADM approach

After pre-calculating all the effective multilevel permeability fields, the multiphase flow simulation can be started. In each time step, the multilevel dynamic grid is imposed. This is done by refining the grid where ΔS is high (step 3 in figure 4.5a). Then the upscaled effective properties replace the fine-scale permeability quantities in the corresponding coarse cells. Clearly, at places where the fine-scale grid is imposed, no upscaling property is employed. This adjusted fine-scale system is now restricted to an ADM system with the use of restriction and prolongation operators, which contain constant 1 entries. More precisely, the restriction operator to coarsen the system form $l-1$ to level l reads

$$\mathbf{R}_l^{l-1} = \begin{pmatrix} (R_p)_l^{l-1} & 0 \\ 0 & (R_s)_l^{l-1} \end{pmatrix}_{N_l \times N_{l-1}}, \tag{4.13}$$

where, specially

$$(\hat{R}_p)_l^{l-1}(i,j) = \begin{cases} (R_p^{l-1})(i,j) & if\ cell\ i \subset \Omega^l\ and\ cell\ j \subset \Omega^{l-1} \\ \delta_{ij} & \text{otherwise} \end{cases} \tag{4.14}$$

holds. The prolongation operator which maps a coarse scale solution $l+1$ to a fine-scale solution (higher resolution level l) is given by

$$\mathbf{P}_{l-1}^l = \begin{pmatrix} (P_p)_{l-1}^l & 0 \\ 0 & (P_s)_{l-1}^l \end{pmatrix}_{N_{l-1} \times N_l}, \tag{4.15}$$

where

$$(P_S)_{l-1}^l = (R_l^{l-1})^T \tag{4.16}$$

and

$$(\hat{P}_p)_{l-1}^l = ((\hat{R}_p)_l^{l-1})^T. \tag{4.17}$$

5

Numerical Results for CO_2 Injection

In this chapter, the developed upscaling-based and multiscale-based ADM methods are investigated for several systematic test cases as shown in figure 5.1. To come to a conclusive outcome, for each permeability realisation set, 6 equiprobable (same geo-statistical properties) are used, from which average values are extracted. For all cases the fine scale simulation results are compared against upscaling and multiscale ADM approaches. For the sake of a brief chapter, for each sensitivity study, only the results of one permeability case is shown. All other results can be found in the Appendix.

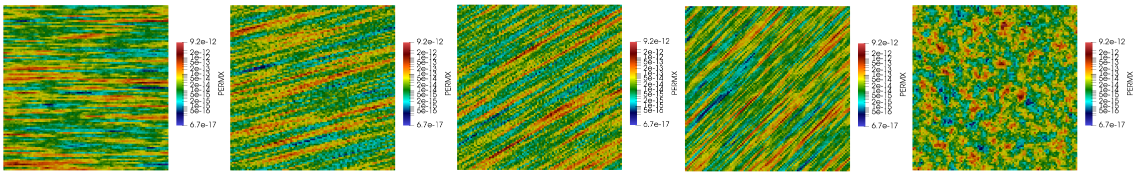

(a) 0° (layered) (b) 15° (layered) (c) 30° (layered) (d) 45° (layered) (e) patchy.

Figure 5.1: Overview of the systematic permeability fields from patchy (right) to layered with different orientation angles.

5.1. Numerical experiments: influence of capillary pressure

We consider a quarter-five-spot test case, where the injection is at the lower left corner and the production in the upper right corner. The dimensions of all test cases are 1 × 1 [m^2]. A fine grid size resolution of 99 × 99 is used. For the ADM and Upscaling method a coarsening ratio of 3 has been chosen for each level, with maximum 2 coarsened levels. A total simulation time of 12 days has been chosen, this is because after 12 days the domain is mostly flooded. The injected fluid is CO_2 and the pores are inhabited by brine, representative fluid properties for CO_2 and brine are chosen. Furthermore, the temperature is assumed to be constant $323.15K$. The porosity is 0.221. Parameter details can be found in the appendix A, in table A.1.

In this section the influence of capillary pressure on the performance of Upscaled-based ADM and ADM is investigated. As explained in chapter 2 the capillary number, which is the ratio of viscous and capillary forces, determines the influence of capillary pressure on the total flow. When the capillary number is low, capillary forces dominate the flow pattern. While at a high capillary number viscous forces are dominant. In this research the capillary number is adjusted by changing the interfacial tension. Besides adjusting the interfacial tension the simulations for all cases have been performed including and excluding capillary pressure. Three interfacial tensions have been investigated. The first interfacial tension is in the domain where viscous forces are dominant, the second interfacial tension is in the transition area and the third interfacial tension is chosen to represent the capillary dominated regime. The interfacial tensions are shown in table 5.1.

In this sensitivity a 45° diagonal layered heterogeneous quarter-five spot permeability field has been investigated. Injection is performed in the lower left corner and production in the upper right.

Table 5.1: Interfacial tensions and capillary numbers.

Interfacial tension ($Pa \cdot sec$)	**Value**	**Capillary Number**
Interfacial Tension 1:	6.5e-10	high (541)
Interfacial Tension 2:	6.5e-7	medium (0.541)
Interfacial Tension 3:	6.5e-6	low (0.0541)

Figure 5.2 shows the fine-scale saturation solution for different 3 interfacial tensions, including and excluding capillary pressure. The left column corresponds to no capillarity, while the right graphs are obtained by using capillary pressure. The increasing effect of capillarity pressure can be seen in figure 6.1d and 6.1f. Note the significant effect of capillary pressure on the saturation results.

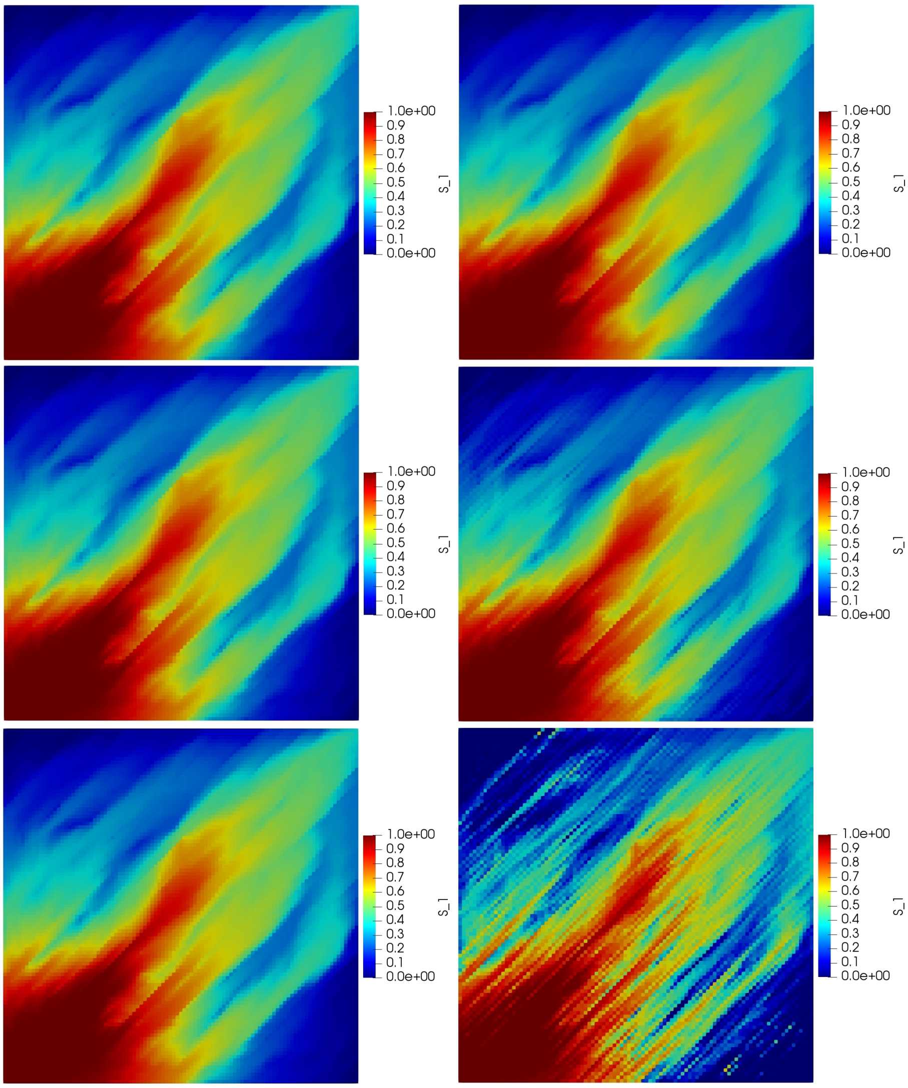

Figure 5.2: Saturation profiles with (right column) and without (left column) capillarity and different interfacial tensions (each row).

In figure 5.3 the left column shows the fine-scale, multiscale-based ADM and upscaling-based ADM saturation solutions for interfacial tension 3 using ΔS tolerance of 0.1. Figure 5.4 displays the corresponding pressure fields. These results are obtained without taking capillarity into account. Multiscale-based ADM employs 30% active fine-scale cells and the upscaling-based approach employs 24% of the fine-scale grids. The errors for different tolerances are also shown in the top-right sub-figures. As can be concluded from the graph and from the saturation-error plots, upscaling-based approach results in significant errors compared with multiscale-based approach. Thus, multiscale-based ADM outperforms the upscaling-based approach, even though the upscaling procedure is employed in an ADM (multilevel) framework, i.e., only behind the front the effective coefficients are used and at the front fine-scale grid is employed.

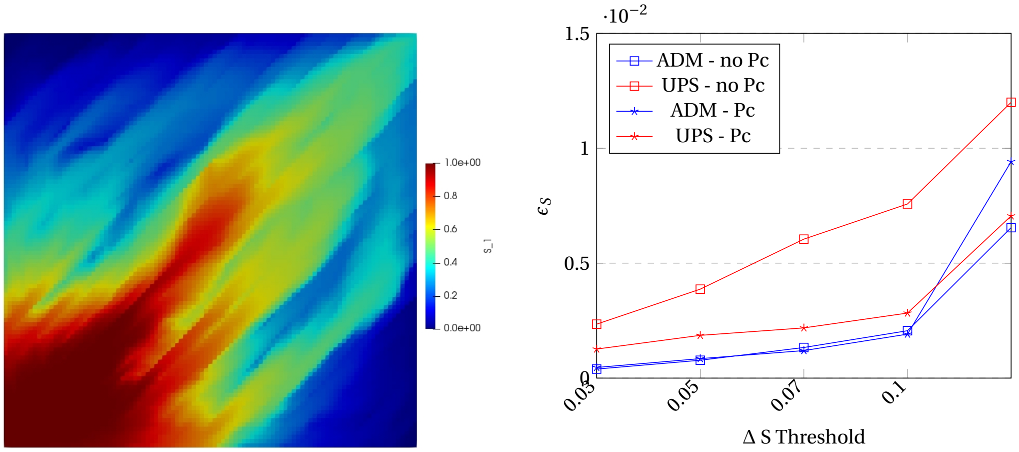

(a) Fine-scale saturation solution, no capillarity.

(b) Mean saturation error.

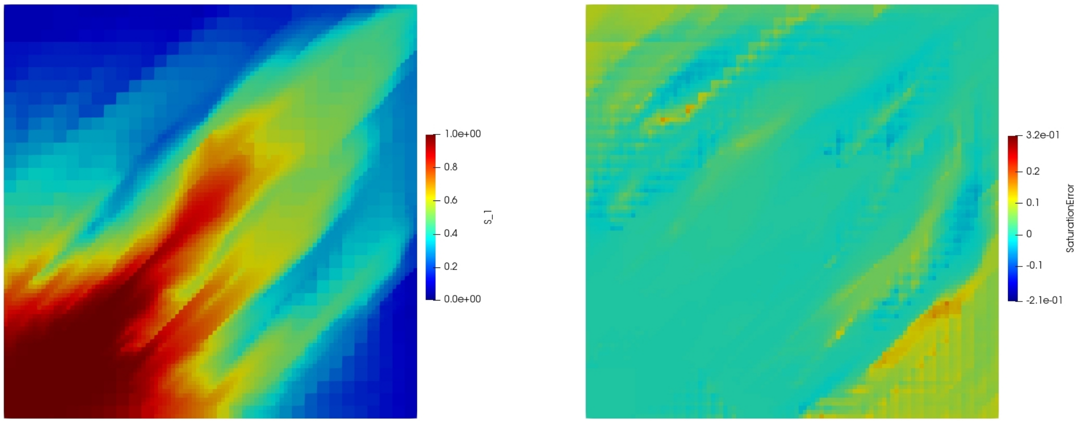

(c) Multiscale-based ADM saturation.

(d) Multiscale-based ADM saturation error.

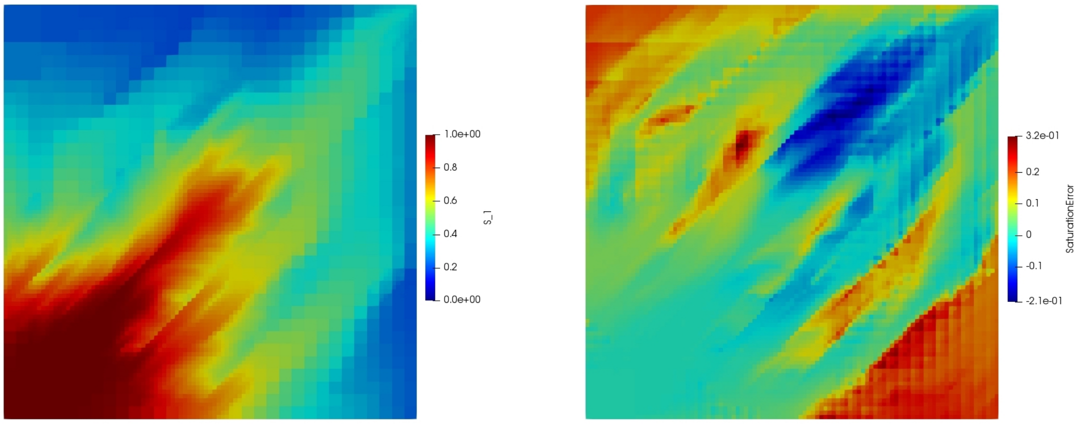

(e) Upscaling-based ADM saturation.

(f) Upscaling-based ADM saturation error.

Figure 5.3: Upscaling-based vs multiscale-based ADM solution for the case with no capillary pressure and refinement criterion of $\Delta S = 0.1$ and interfacial tension 3. Note that multiscale-based and upscaling-based approaches employed (in average), respectively, 30% and 24% of the fine grid cells. Sub-figure (b) shows the saturation error norm for different threshold values.

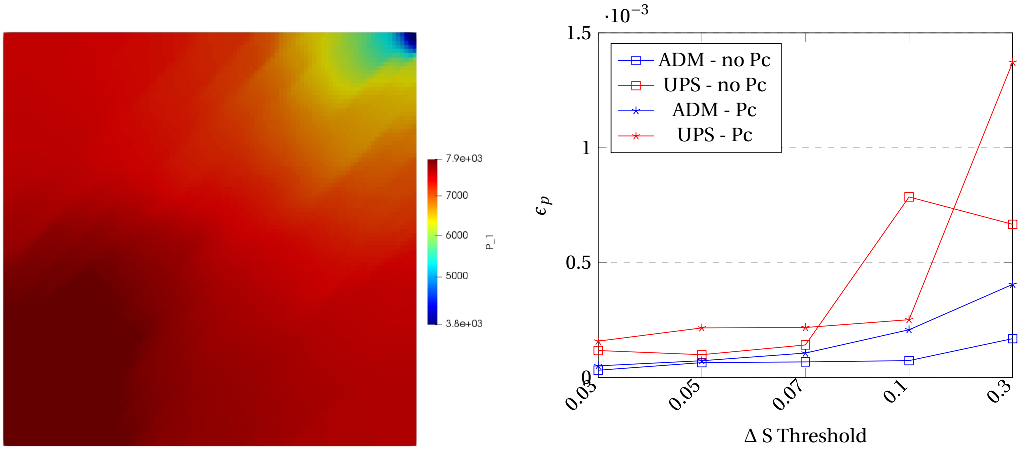

(a) Fine-scale pressure solution, no capillarity.

(b) Mean pressure error.

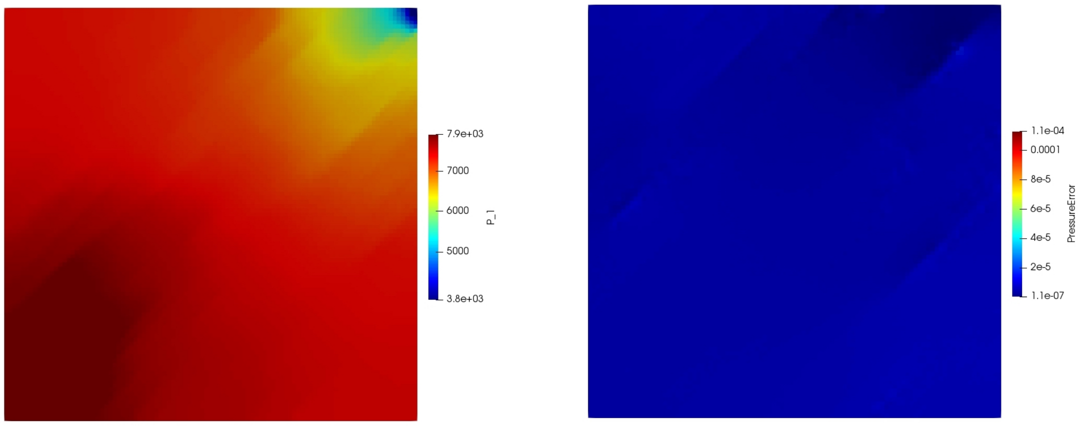

(c) Multiscale-based ADM pressure.

(d) Multiscale-based ADM pressure error.

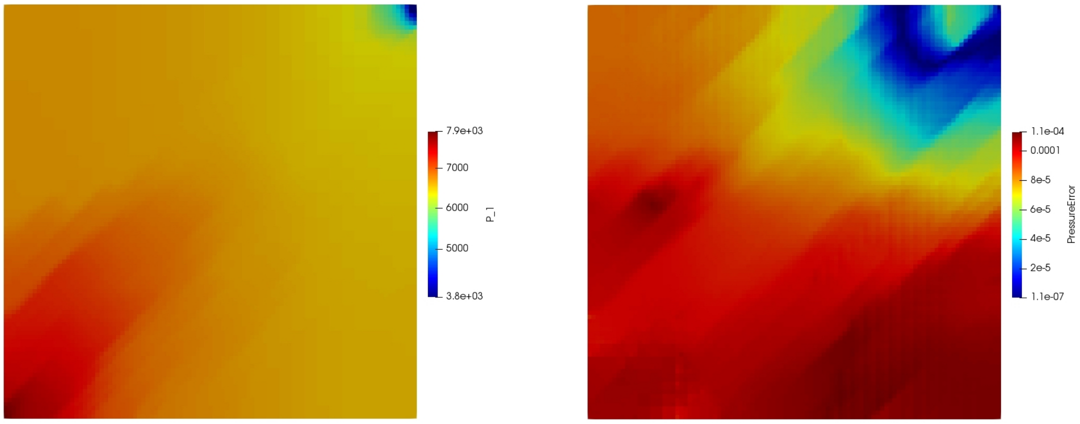

(e) Upscsaling-based ADM pressure.

(f) Upscsaling-based ADM pressure error.

Figure 5.4: Upscaling-based vs multiscale-based ADM solution for the case with no capillary pressure and refinement criterion of $\Delta S = 0.1$ and interfacial tension 3. Note that multiscale-based and upscaling-based approaches employed (in average), respectively, 30% and 24% of the fine grid cells. Sub-figure (b) shows the pressure error norm for different threshold values.

Figures 5.5 and 5.6 illustrate the results for fine-scale, multiscale-based and upscaling-based ADM when capillary pressure is considered. Obviously can be concluded that when capillary forces are dominant both methods provide similar results with a similar degree of error. There should however be noted that during these simulations a significant greater proportion of fine-scale cells is being deployed. The ADM-method uses 66% of active fine-scale cells while the Upscaled-based approach uses 85 %. From this can be concluded that when simulations are being performed including more complex physics such as capillarity a higher degree of active fine-scale cells will be deployed. In addition to the first comment with respect to active cells, ADM does use approximately 20% less active fine-scale cells while reaching an error which is of the same order of magnitude.

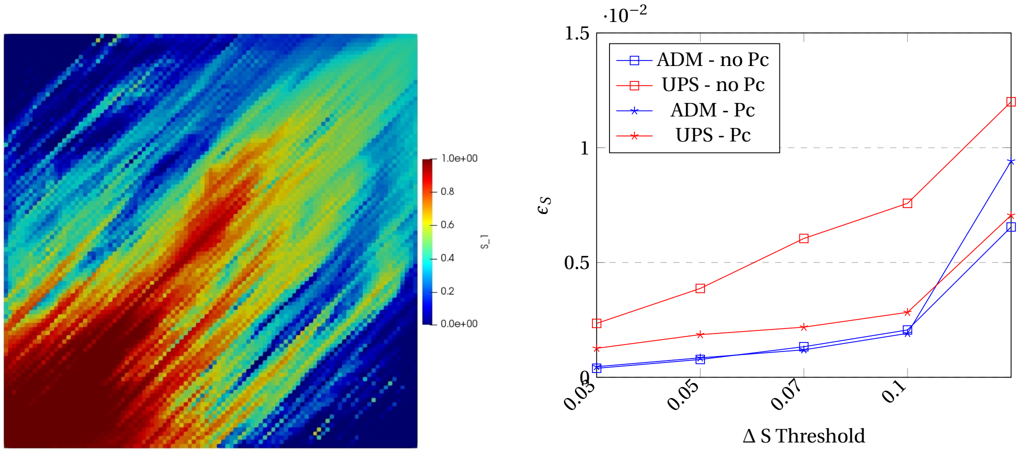

(a) Fine-scale saturation, low capillary number

(b) Mean saturation error.

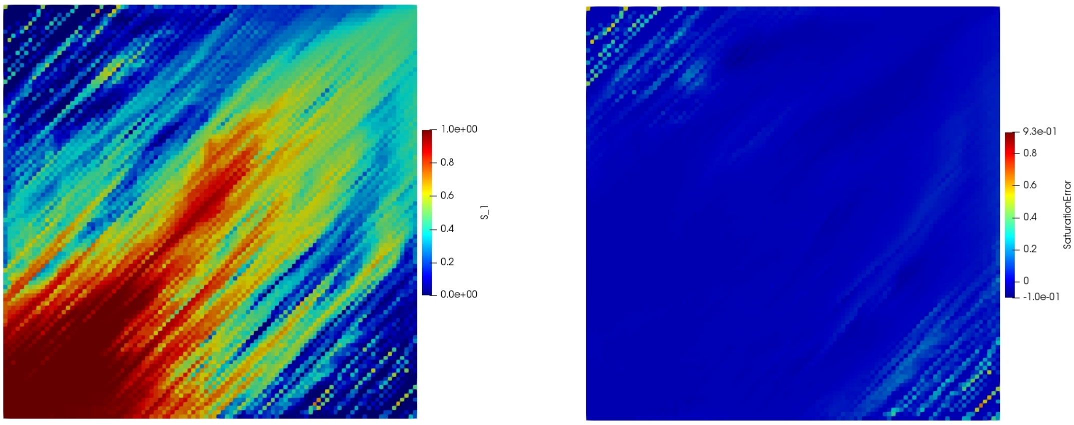

(c) Multiscale-based ADM saturation.

(d) Multiscale-based ADM saturation error.

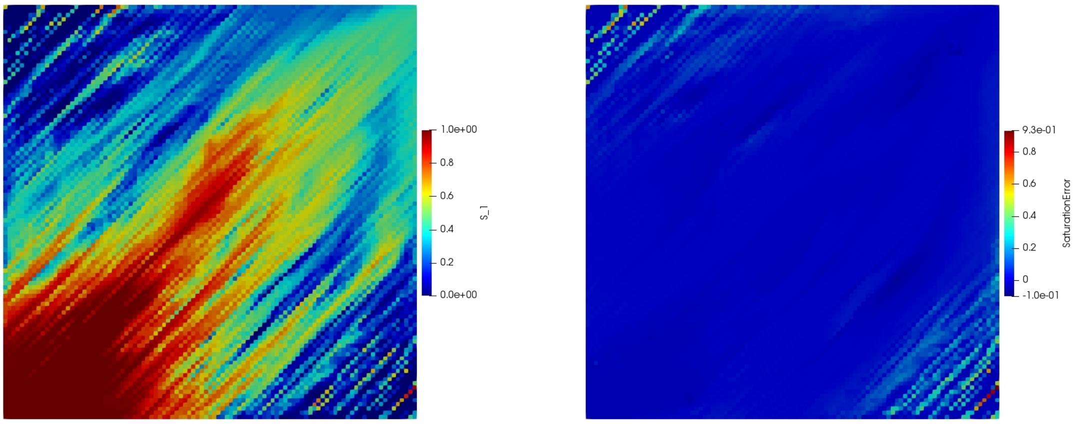

(e) Upscsaling-based ADM saturation.

(f) Upscsaling-based ADM saturation error.

Figure 5.5: Upscaling-based vs multiscale-based ADM solution for the case with (low) capillary pressure and refinement criterion of $\Delta S = 0.1$. Note that multiscale-based and upscaling-based approaches employed (in average), respectively, 66% and 85% of the fine grid cells. Sub-figure (b) shows the error norm for different threshold values.

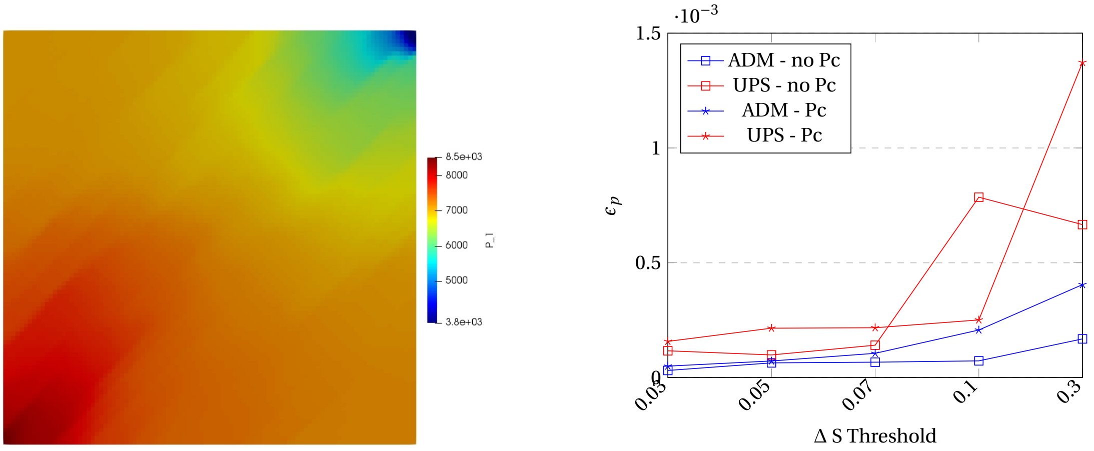

(a) Fine-scale saturation solution, low capillary number

(b) Mean pressure error.

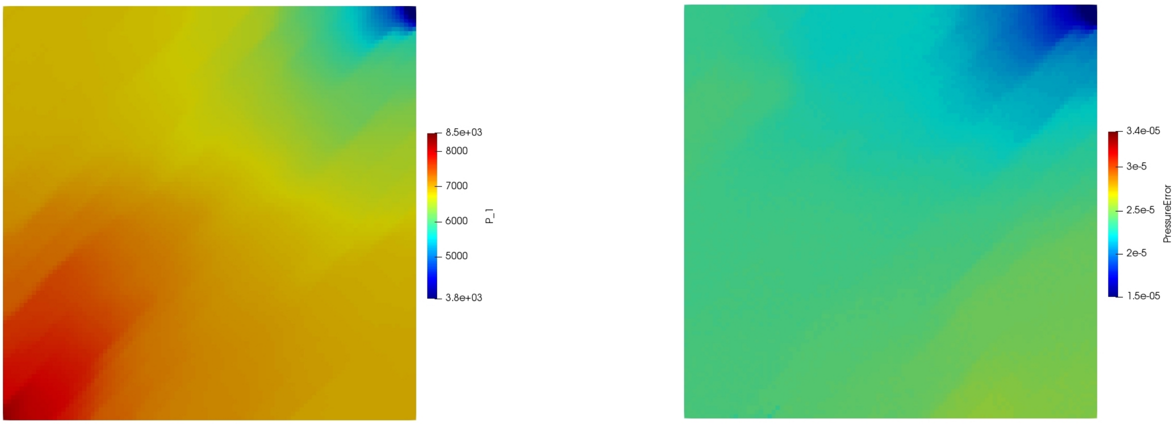

(c) Multiscale-based ADM pressure.

(d) Multiscale-based ADM pressure error.

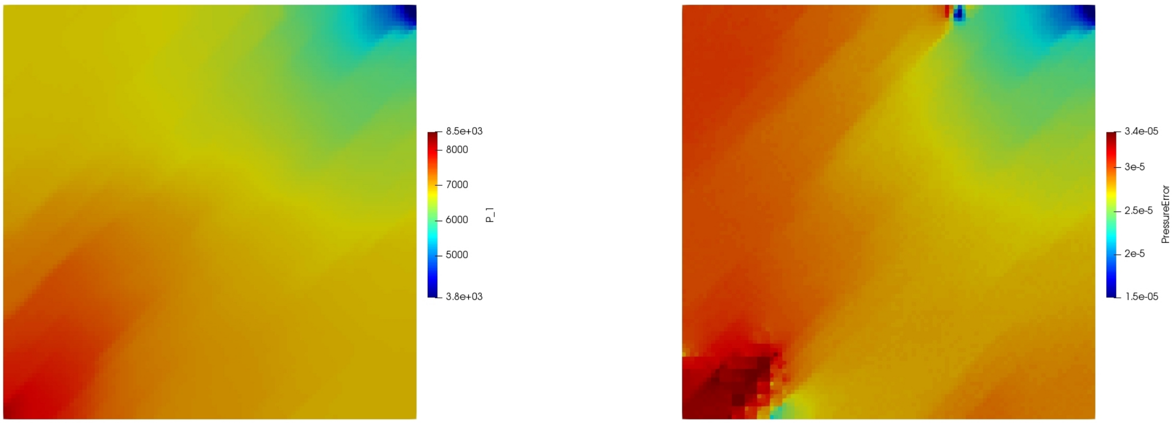

(e) Upscaling-based ADM pressure.

(f) Upscaling-based ADM pressure.

Figure 5.6: Upscaling-based vs multiscale-based ADM solution for the case with (low) capillary pressure and refinement criterion of $\Delta S = 0.1$. Note that multiscale-based and upscaling-based approaches employed (in average), respectively, 66% and 85% of the fine grid cells. Sub-figure (b) shows the error norm for different threshold values.

Figure 5.7 displays the production of brine over the simulation time of 12 days with $\Delta S = 0.03$ and $\Delta S = 0.1$ refinement threshold. The multiscale-based ADM solutions (blue) are in better agreement with the fine-scale ones (red) than the upscaling-based ones (green). Note that using the interfacial tension 1 and 2 the production prediction error in upscaling-based ADM is 5% higher than the error in multiscale-based ADM.

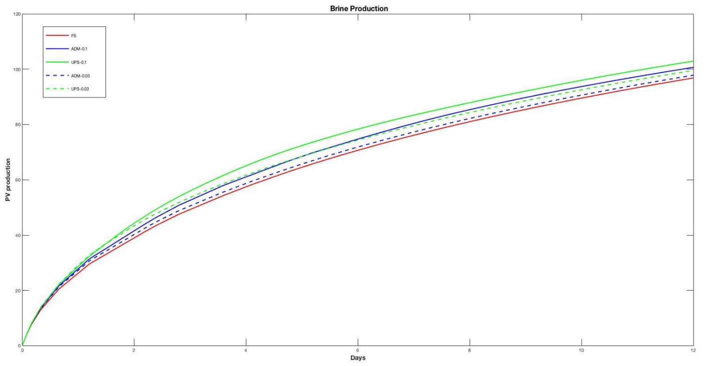

Figure 5.7: Brine production over simulation time for 45° permeability field with $\Delta S = 0.03$ and $\Delta S = 0.1$ refinement threshold. Red curve is the fine-scale, blue the multiscale-based and green the upscaling-based solutions.

Through these results we conclude that the multiscale-based ADM outperforms the upscaling-based approach, even though both are employed on adaptive dynamic grid which imposes fine-scale grids at the fronts. For the case with capillary, the multiscale-based ADM provides the same accuracy (compared with upscaling-based approach) with a lot less active grid cells. Note that for the case with capillary pressure, a lot more active grid cells were needed to obtain accurate results. Furthermore, one should note that the studied test cases were quite small compared to the field-scale relevant cases. As shown in the literature, the ADM performs a lot less active grid cells for larger domains, due to the local nature of the saturation fronts.

Next, sensitivity of the both ADM approaches with respect to mobility ratio and degree of wetting is studied. The sensitivity for porosity was done, which is left out for the sake of a brief thesis.

5.2. Numerical experiments: different mobility ratios

After investigation of the influence of a changing interfacial tension and presence of capillary pressure, in this section the simulators are benchmarked with respect to sensitivity to the mobility ratio, i.e.,

$$M = \frac{\mu_{resident fluid}}{\mu_{injected fluid}}. \tag{5.1}$$

The injection rate during these simulations is 1.5 pore volumes and capillary pressure is taken into account. Furthermore, ΔS tolerance of 0.07 is used for grid refinement. These sensitivities have been performed on all 5 permeability cases shown in figure 5.1. Besides a varying viscosity of the injected CO_2 the same simulation parameters are used as in the case of the previous section. Detailed parameters of this sensitivity analyses are shown in table B.1. To determine the sensitivity with respect to variations in the viscosity of the injected fluid and thus the mobility ratio, 5 different ratios of 0.5, 1, 5, 10 and 24 are considered.

Figure 5.8 shows the effect of different mobility ratio on the saturation results. All pictures are taken at the same time step. The lower mobility ratio leads to more stable displacements, thus better sweep efficiency. Higher mobility ratios would lead to less effective recovery factors.

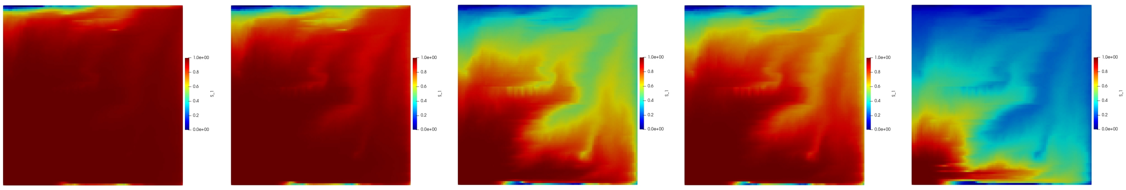

(a) M=0.5 (b) M=1 (c) M=5 (d) M=10 (e) M=24

Figure 5.8: Effect of mobility ratio (M) on saturation solution.

The influence of mobility ratio on the performance of upscaling-based and multiscale-based ADM methods can be seen in figure 5.9b and 5.10. For higher mobility ratios, the error in saturation increase. This is due to the fact that the front is much more defused in higher mobility ratios, compared with the lower (stable) ones. Comparing the two ADM approaches, it can be seen that the multiscale-based approach does indeed provide more robust framework. Specially the pressure errors indicate this conclusion.

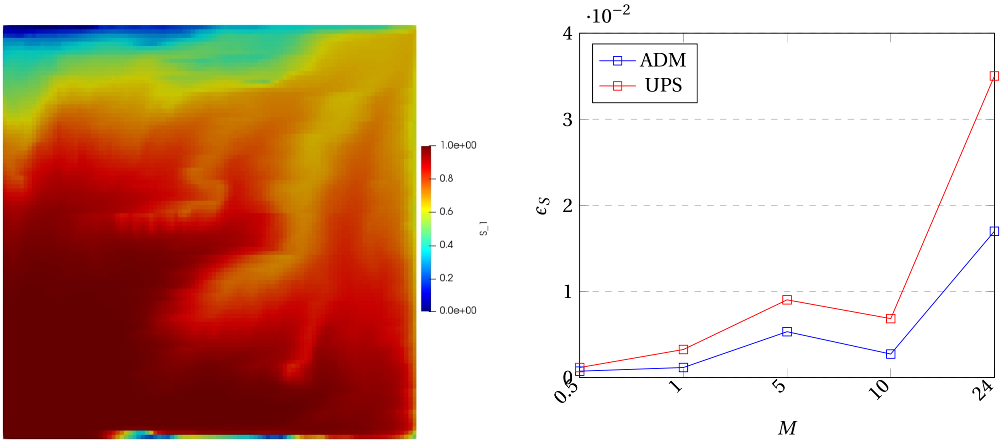

(a) Fine-scale saturation, M=10

(b) Mean saturation error.

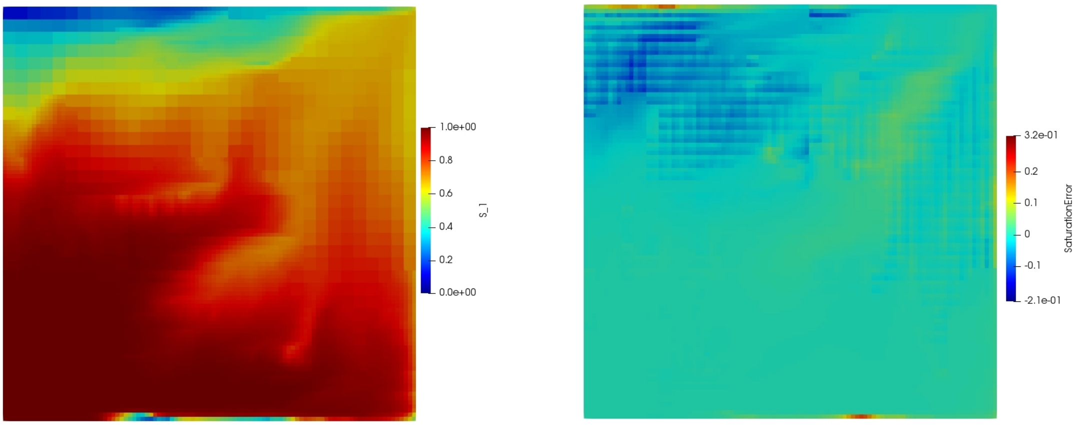

(c) Multiscale-based ADM saturation.

(d) Multiscale-based ADM saturation error.

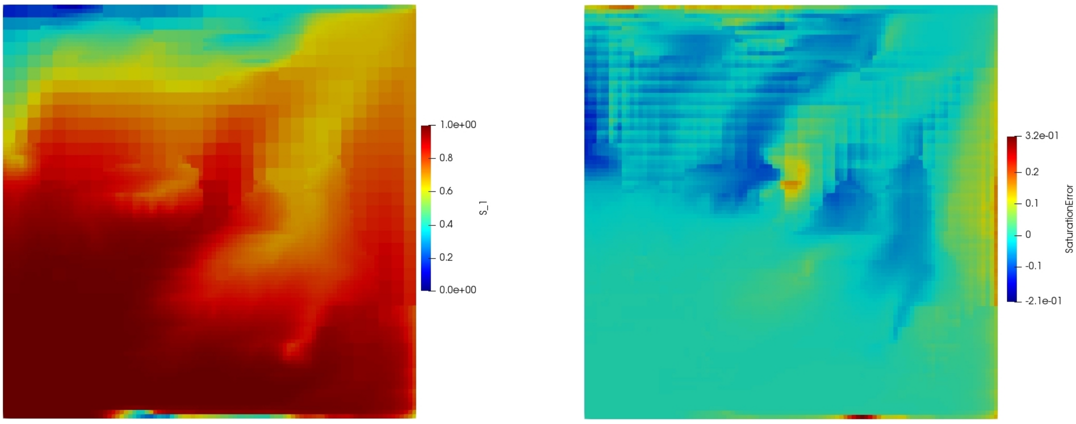

(e) Upscaling-based ADM saturation.

(f) Upscaling-based ADM saturation error.

Figure 5.9: Fine-scale, upscaling-based and multiscale-based ADM solutions (and errors) with $\Delta S = 0.07$ grid refining threshold, and $M = 10$. Upscaling-based approach imposes 17% and multiscale-based one 15% active grid cells. Also, the sub-figure (b) shows the error for different mobility ratios.

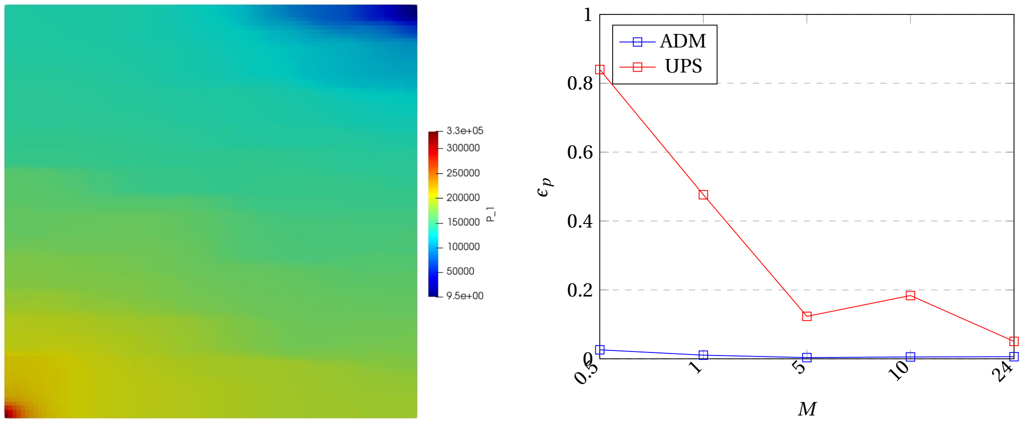

(a) Fine-scale pressure, M=10 (b) Viscosity sensitivity: Mean error pressure

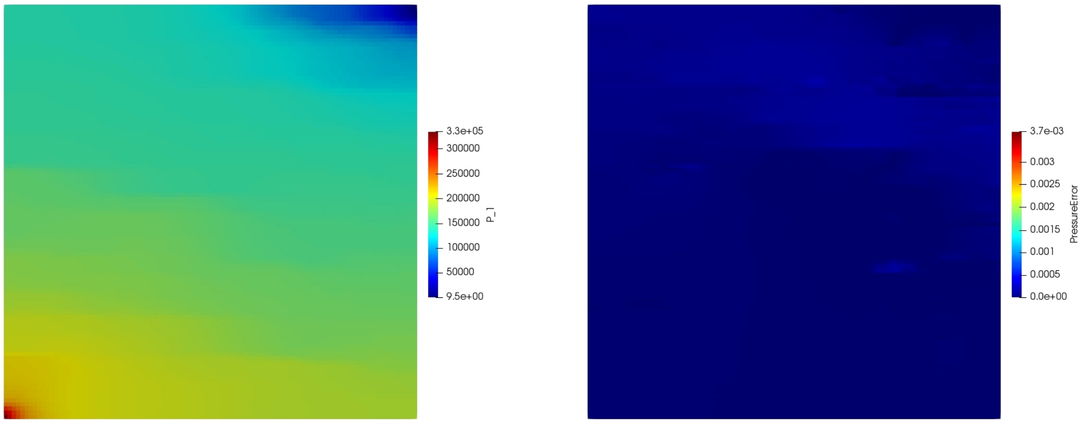

(c) Multiscale-based ADM pressure. (d) Multiscale-based ADM pressure error.

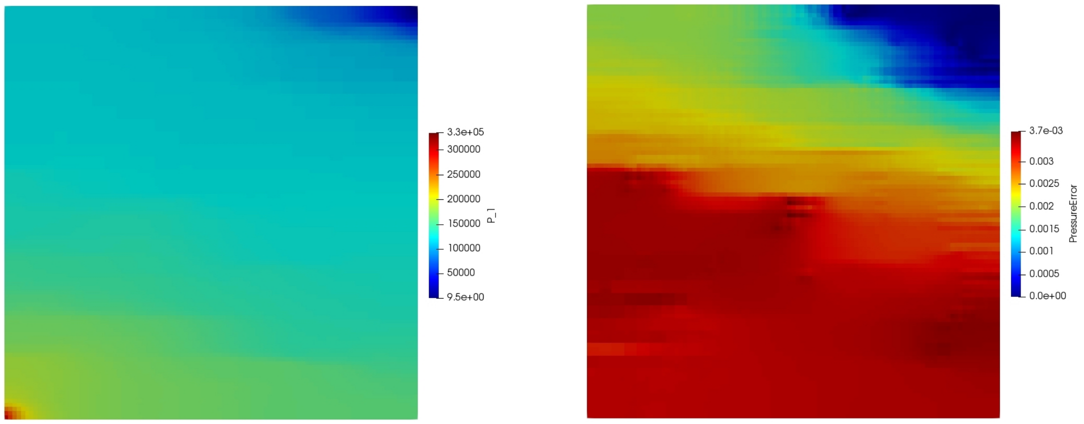

(e) Upscaling-based ADM pressure. (f) Upscaling-based ADM pressure error.

Figure 5.10: Fine-scale, upscaling-based and multiscale-based ADM solutions (and errors) with $\Delta S = 0.07$ grid refining threshold, and $M = 10$. Upscaling-based approach imposes 17% and multiscale-based one 15% active grid cells. Also, the sub-figure (b) shows the error for different mobility ratios.

The results of the other permeability fields are shown in Appendix B. Irrespective of the viscosity ratio, as shown in figure 5.11, the multiscale-based ADM uses slightly smaller active cells, at the same time, provides more accurate results. This is further confirmed by figure 5.12, which shows the production errors.

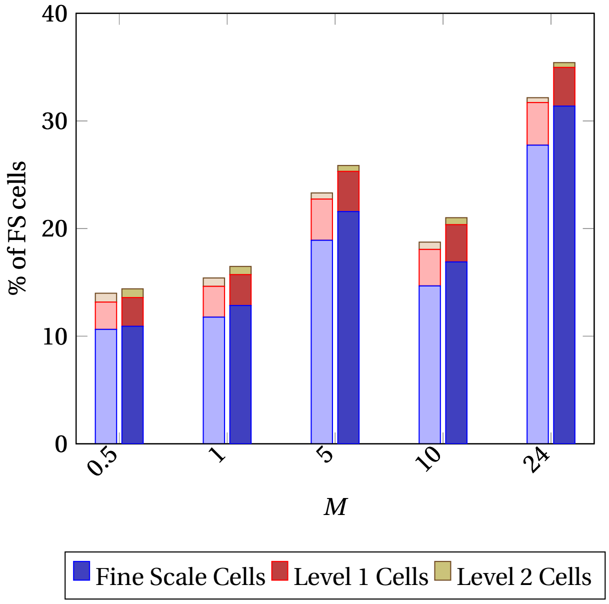

Figure 5.11: active grid cells for 0° permeability field test cases: multiscale-based (left bar) vs upscaling-based (right bar) ADM.

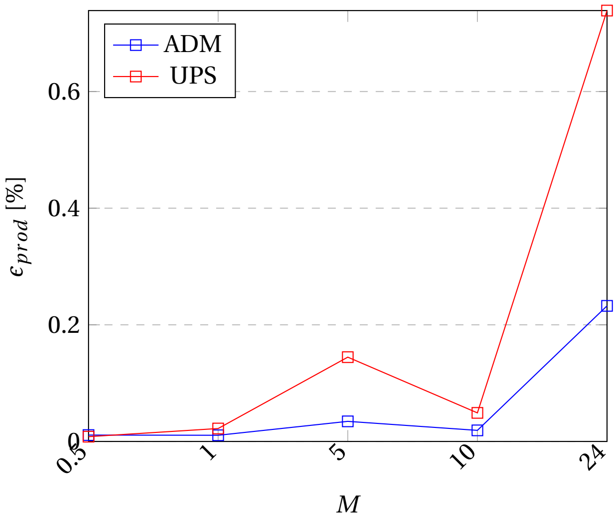

Figure 5.12: 0° Permeability Field: Percentual Mean Error Production

5.3. Numerical experiments: wetting phase injection

Previously, CO_2 was injected into brine. In this experiment the resident fluid of the reservoir are various well known crude oils with varying viscosities and densities ranging from light crudes to extra heavy oils. The different type of oils and specific characteristics are given in table 5.2. The purpose of this experiment is to investigate the behaviour of both ADM methods when the wetting phase is injected into the different resident fluids. Simulations are performed at an injection rate of 1.5 pore volumes daily, capillary pressure is taken into account and a ΔS tolerance of 0.07 is used.

In figures 5.14 and 5.15 an overview of the saturation and pressure results and error for the Arabian Medium are given. Similar to the previously found results, the upscaling-based approach leads to higher

Table 5.2: Characteristic values crudes used for sensitivity analysis.

Oil type	**Area**	**Type**	**Viscosity** ($Pa \cdot s$)	**Density** (kg/m^3)
Brent Blend:	North Sea	Ligth crude	1.6e-4	992
Arabian Medium:	Saudi Arabia	Medium crude	2.3e-4	965.9
BCF-17:	Venezuela	Heavy crude	1.709	854
Boscan:	Venezuela	Extra heavy crude	11.233	834.8

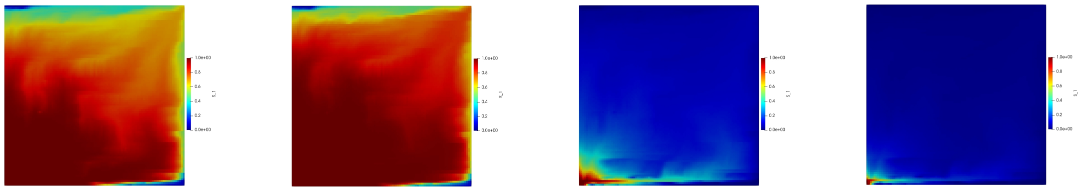

(a) Brent Blend (b) Arabian Medium (c) BCF-17 (d) Boscan

Figure 5.13: Saturation plots for different residing oil.

errors compared with the multiscale-based approach. This is the case for both saturation and pressure errors. The sub-figure (b) in the figures show the error trends for all 4 different cases. Note that the number of active cells deployed during simulation for multiscale-based and upscaling-based ADM methods are almost equal for all scenarios.

5.4. Conclusion:

In this chapter, performances of the developed multiscale-based and upscaling-based ADM methods were investigated for a variety of test cases. The performance of the simulator has been investigated using several measurable properties, namely: number of active cells during simulation, pressure and saturation error and the production errors. The sensitivity of the outcome with respect to mobility ratio, residing oil properties, and capillary pressure with different degrees of interfacial effects was also studied.

The influence of capillary pressure in the saturation profile was found significant. Both ADM approaches imposed a lot more active grid cells for strong capillary pressure case, expected from the nature of the process. Note that for larger (field-scale) test cases, the fraction of the front is expected to be much less than the overall size of the formation. As such, the ADM is expected to impose much fewer active grid cells for larger domains.

Another important point was that the increase of mobility ratio will smear out the sharp front, and as such more sub-domain regions are detected to be included in the zones of fine-scale grid cells. One may set looser tolerances for high mobility ratios, so that the active grid cells are lowered, as the smeared out front may not be necessarily needed to be captured very accurately.

It is very important to also note that the effective permeabilities (for upscaling-based approach) and multiscale basis functions (for multiscale-based approach) were all calculated at the beginning of the simulation; and never get updated during the simulation. This leads to significant speed up in both ADM simulations.

Overall, it can be concluded that multiscale-based ADM approach outperforms the upscaling-based one, both in terms of the quality of the results and the count of overall imposed active grid cells.

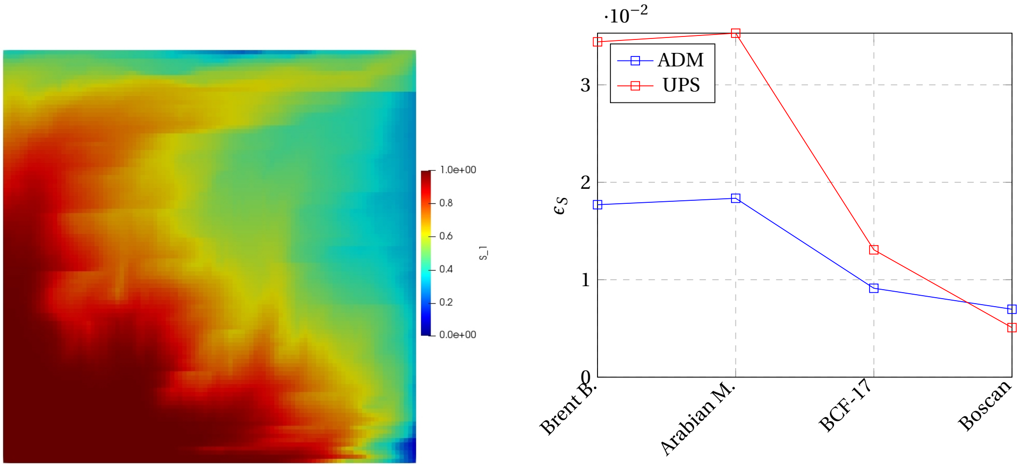

(a) Fine-scale saturation Arabian Medium

(b) Mean saturation error.

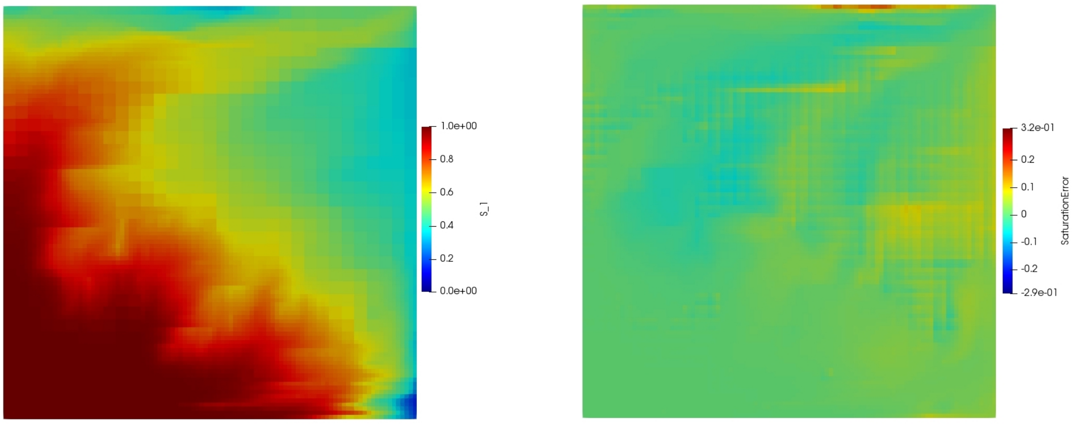

(c) Multiscale-based ADM saturation.

(d) Multiscale-based ADM saturation error.

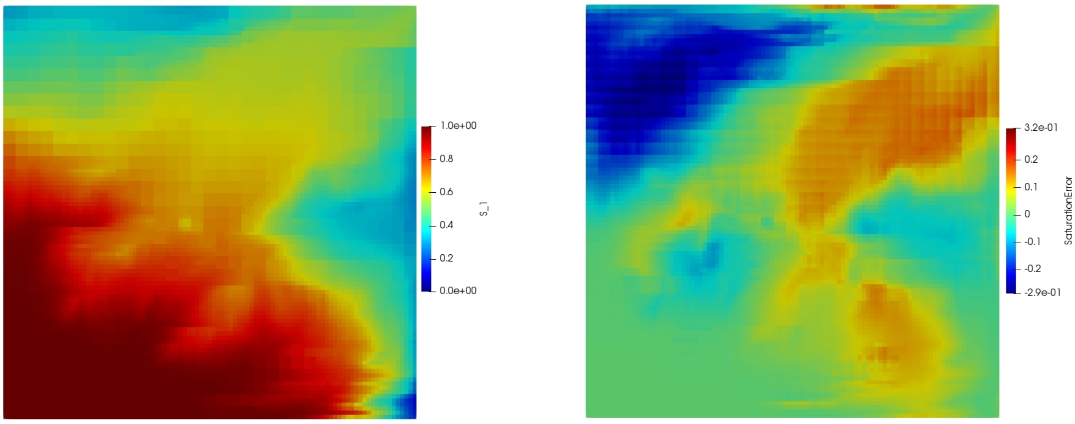

(e) Upscaling-based ADM saturation.

(f) Upscaling-based ADM saturation error.

Figure 5.14: Saturation profiles for the fine-scale, multiscale-based and upscaling-based ADM methods with $\Delta S = 0.07$ for the Arabian Medium. The sub-figure (b) shows the error for all the 4 cases.

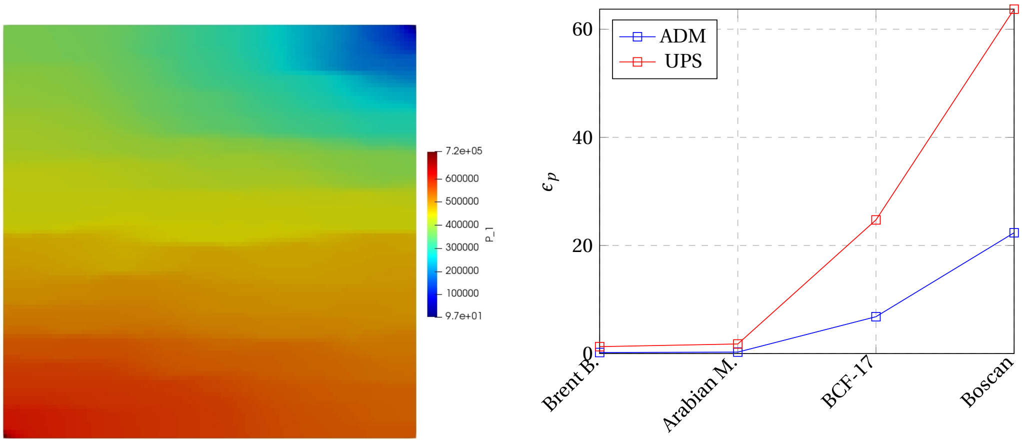

(a) Fine-scale pressure, $\phi = 0.3$

(b) Mean pressure error.

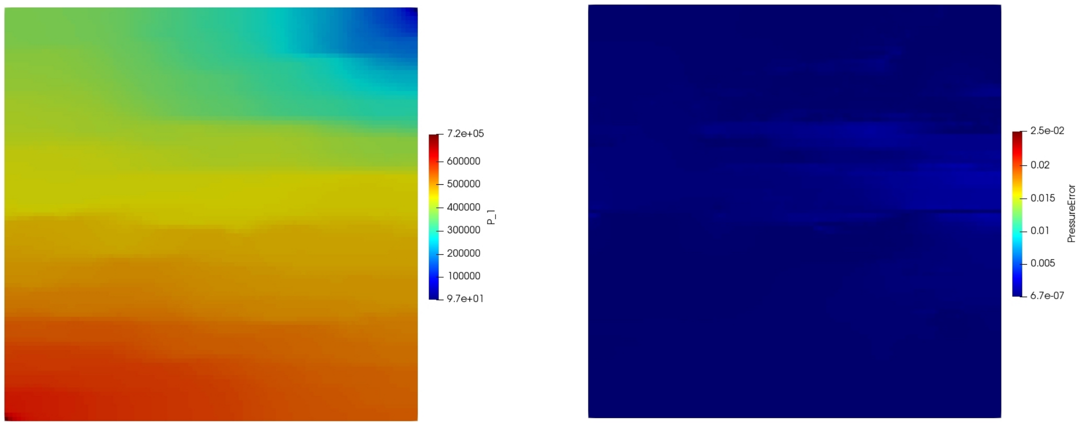

(c) Multiscale-based ADM pressure.

(d) Multiscale-based ADM pressure error.

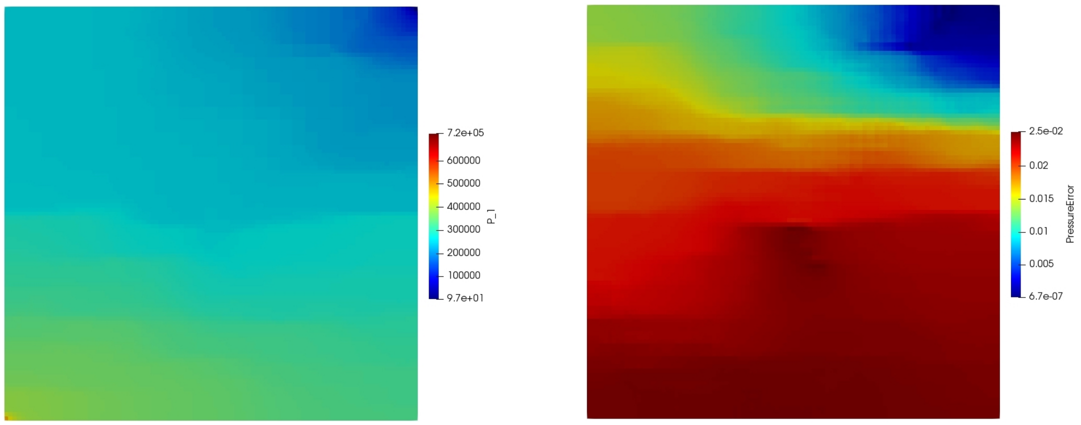

(e) Upscaling-based ADM pressure.

(f) Upscaling-based ADM pressure error.

Figure 5.15: Pressure profiles for the fine-scale, multiscale-based and upscaling-based ADM methods with $\Delta S = 0.07$ for the Arabian Medium. The sub-figure (b) shows the error for all the 4 cases.

6

Results of Miscible Mixing

In this chapter the results of the studied cases related to miscible flow displacement will be presented. The mixing processes will be investigated for homogeneous media with saturation perturbations along the injection side and secondly for heterogeneous media with similar characteristics used in the literature.

6.1. Mixing rocesses in homogeneous media

In this section, the viscous fingers are initiated by perturbing permeability of the first (West) column of the domain (injection boundary). The Péclet numbers used for the simulations are depicted in table 6.1. In table E.1 (appendix) the parameters for the study of viscous fingers initiated by saturation perturbations are shown. In this section two fine-scale resolutions are considered: 99×99 and 198×198. Figure 6.1 shows the fine-scale solutions for the two resolutions and the different Péclet numbers (different dispersions). From top to bottom the influence of dispersion increases, thus the Péclet number decreases.

Figures 6.2 and 6.3 show, respectively, the saturation distribution for fine-scale, multiscale-based and upscaling-based ADM methods for different fine-scale grid resolutions of 99 × 99 and 198 × 198. Note that these results correspond to “no-dispersion” case (i.e., infinity Péclet number). Similar as before, sub-figures (b) illustrate the error norms for different refinement thresholds. In the appendix, in figure E.2, the exact data for all three Péclet numbers can be found. From this can be concluded that multiscale-based ADM outperforms the upscaling-based approach for both pressure and saturation. Note that for the sake of a brief manuscript, only these selected results are presented. Overall, our findings for this case is representative of the other studied cases.

When the Péclet number increases, due to more fingers, the number of active cells increases. Production results illustrate that, in general, the error in multiscale-based ADM is below 0.5% (depending on the tolerances and resolutions), while for the upscaling-based approach the error is between 1% to 3%.

From these results can be concluded that ADM has significant advantage when complex mixing occurs.

6.2. Mixing processes in heterogeneous media

In the second case a range of Péclet numbers is used in a heterogeneous permeability field which is similar to literature and thus a comparison can be made. The values used are: 1000, 10000 and infinity. This case has been benchmarked on three tolerances, namely: 0.03, 007 and 0.1. The characteristics used to create a set of different cases with similar characteristics are comparable to values used in case 3 in [11]. The cases uses a

Table 6.1: Péclet numbers used for simulation of homogeneous media.

Péclet number (*Pe*)	**Value**
Case 1:	1000
Case 2:	10000
Case 3:	∞

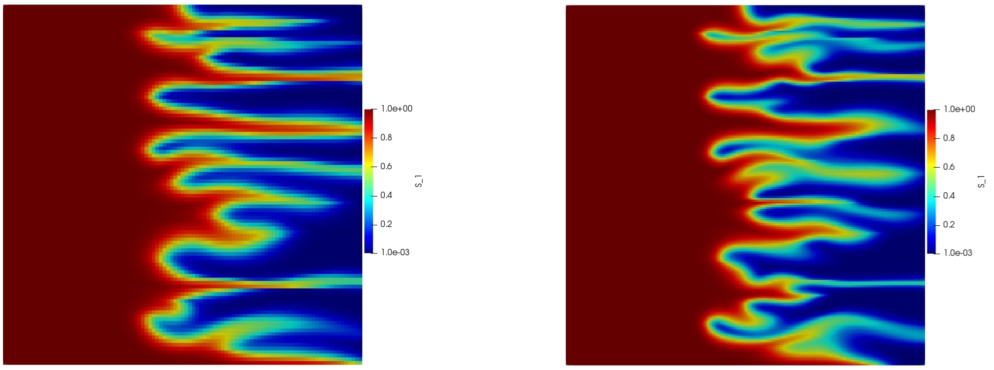

(a) No dispersion 99 × 99 grids.

(b) No dispersion 198 × 198 grids.

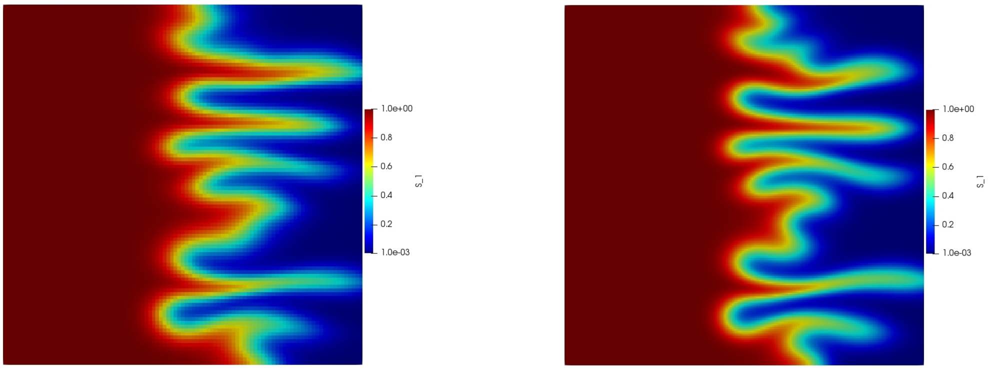

(c) Midum dispersion 99 × 99 grids.

(d) Midium dispersion 198 × 198 grids.

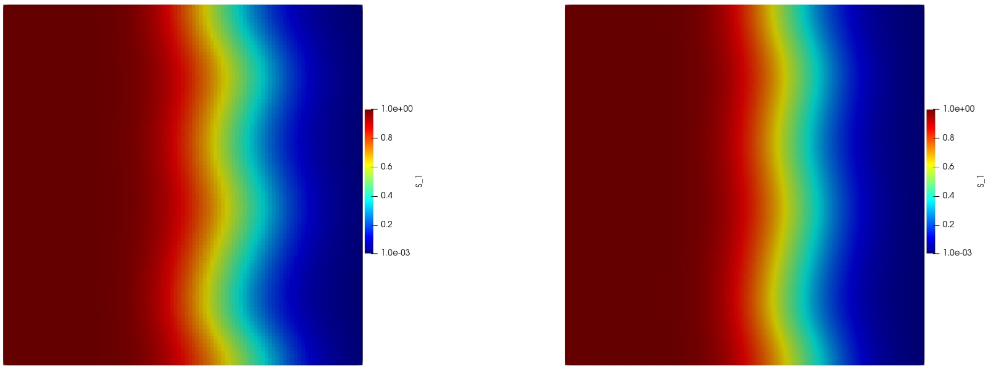

(e) High dispersion 99 × 99 grids.

(f) High dispersion 198 × 198 grids.

Figure 6.1: Fine-scale saturation profiles including mixing processes at different resolutions and Péclet numbers.

correlation length of $\lambda = 0.1$ and a Dykstra-Parson Coefficient (V_{dp}) of 0.63. In total 5 different realisations have been developed and simulated.

The heterogeneous reservoir forms a challenging case for the simulator. The simulations are performed using three Péclet numbers, resulting in different degrees of diffusion. The saturation distributions and error plots can be seen in the following figures, i.e., from 6.4 to 6.7. In all figures, the permeability fields are plotted in the sub-figures (b). Also, the saturation plots are provided for all test cases with different Péclet numbers, while for the last case, the pressure profiles are also provided. Note that the pressure profiles for other Péclet numbers have the same pattern.

For the upscaling-based approach, errors are quite visible (both for pressure and saturation), while the multiscale-based ADM method results in very accurate solutions. In addition, the production data studies revealed that the multiscale-based ADM leads to only 0.5% errors for a wide range of the refinement thresholds, while the upscaling-based approach can show error of above 4% with $\Delta S = 0.1$.The number of active grid cells used to solve this heterogeneous case for the varying Péclet numbers is similar for both approaches and is between 52 and 66 %.

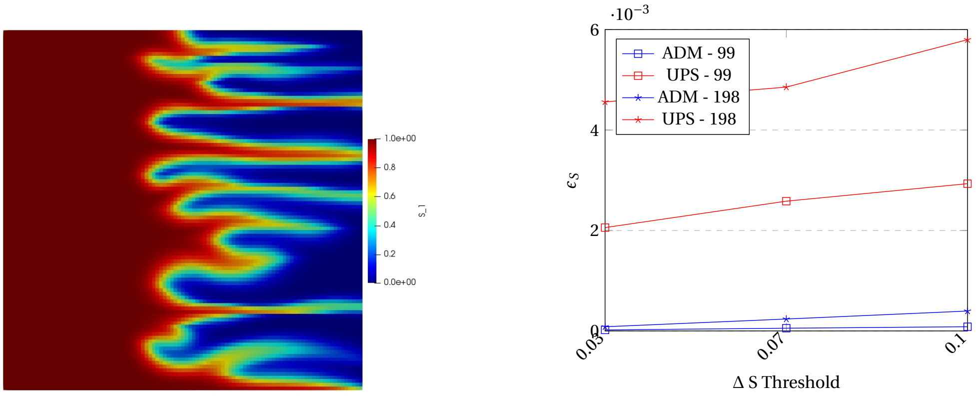

(a) Fine-scale saturation, no dispersion, 99x99 cells.

(b) Mean saturation error.

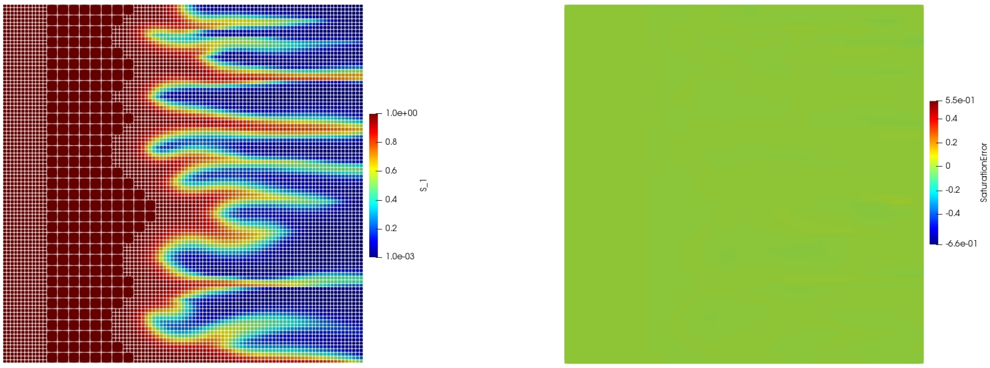

(c) Multiscale-based ADM saturation.

(d) Multiscale-based ADM saturation error.

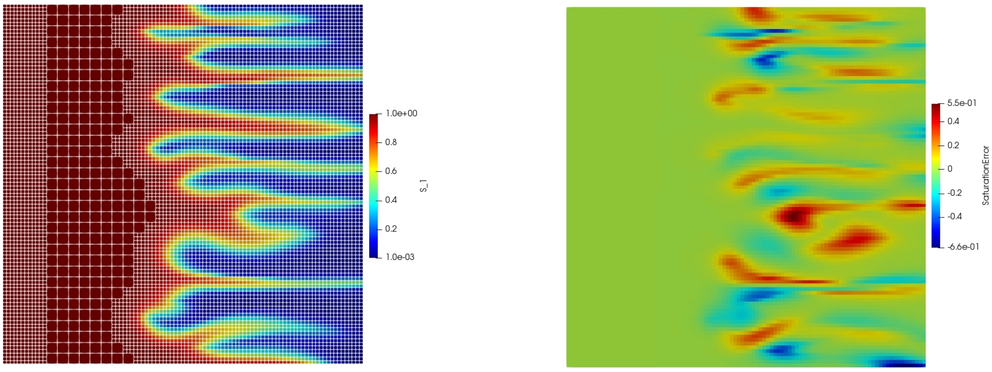

(e) Upscaling-based ADM saturation

(f) Upscaling-based ADM saturation.

Figure 6.2: Saturation for fine-scale (a) and ADM approaches. Also shown in sub-figure (b) is the error for different threshold values. Both ADM methods apply 62% of fine-scale cells.

Overall, it is clear that the multiscale-based ADM outperforms the upscaling-based approach for displacements with mixing. This study is of significant importance as for its industrial-relevant application, where classically an upscaling-based approach is implemented for the dynamic grid refinement methods.

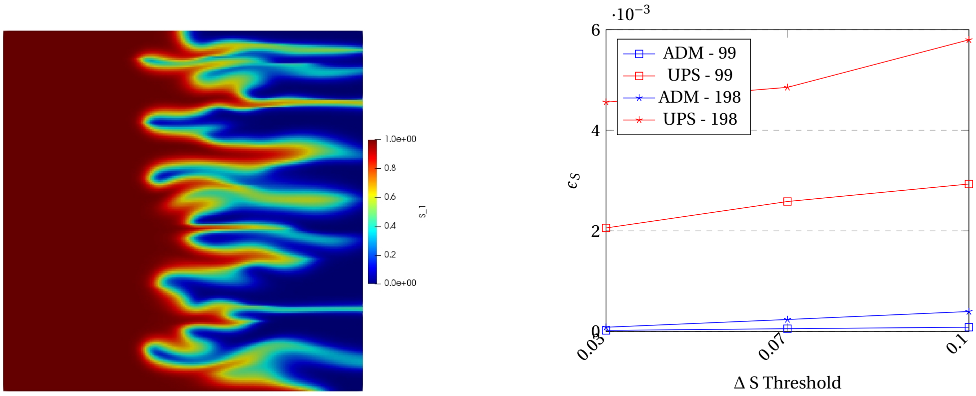

(a) Fine-scale saturation, no dispersion, 198*x*198 grids.

(b) Mean saturation error.

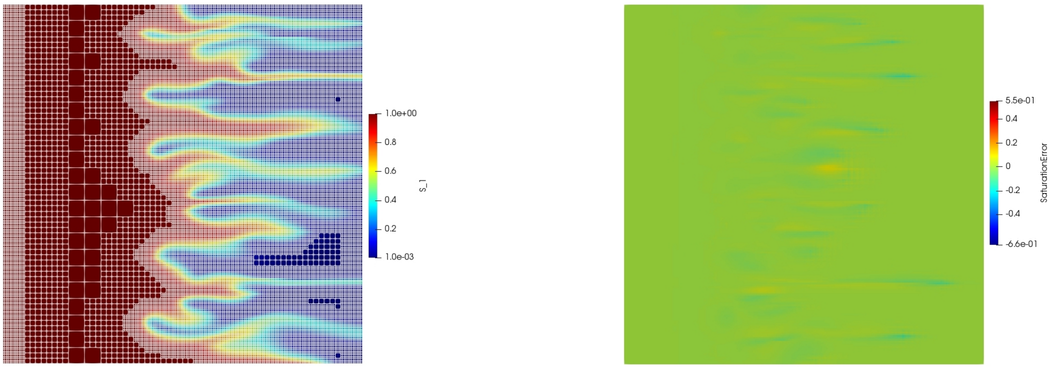

(c) multiscale-based ADM saturation.

(d) multiscale-based ADM saturation error.

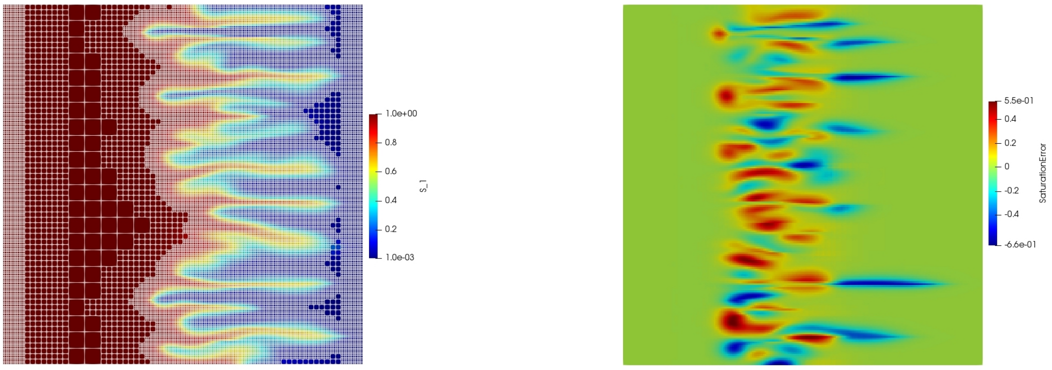

(e) Upscaling-based ADM saturation.

(f) Upscaling-based ADM saturation error.

Figure 6.3: Saturation for fine-scale (a) and ADM approaches. Also shown in sub-figure (b) is the error for different threshold values. Both ADM methods apply 47% of fine-scale cells.

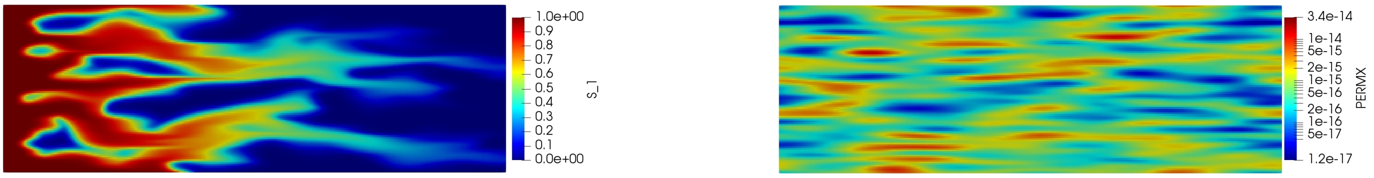

(a) Fine-scale saturation, high dispersion, 297 × 99 cells.

(b) Permeability field.

(c) Multiscale-based ADM saturation.

(d) Multiscale-based ADM saturation error.

(e) Upscaling-based ADM saturation.

(f) Upscaling-based ADM saturation error.

Figure 6.4: Saturation profiles for the fine-scale and ADM methods with $Pe = 1000$ and $\Delta S = 0.1$. Multiscale and upscaling ADM apply 52% and 53% grid cells, respectively.

(a) Fine-scale saturation, medium dispersion, 297 × 99 cells.

(b) Permeability field.

(c) Multiscale-based ADM saturation.

(d) Multiscale-based ADM saturation error.

(e) Upscaling-based ADM saturation.

(f) Upscaling-based ADM saturation error.

Figure 6.5: Saturation profiles for the fine-scale and ADM methods with $Pe = 10000$ and $\Delta S = 0.1$. Multiscale and upscaling ADM apply 65% and 64% grid cells, respectively.

(a) Fine-scale saturation, no dispersion, 297 × 99 cells.

(b) Permeability field.

(c) Multiscale-based ADM saturation.

(d) Multiscale-based ADM saturation error.

(e) Upscaling-based ADM saturation.

(f) Upscaling-based ADM saturation error.

Figure 6.6: Saturation profiles for $Pe = \infty$ and $\Delta S = 0.1$. Both ADM approaches impose 66% active grid cells.

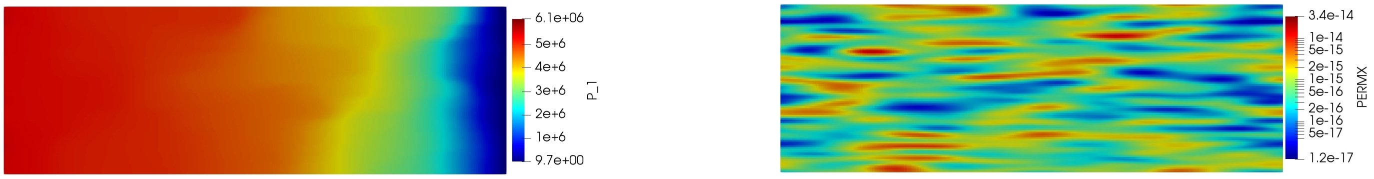

(a) Fine-scale saturation, no dispersion, 297 × 99 cells.

(b) Permeability field.

(c) Multiscale-based ADM pressure.

(d) Multiscale-based ADM pressure error.

(e) Upscaling-based ADM pressure.

(f) Upscaling-based ADM pressure error.

Figure 6.7: Pressure profiles for $Pe = \infty$ and $\Delta S = 0.1$. Both ADM approaches impose 66% active grid cells.

7

Conclusions

The biggest challenge in reservoir simulation is to capture the highest degree of detail and thus reaching the most accurate results while remaining as computational efficient as possible. When simulating the storage of CO_2 in the reservoir considerable challenges are present due to the high mobility of the supercritical CO_2. With this challenge in mind the two simulation methods are being developed and compared to understand which solves the injection and migration process of CO_2 the most accurate. On one hand the Algebraic Dynamic Multilevel approach using Multi-Scale pressure interpolators and secondly an Upscaled-Algebraic Dynamic Multilevel approach using constant pressure interpolators. The ADM approach using pre-processed (calculated only at the first time step) multi-scale pressure interpolators maintains fine-scale heterogeneities during simulations on coarser levels. While the flow-based upscaling approach includes a pre-processing step (calculated only at the first time step) during which effective permeabilities at different levels are calculated. These upscaled effective values have been calculated using a local approach for the considered coarse cell.

Following the development of the previously discussed methods, the methods have been tested on a variety of different settings. Firstly both methods are extensively tested on a variety of permeability fields using a quarter-five spot injection pattern. In total 5 different permeability fields (4 layered with different angles and 1 patchy permeability fields) of which each are tested for 6 different realisations were considered. It is important to be able to estimate the location of the migrating CO_2 as accurately as possible since this can have significant effects over the times-span during which it is stored in the sub-surface.

To gain comprehensive understanding about the both methods, several different sensitivity cases were investigated with different magnitudes of capillarity, mobility ratios and existing reservoir fluid properties. The performance of both methods was tested using number of active cells and error in pressure and saturation and production.

The last section consisted of the research in to a miscible displacement situation in which complex mixing took place. Three cases with a different Péclet number are investigated for a homogeneous and heterogeneous reservoir. The three cases considered situations of no, medium and high dispersion. In the homogeneous case besides the influence of dispersion also the influence of resolution with respect to the performance ADM and Upscaled-based approach has been performed.

Overall, it can be concluded that the multiscale-based ADM approach outperforms the upscaling-based one both in terms of robustness and accuracy of the simulation results. Due to its algebraic (i.e., convenient integration with existing simulators), fully-implicit (stable), and scalable (efficient) characteristics, multiscale-based ADM casts a promising framework for next-generation reservoir simulators.

8

Future Work

This research proves the clear advantage of ADM over classically-imposed upscaling approaches with effective properties at static coarse grid. Here, the upscaling-based approach was also extended into an ADM (multilevel dynamic) grid framework, in order to reduce its errors. Even with ADM advantages, the upscaling-based ADM was found less accurate than multiscale-based ADM. To this end, future studies can be done to test larger domains with 3D geometries. There are several tests that can be performed to improve the current knowledge about the performance of Multiscale-based and upscaling-based ADM approaches. As with all models assumptions are made, future work could be done to reduce the amount of assumptions. In this work isothermal conditions have been assumed, however in true reservoirs isothermal conditions may not exist. The thermal-effect can have significant effects on the flow of CO_2 in the reservoir.

Another interesting topic would be to investigate the performance of both simulation methods with different coarsening/refinement criteria. In this work the coarsening/refinement tolerance is based on saturation difference between neighbouring cells. Other criteria could be the usage of for example time-based criteria. In which coarsening/refinement is based on saturation changes with respect to the previous time step.

Since the static flow-based upscaling method is still widely used in industry, the next challenge to prove the significant advantages of the multi-scale ADM approach would be to demonstrate its speed-up and accuracy performance on a commercial-grade simulator.

Bibliography

[1] Structural trapping. URL `https://www.netl.doe.gov/research/coal/carbon-storage/carbon-storage-faqs/how-is-co2-trapped-in-the-subsurface`.

[2] S Benson, R Pini, C Reynolds, and S Krevor. Relative permeability analysis to describe multi-phase flow in co2 storage reservoirs. *Global CCS Institute*, 2013.

[3] M Bentham and Mg Kirby. Co2 storage in saline aquifers. *Oil & gas science and technology*, 60(3):559–567, 2005.

[4] Suzanne Brunsting, Marjolein de Best-Waldhober, CFJ Ynke Feenstra, and Tom Mikunda. Stakeholder participation practices and onshore ccs: lessons from the dutch ccs case barendrecht. *Energy Procedia*, 4:6376–6383, 2011.

[5] Forrest F Craig. *The reservoir engineering aspects of waterflooding*, volume 3. HL Doherty Memorial Fund of AIME New York, 1971.

[6] Matteo Cusini, Cor van Kruijsdijk, and Hadi Hajibeygi. Algebraic dynamic multilevel (adm) method for fully implicit simulations of multiphase flow in porous media. 314, 03 2016.

[7] Heleen de Coninck and Sally M Benson. Carbon dioxide capture and storage: issues and prospects. *Annual review of environment and resources*, 39:243–270, 2014.

[8] Francis AL Dullien. *Porous Media Fluid Transport and Pore Structure*. Academic San Diego, 1992.

[9] Hamid Emami-Meybodi, Hassan Hassanzadeh, Christopher P. Green, and Jonathan Ennis-King. Convective dissolution of co2 in saline aquifers: Progress in modeling and experiments. *International Journal of Greenhouse Gas Control*, 40:238 – 266, 2015. ISSN 1750-5836. doi: https://doi.org/10.1016/j.ijggc.2015.04.003. URL `http://www.sciencedirect.com/science/article/pii/S1750583615001450`. Special Issue commemorating the 10th year anniversary of the publication of the Intergovernmental Panel on Climate Change Special Report on CO2 Capture and Storage.

[10] CFJ Feenstra, T Mikunda, and S Brunsting. What happened in barendrecht. *Case study on the planned onshore carbon dioxide storage in Barendrecht, the Netherlands. Prepared by the Energy research Centre of the Netherlands (ECN) Project*, 6, 2010.

[11] R.A.M. Gielisse. Dynamic local grid refinement for incomplete mixing in reservoir simulation. *MSc Thesis*, Oct 2015.

[12] George M Homsy. Viscous fingering in porous media. *Annual review of fluid mechanics*, 19(1):271–311, 1987.

[13] Richard D Hornung and John A Trangenstein. Adaptive mesh refinement and multilevel iteration for flow in porous media. *Journal of computational Physics*, 136(2):522–545, 1997.

[14] International Energy Agency (IEA). Recent trends in the oecd: energy and co−2 emissions. Technical report, International Energy Agency (IEA), 2005.

[15] P Jenny, SH Lee, and HA Tchelepi. Multi-scale finite-volume method for elliptic problems in subsurface flow simulation. *Journal of Computational Physics*, 187(1):47–67, 2003.

[16] M.A. Celia J.M. Nordbotten. *Geological storage of CO2: modeling approaches for large-scale simulation*. Cambridge University Press, 2011.

[17] Ruben Juanes, EJ Spiteri, FM Orr, and MJ Blunt. Impact of relative permeability hysteresis on geological co2 storage. *Water Resources Research*, 42(12), 2006.

[18] E.J. Koval. A method for predicting the performance of unstable miscible displacement in heterogeneous media. *Society of Petroleum Engineers*, 3(2):145–154, Jun 1963. ISSN 0197-7520. URL `https://doi.org/10.2118/450-PA`.

[19] Samuel Krevor, Martin J Blunt, Sally M Benson, Christopher H Pentland, Catriona Reynolds, Ali Al-Menhali, and Ben Niu. Capillary trapping for geologic carbon dioxide storage–from pore scale physics to field scale implications. *International Journal of Greenhouse Gas Control*, 40:221–237, 2015.

[20] Larry W Lake. Enhanced oil recovery. 1989.

[21] I. S. Ligaarden and H. M. Nilsen. Numerical aspects of using vertical equilibrium models for simulating co2 sequestration. *Proceedings of ECMOR XII*, Sept 2010. doi: 10.3997/2214-4609.20144940.

[22] CW MacMinn, ML Szulczewski, and R Juanes. Co2 migration in saline aquifers. part 2. capillary and solubility trapping. *Journal of Fluid Mechanics*, 688:321–351, 2011.

[23] D.W. van Batenburg J.Vink M.B.P.M Boerrigter, A.H. de Zwart. Application of dynamic gridding techniques to ior/eor-processes. *SPE Reservoir Simulation Symposium Texas, USA*, 21-23 February 2011.

[24] Bert Metz, Ogunlade Davidson, Heleen De Coninck, Manuela Loos, and Leo Meyer. Ipcc special report on carbon dioxide capture and storage. Technical report, Intergovernmental Panel on Climate Change, Geneva (Switzerland). Working Group III, 2005.

[25] Olav MÃžyner and Halvor Nilsen. Multiresolution coupled vertical equilibrium model for fast flexible simulation of co$_2$ storage. 10 2017.

[26] Halvor Møll Nilsen, Knut-Andreas Lie, and Odd Andersen. Fully-implicit simulation of vertical-equilibrium models with hysteresis and capillary fringe. *Computational Geosciences*, 20(1):49–67, Feb 2016. ISSN 1573-1499. doi: 10.1007/s10596-015-9547-y. URL `https://doi.org/10.1007/s10596-015-9547-y`.

[27] Intergovernmental Panel on Climate Change. *Climate change 2014: mitigation of climate change*, volume 3. Cambridge University Press, 2015.

[28] D. W. Peaceman and Jr. Rachford, H. H. Numerical calculation of multidimensional miscible displacement. *Society of Petroleum Engineers*, Dec 1962. doi: 10.2118/471-PA. URL `http://dx.doi.org/10.2118/471-PA`.

[29] Catherine Ruprecht, Ronny Pini, Ronald Falta, Sally Benson, and Lawrence Murdoch. Hysteretic trapping and relative permeability of co 2 in sandstone at reservoir conditions. *International Journal of Greenhouse Gas Control*, 27:15–27, 2014.

[30] UFCCC. Paris agreement. 2016.

[31] Per H Valvatne and Martin J Blunt. Predictive pore-scale modeling of two-phase flow in mixed wet media. *Water Resources Research*, 40(7), 2004.

[32] Yixuan Wang, Hadi Hajibeygi, and Hamdi A. Tchelepi. Algebraic multiscale solver for flow in heterogeneous porous media. *Journal of Computational Physics*, 259(Supplement C):284 – 303, 2014. ISSN 0021-9991. doi: https://doi.org/10.1016/j.jcp.2013.11.024. URL `http://www.sciencedirect.com/science/article/pii/S0021999113007869`.

[33] Yixuan Wang, Hadi Hajibeygi, and Hamdi A Tchelepi. Algebraic multiscale solver for flow in heterogeneous porous media. *Journal of Computational Physics*, 259:284–303, 2014.

[34] Tianfu Xu, John A Apps, and Karsten Pruess. Reactive geochemical transport simulation to study mineral trapping for co2 disposal in deep arenaceous formations. *Journal of Geophysical Research: Solid Earth*, 108(B2), 2003.

A

First Appendix: influence of Capillary Pressure

A.1. Simulation Parameters

Table A.1: Parameters used for simulations.

Variable	**Value**	**Unit**
Porosity: ϕ	0.221	volume fraction (%)
Temperature: T	323.15	K
Density CO_2: ρ_{CO_2}	280	kg/m^3
Density brine: ρ_{brine}	992	kg/m^3
Viscosity CO_2: μ_{CO_2}	$2.3 \cdot 10^{-5}$	$Pa \cdot sec$
Viscosity brine: μ_{brine}	$5.5 \cdot 10^{-5}$	$Pa \cdot sec$]
Initial Reservoir Pressure: $P_{res,init}$	90	Bar
Initial CO_2 Saturation: S_{CO_2}	0.0	%
Initial Brine Saturation: S_{brine}	0.1	%
Fine Scale Resolution	99 × 99 × 1	(x,y,z) gridblocks
Level 1 Resolution	33 × 33 × 1	(x,y,z) gridblocks
Level 2 Resolution	11 × 11 × 1	(x,y,z) gridblocks
Simulation Time	12	days
Injection Rate	0.25	PV/day
Relative Permeability Curve	Quadratic	
ADM Pressure Interpolator	Multi-Scale	
Upscaling Pressure Interpolator	Constant	

A.2. Active Cells

(a) Number of cells per level represented in A.1a.

Δ S Threshold Value	**FS cells**		**Level 1 cells**		**Level 2 cells**	
	ADM	**UPS**	**ADM**	**UPS**	**ADM**	**UPS**
0.03: Absolute number of cells	4718	4510	183	198	42	43
% of Active FS cells	48.14%	46.02%	1.87%	2.02%	0.43%	0.44%
0.05: Absolute number of cells	3854	3334	244	290	46	48
% of Active FS cells	39.32%	34.02%	2.49%	2.96%	0.47%	0.49%
0.07: Absolute number of cells	2972	2384	303	354	51	52
% of Active FS cells	30.32%	24.32%	3.09%	3.61 %	0.52%	0.53%
0.1: Absolute number of cells	1960	1513	356	392	57	59
% of Active FS cells	19.99%	15.44%	3.63%	3.99%	0.58%	0.60%
0.3: Absolute number of cells	304	340	255	242	89	90
% of Active FS cells	3.10%	3.47%	2.60%	2.47%	0.92%	0.92%

(b) Number of cells per level represented in A.1b.

Δ S Threshold Value	**FS cells**		**Level 1 cells**		**Level 2 cells**	
	ADM	**UPS**	**ADM**	**UPS**	**ADM**	**UPS**
0.03: Absolute number of cells	4718	4510	183	198	42	43
% of Active FS cells	48.14%	46.02%	1.87%	2.02%	0.43%	0.44%
0.05: Absolute number of cells	3854	3334	244	290	46	48
% of Active FS cells	39.32%	34.02%	2.49%	2.96%	0.47%	0.49%
0.07: Absolute number of cells	2972	2384	303	354	51	52
% of Active FS cells	30.32%	24.32%	3.09%	3.61 %	0.52%	0.53%
0.1: Absolute number of cells	1960	1513	356	392	57	59
% of Active FS cells	19.99%	15.44%	3.63%	3.99%	0.58%	0.60%
0.3: Absolute number of cells	304	340	255	242	89	90
% of Active FS cells	3.10%	3.47%	2.60%	2.47%	0.92%	0.92%

(a) Number of cells per level represented in A.1c.

Δ S Threshold Value	**FS cells**		**Level 1 cells**		**Level 2 cells**	
	ADM	**UPS**	**ADM**	**UPS**	**ADM**	**UPS**
0.03: Absolute number of cells	4718	4510	183	198	42	43
% of Active FS cells	48.14%	46.02%	1.87%	2.02%	0.43%	0.44%
0.05: Absolute number of cells	3854	3334	244	290	46	48
% of Active FS cells	39.32%	34.02%	2.49%	2.96%	0.47%	0.49%
0.07: Absolute number of cells	2972	2384	303	354	51	52
% of Active FS cells	30.32%	24.32%	3.09%	3.61 %	0.52%	0.53%
0.1: Absolute number of cells	1960	1513	356	392	57	59
% of Active FS cells	19.99%	15.44%	3.63%	3.99%	0.58%	0.60%
0.3: Absolute number of cells	304	340	255	242	89	90
% of Active FS cells	3.10%	3.47%	2.60%	2.47%	0.92%	0.92%

(b) Number of cells per level represented in A.1d.

Δ S Threshold Value	**FS cells**		**Level 1 cells**		**Level 2 cells**	
	ADM	**UPS**	**ADM**	**UPS**	**ADM**	**UPS**
0.03: Absolute number of cells	4822	4837	172	162	42	43
% of Active FS cells	49.20%	49.35%	1.75%	1.65%	0.43%	0.44%
0.05: Absolute number of cells	4003	4021	225	216	47	47
% of Active FS cells	40.84%	41.03%	2.30%	2.20%	0.48%	0.48%
0.07: Absolute number of cells	3100	3033	289	284	51	52
% of Active FS cells	31.63%	30.95%	2.95%	2.90%	0.52%	0.53%
0.1: Absolute number of cells	2035	1851	347	365	57	58
% of Active FS cells	20.76%	18.89%	3.54%	3.72%	0.58%	0.59%
0.3: Absolute number of cells	304	368	256	247	89	89
% of Active FS cells	3.10%	3.75%	2.61%	2.52%	0.91%	0.91%

(a) Number of cells per level represented in A.1e.

Δ S Threshold Value	**FS cells**		**Level 1 cells**		**Level 2 cells**	
	ADM	**UPS**	**ADM**	**UPS**	**ADM**	**UPS**
0.03: Absolute number of cells	4718	4510	183	198	42	43
% of Active FS cells	48.14%	46.02%	1.87%	2.02%	0.43%	0.44%
0.05: Absolute number of cells	3854	3334	244	290	46	48
% of Active FS cells	39.32%	34.02%	2.49%	2.96%	0.47%	0.49%
0.07: Absolute number of cells	2972	2384	303	354	51	52
% of Active FS cells	30.32%	24.32%	3.09%	3.61 %	0.52%	0.53%
0.1: Absolute number of cells	1960	1513	356	392	57	59
% of Active FS cells	19.99%	15.44%	3.63%	3.99%	0.58%	0.60%
0.3: Absolute number of cells	304	340	255	242	89	90
% of Active FS cells	3.10%	3.47%	2.60%	2.47%	0.92%	0.92%

(b) Number of cells per level represented in A.1f.

Δ S Threshold Value	**FS cells**		**Level 1 cells**		**Level 2 cells**	
	ADM	**UPS**	**ADM**	**UPS**	**ADM**	**UPS**
0.03: Absolute number of cells	6917	7753	88	58	26	19
% of Active FS cells	70.57%	79.10%	0.90%	0.59%	0.27%	0.19%
0.05: Absolute number of cells	6665	7756	97	67	28	18
% of Active FS cells	68.00%	79.14%	0.99%	0.68%	0.29%	0.18%
0.07: Absolute number of cells	7607	8325	83	55	18	12
% of Active FS cells	77.62%	84.94%	0.85%	0.56%	0.18%	0.12%
0.1: Absolute number of cells	6510	8348	143	68	25	10
% of Active FS cells	66.42%	85.18%	1.46%	0.69%	0.26%	0.10%
0.3: Absolute number of cells	448	368	270	317	85	87
% of Active FS cells	4.57%	3.75%	2.75%	3.23%	0.91%	0.92%

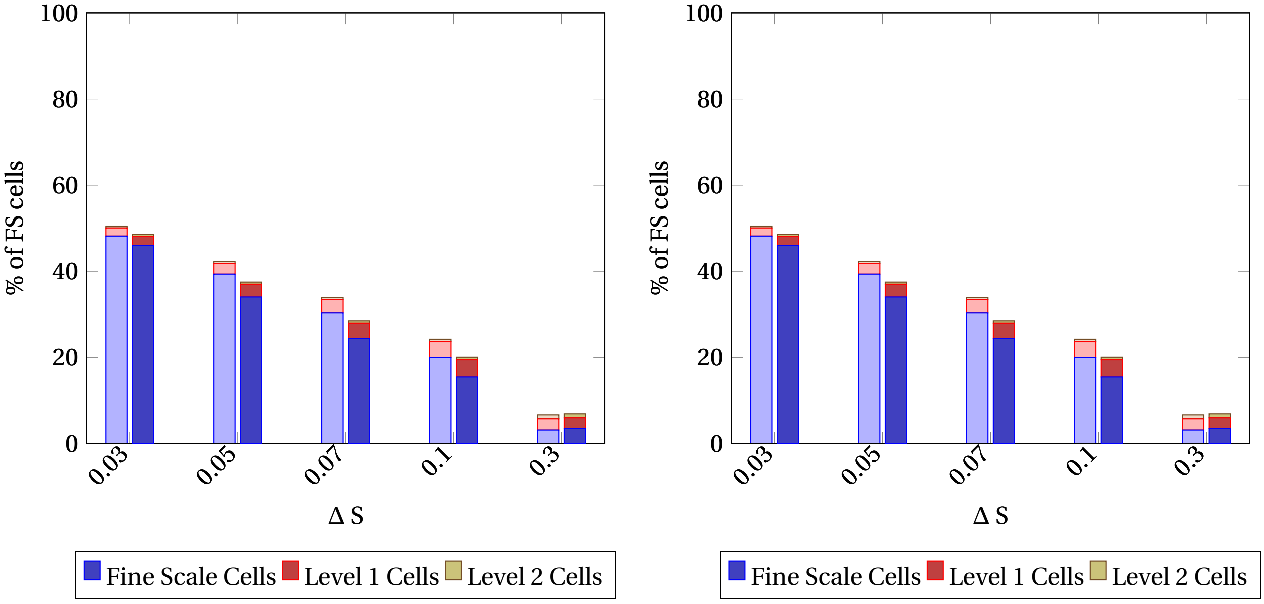

(a) Excluding capillary pressure, interfacial tension 1.

(b) Including capillary pressure, high capillary number.

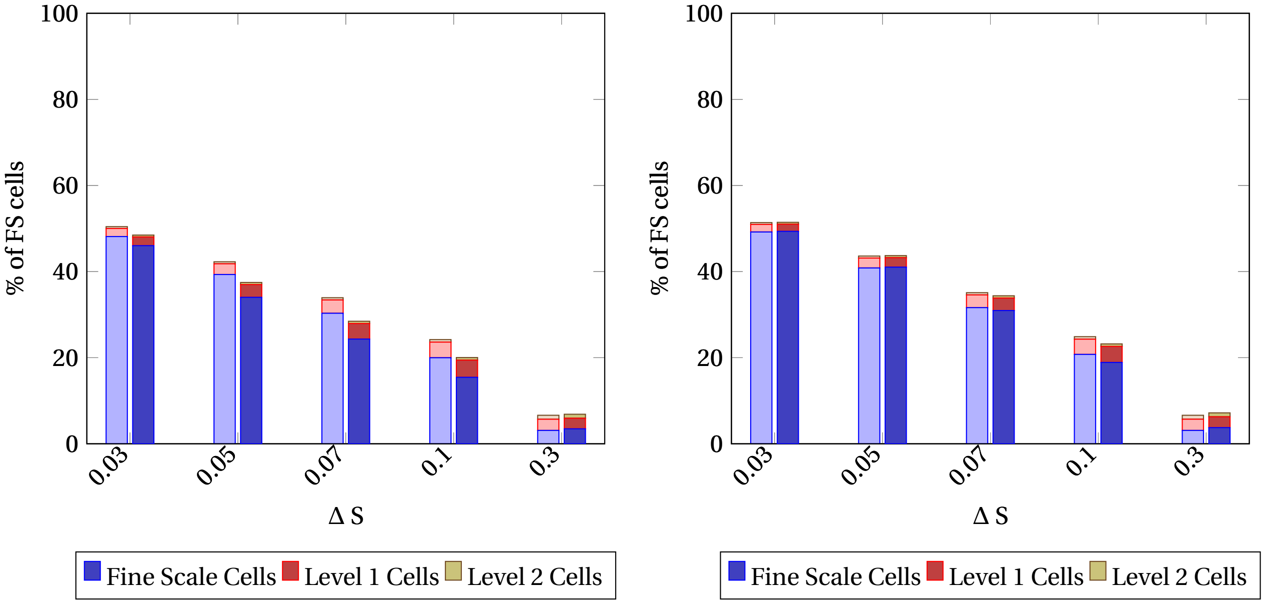

(c) Excluding capillarity, interfacial tension 2.

(d) Including capillarity, medium capillary number.

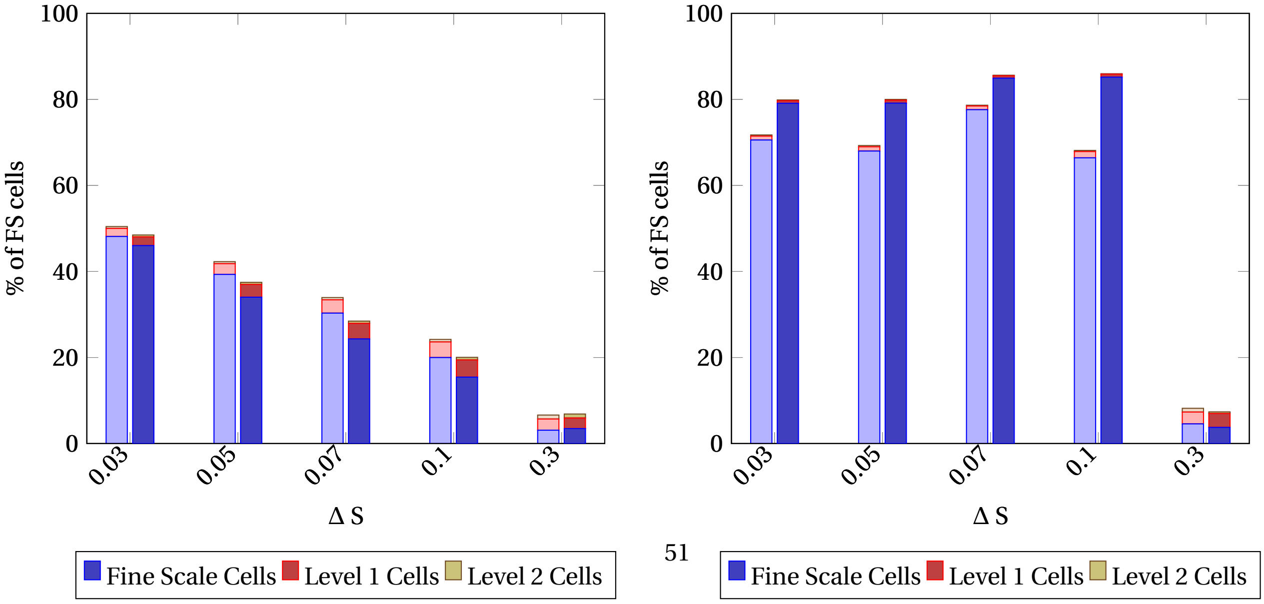

(e) Excluding capillarity, interfacial tension 3.

(f) Including capillarity, low capillary number.

Figure A.1: 45° Permeability field: % of active cells of fine-scale simulation per Level ADM (left bar) vs Upscaling (right bar).

A.3. Pressure & saturation error results

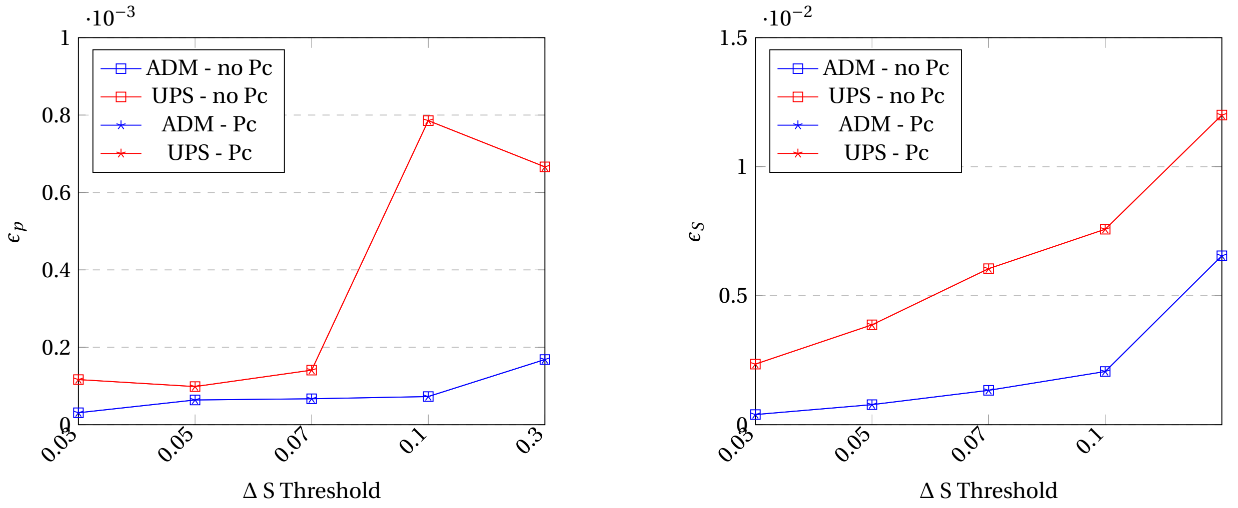

(a) High capillary number: mean error pressure

(b) High capillary number: mean error saturation

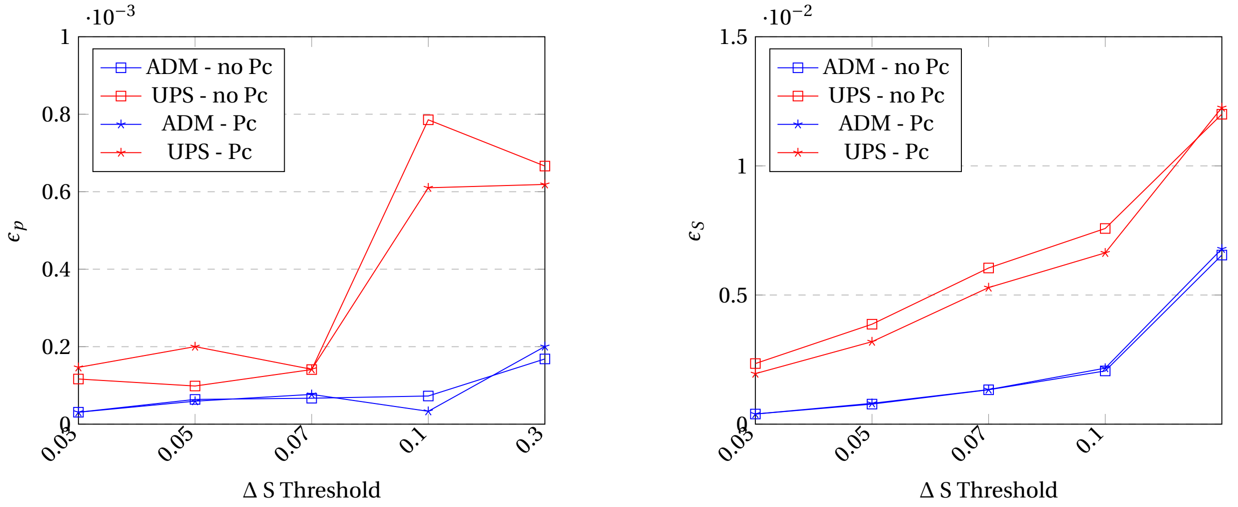

(c) Medium capillary number: mean error pressure

(d) Medium capillary number: mean error saturation

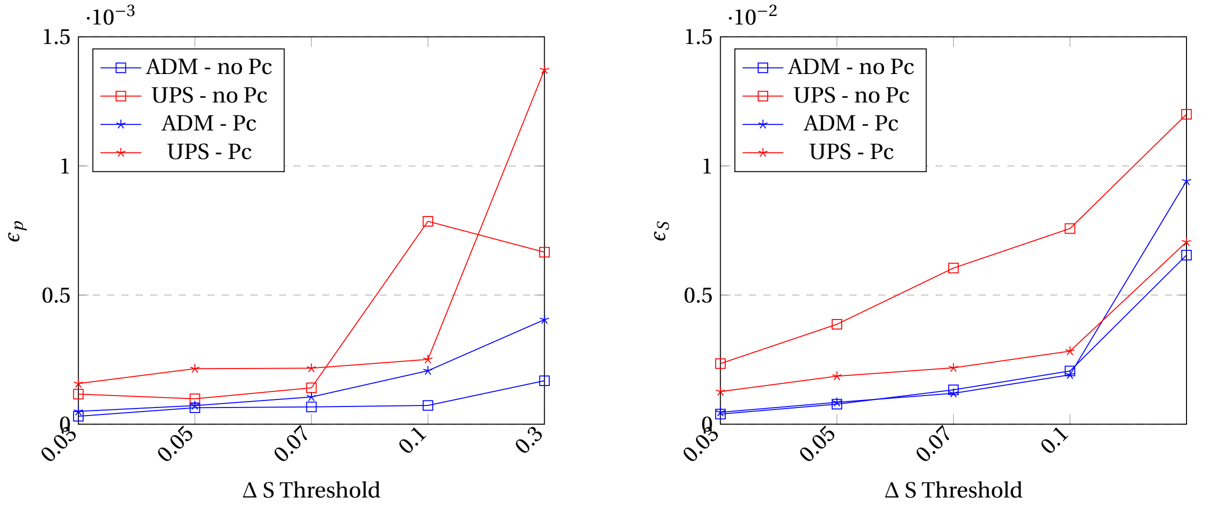

(e) Low capillary number: mean error pressure

(f) Low capillary number: mean error saturation

Figure A.2: Pressure and saturation error for cases with and without capillarity and decreasing capillary numbers.

A.4. Production error results

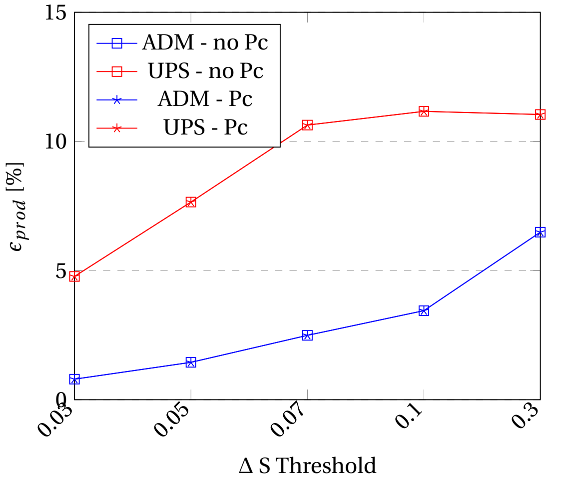

(a) High capillary number: percentual mean error production.

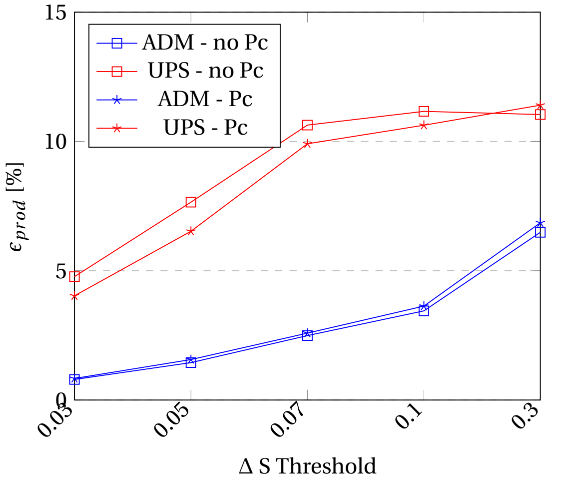

(b) Medium capillary number: percentual mean error production.

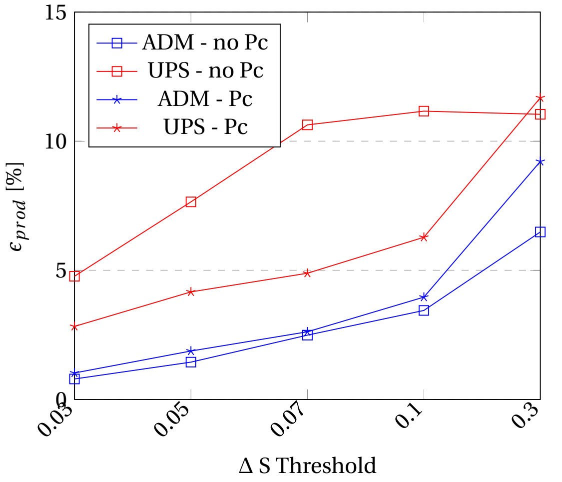

(c) Low capillary number: percentual mean error production.

Figure A.3: Percentual mean error production for low, medium and high capillary numbers.

B

Second Appendix: Viscosity Sensitivity

B.1. Simulation parameters

Table B.1: Parameters used for simulations.

Variable	**Value**	**Unit**
Porosity: ϕ	0.221	volume fraction (%)
Temperature: T	323.15	K
Density CO_2: ρ_{CO_2}	280	kg/m^3
Density brine: ρ_{brine}	992	kg/m^3
Viscosity brine: μ_{brine}	$5.5 \cdot 10^{-5}$	$Pa \cdot sec$
Initial Reservoir Pressure: $P_{res,init}$	90	Bar
Initial CO_2 Saturation: S_{CO_2}	0.0	%
Initial Brine Saturation: S_{brine}	1.0	%
Fine Scale Resolution	99 × 99 × 1	(x,y,z) gridblocks
Level 1 Resolution	33 × 33 × 1	(x,y,z) gridblocks
Level 2 Resolution	11 × 11 × 1	(x,y,z) gridblocks
Simulation Time	12	days
Relative Permeability Curve	Quadratic	
ADM Pressure Interpolator	Multi-Scale	
Upscaling Pressure Interpolator	Constant	
Δ S Tolerance	0.07	
Injection Rate S Tolerance	1.5	Pore-Volumes

B.2. Active Cells ADM versus Upscaled Method

B.2.1. 15° Permeability field

Table B.2: Number of cells per level represented in B.1.

Effective Mobility (*M*)	**FS cells**		**Level 1 cells**		**Level 2 cells**	
	ADM	**UPS**	**ADM**	**UPS**	**ADM**	**UPS**
0.5: Absolute number of cells	1124	1270	249	271	79	75
% of Active FS cells	11.47%	12.96%	2.54%	2.77%	0.81%	0.77%
1: Absolute number of cells	1450	1491	291	299	71	70
% of Active FS cells	14.79%	15.21%	2.97%	3.05 %	0.72%	0.71%
5: Absolute number of cells	2386	2583	368	363	51	49
% of Active FS cells	24.34%	26.35%	3.75 %	3.70 %	0.52 %	0.49 %
10: Absolute number of cells	1931	2064	342	346	59	57
% of Active FS cells	19.70 %	21.059 %	3.48 %	3.53 %	0.60%	0.58%
24: Absolute number of cells	3285	3502	339	315	43	43
% of Active FS cells	33.52 %	35.73 %	3.46 %	3.21 %	0.44 %	0.44 %

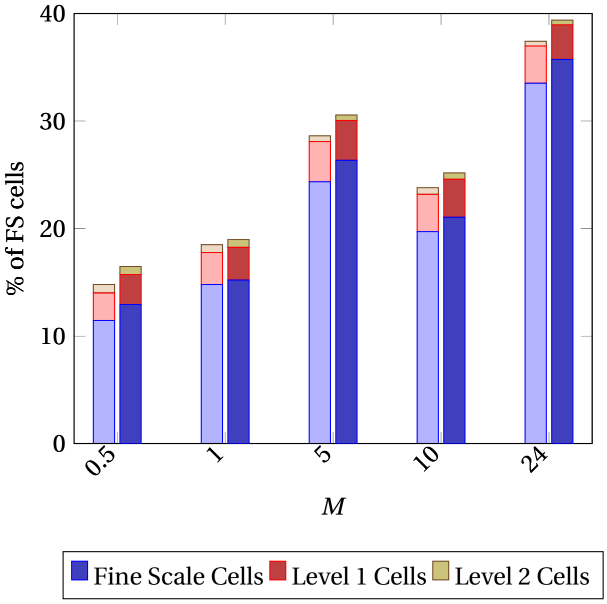

Figure B.1: 15° Permeability field: % of active cells of fine-scale simulation per Level ADM (left bar) vs Upscaling (right bar).

B.2.2. 30° Permeability field

Table B.3: Number of cells per level represented in B.1.

Effective Mobility (M)	**FS cells**		**Level 1 cells**		**Level 2 cells**	
	ADM	**UPS**	**ADM**	**UPS**	**ADM**	**UPS**
0.5: Absolute number of cells	1337	1259	292	277	72	75
% of Active FS cells	13.64%	12.85%	2.98%	2.83%	0.73%	0.77%
1: Absolute number of cells	1709	1645	324	307	64	67
% of Active FS cells	17.44%	16.78%	3.31%	3.13%	0.65%	0.68%
5: Absolute number of cells	2817	2722	347	351	48	48
% of Active FS cells	28.74%	27.77%	3.54%	3.58%	0.49%	0.49%
10: Absolute number of cells	2308	2180	348	349	54	55
% of Active FS cells	23.55 %	22.24 %	3.55 %	3.56 %	0.5 %	0.56%
24: Absolute number of cells	3743	3561	300	310	41	43
% of Active FS cells	38.19 %	36.33 %	3.06 %	3.16 %	0.42 %	0.44 %

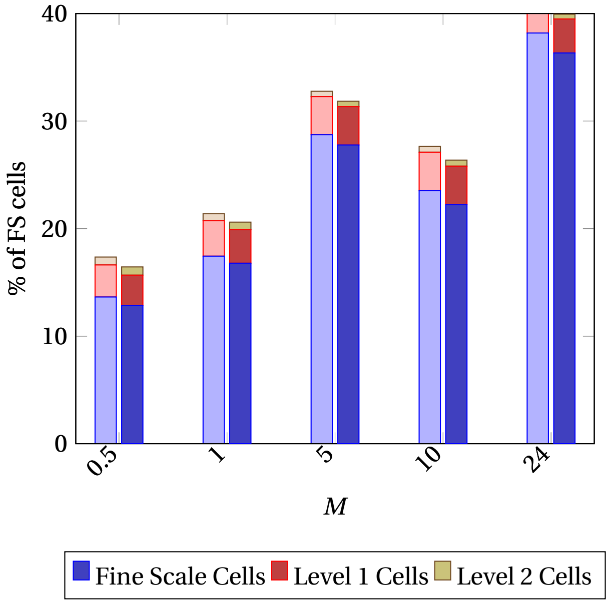

Figure B.2: 30° Permeability field: % of active cells of fine-scale simulation per Level ADM (left bar) vs Upscaling (right bar).

B.2.3. 45° **Permeability field**

Table B.4: Number of cells per level represented in B.3.

Effective Mobility (*M*)	**FS cells**		**Level 1 cells**		**Level 2 cells**	
	ADM	**UPS**	**ADM**	**UPS**	**ADM**	**UPS**
0.5: Absolute number of cells	1498	1377	314	287	68	72
% of Active FS cells	15.28%	12.85%	2.98%	2.8262%	0.73%	0.77%
1: Absolute number of cells	1905	1769	333	316	60	64
% of Active FS cells	19.44%	18.045%	3.40%	3.22%	0.61%	0.65%
5: Absolute number of cells	3232	2883	334	349	44	47
% of Active FS cells	32.98%	29.42%	3.41%	3.56%	0.45 %	0.48%
10: Absolute number of cells	2632	2348	344	346	50	54
% of Active FS cells	26.85 %	23.96 %	3.51 %	3.53 %	0.51 %	0.55%
24: Absolute number of cells	4053	3691	270	302	41	42
% of Active FS cells	41.35 %	37.66 %	2.75 %	3.08 %	0.42 %	0.43 %

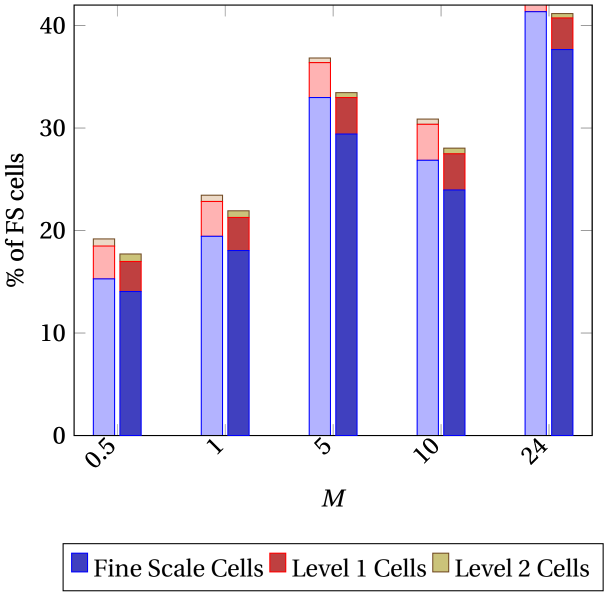

Figure B.3: 45° Permeability field: % of active cells of fine-scale simulation per Level ADM (left bar) vs Upscaling (right bar).

B.2.4. 98° Permeability field

Table B.5: Number of cells per level represented in B.4.

Effective Mobility (M)	**FS cells**		**Level 1 cells**		**Level 2 cells**	
	ADM	**UPS**	**ADM**	**UPS**	**ADM**	**UPS**
0.5: Absolute number of cells	1137	1083	225	232	82	82
% of Active FS cells	11.60%	11.05%	2.29%	2.36%	0.84%	0.84%
1: Absolute number of cells	1361	1348	251	254	76	76
% of Active FS cells	13.89%	13.75%	2.56%	2.59%	0.78%	0.78%
5: Absolute number of cells	2343	2398	348	357	53	52
% of Active FS cells	23.91%	24.47%	3.55%	3.64%	0.54 %	0.53%
10: Absolute number of cells	1822	1869	306	321	64	62
% of Active FS cells	18.59 %	19.07 %	3.12 %	3.28%	0.65 %	0.63%
24: Absolute number of cells	3868	3719	276	292	43	43
% of Active FS cells	39.47 %	37.95 %	2.82 %	2.98 %	0.44 %	0.44 %

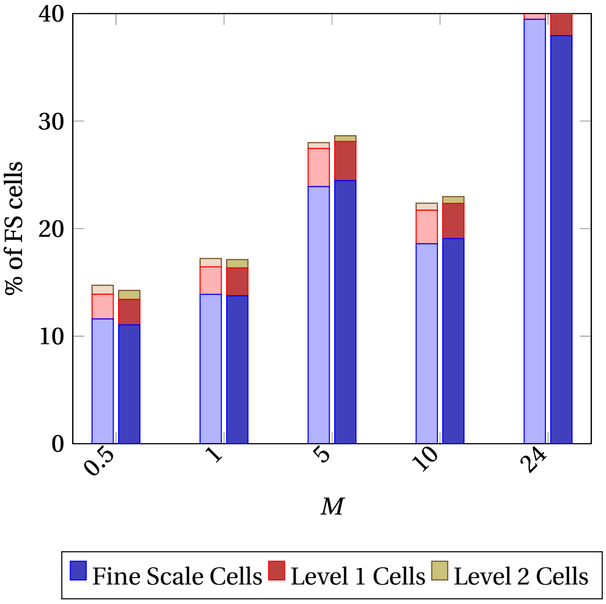

Figure B.4: 98° Permeability field: % of active cells of fine-scale simulation per Level ADM (left bar) vs Upscaling (right bar).

B.3. Pressure & saturation error results

B.3.1. 15° Permeability field

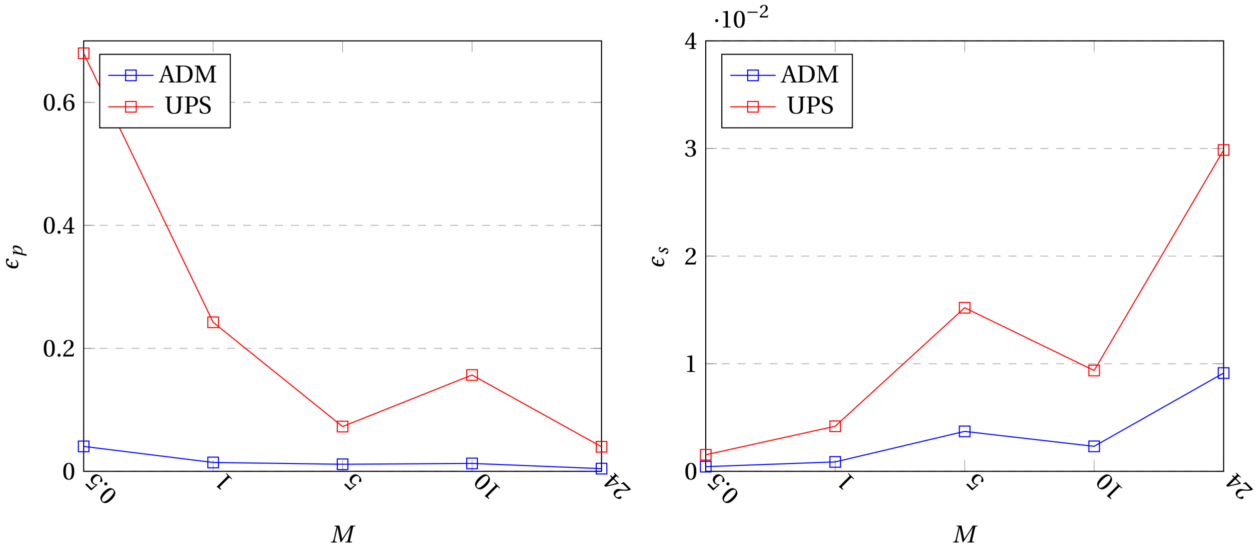

(a) 15° Permeability field: mean error pressure

(b) 15° Permeability field: mean error saturation

Figure B.5: Pressure and saturation error.

B.3.2. 30° Permeability field

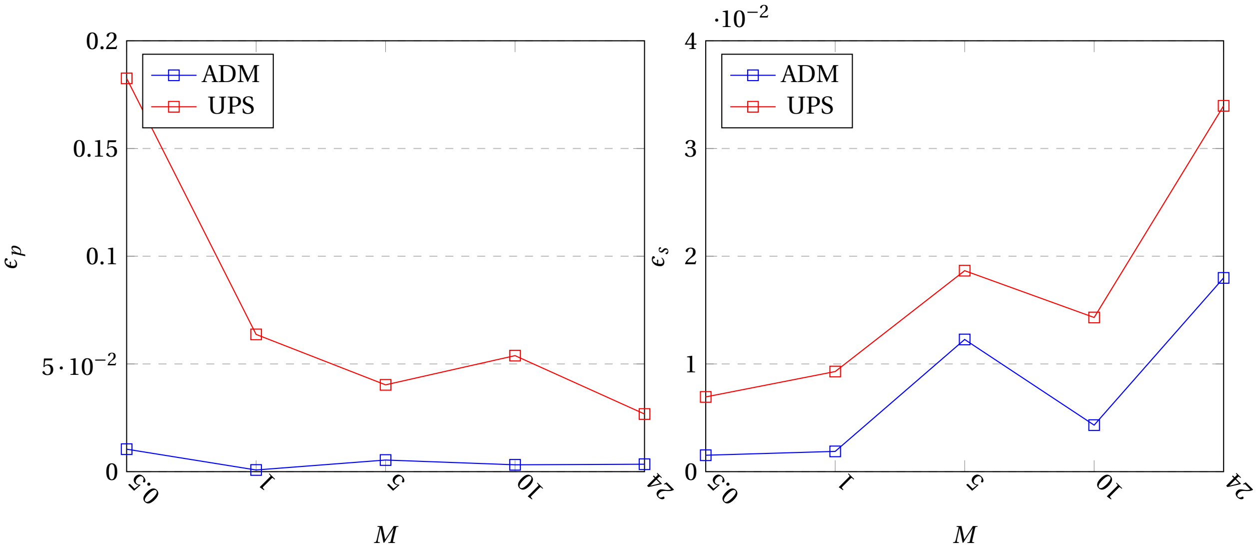

(a) 30° Permeability field: mean error pressure

(b) 30° Permeability field: mean error saturation.

Figure B.6: Pressure and saturation error.

B.3.3. 45° Permeability field

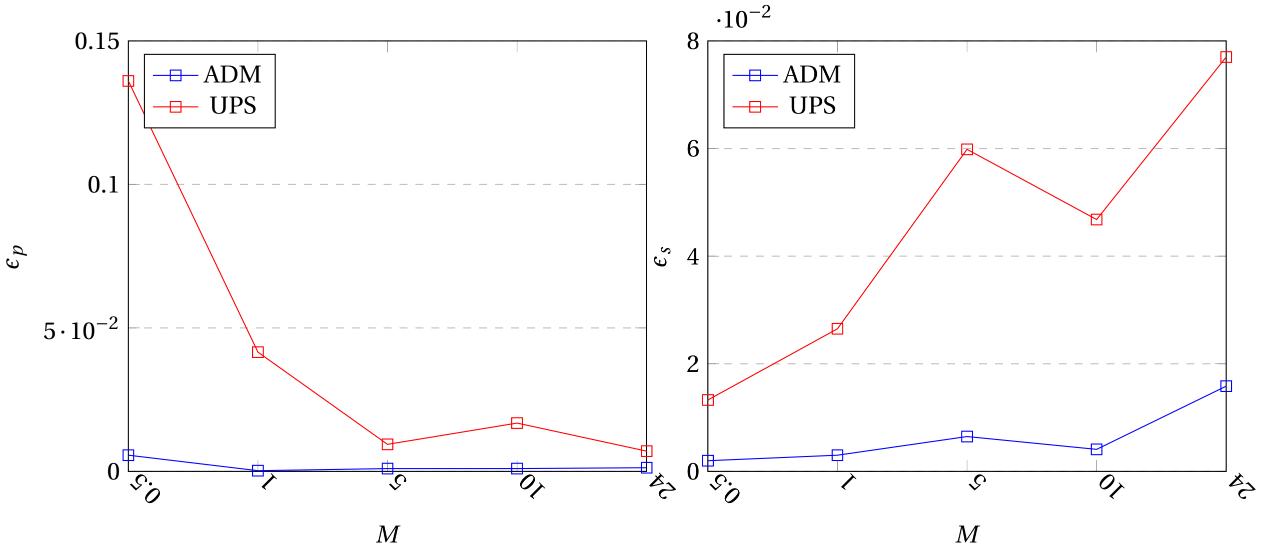

(a) 45° Permeability field: mean error pressure

(b) 45° Permeability field: mean error saturation

Figure B.7: Pressure and saturation error.

B.3.4. 98° Permeability field

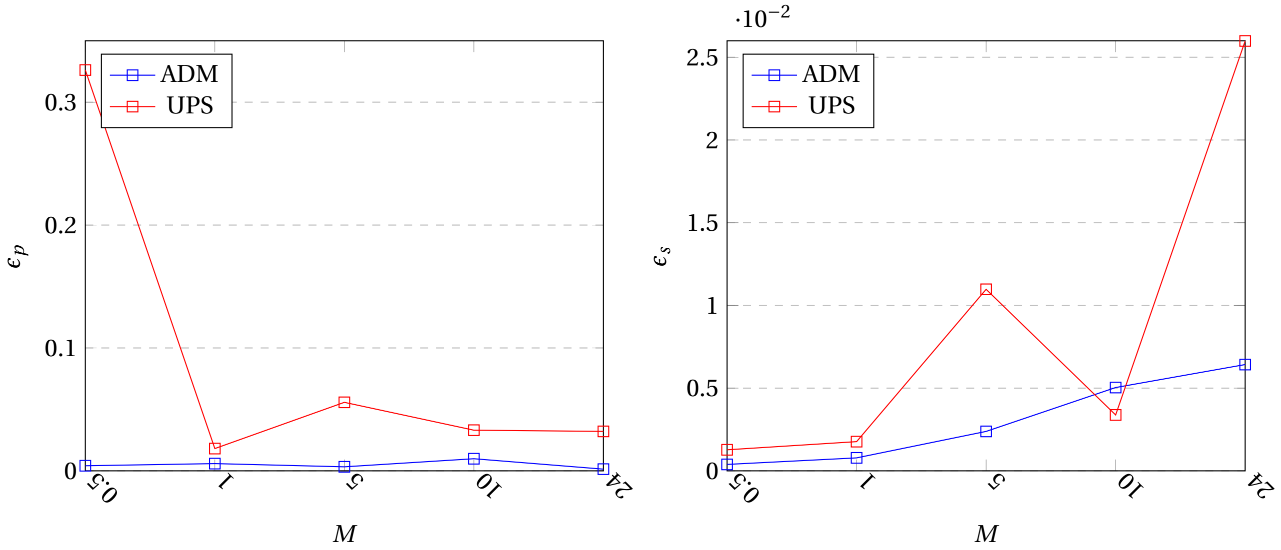

(a) 98° Permeability field: mean error pressure

(b) 98° Permeability field: mean error saturation

Figure B.8: Pressure and saturation error.

B.4. Production error results

B.4.1. 15° & 30° Permeability field

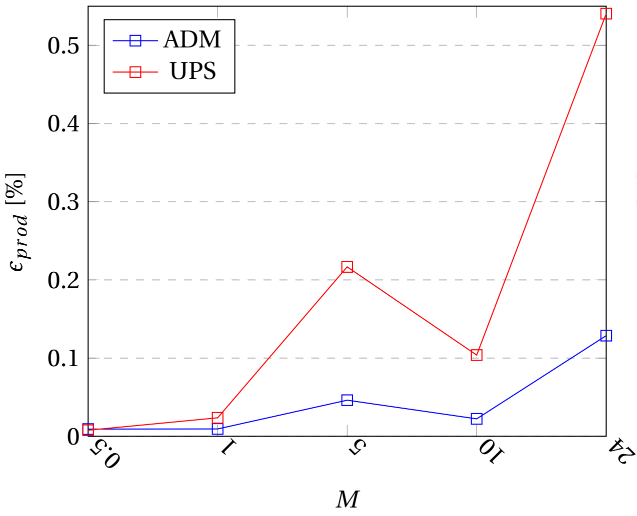

(a) 15° Permeability field: percentual mean error production.

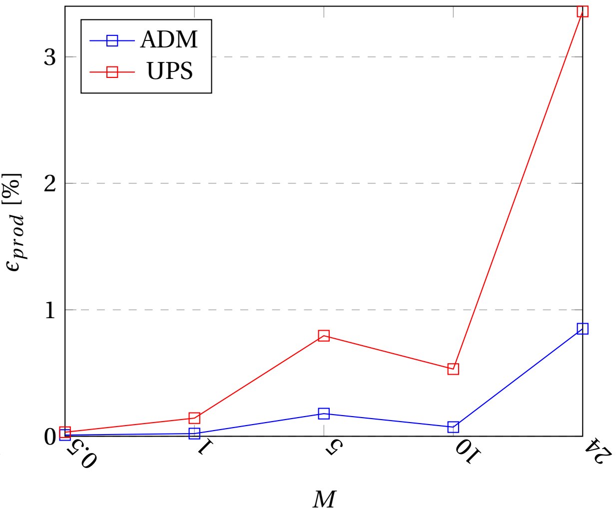

(b) 30° Permeability field: percentual mean error production.

B.4.2. 45° **&** 98° **Permeability field**

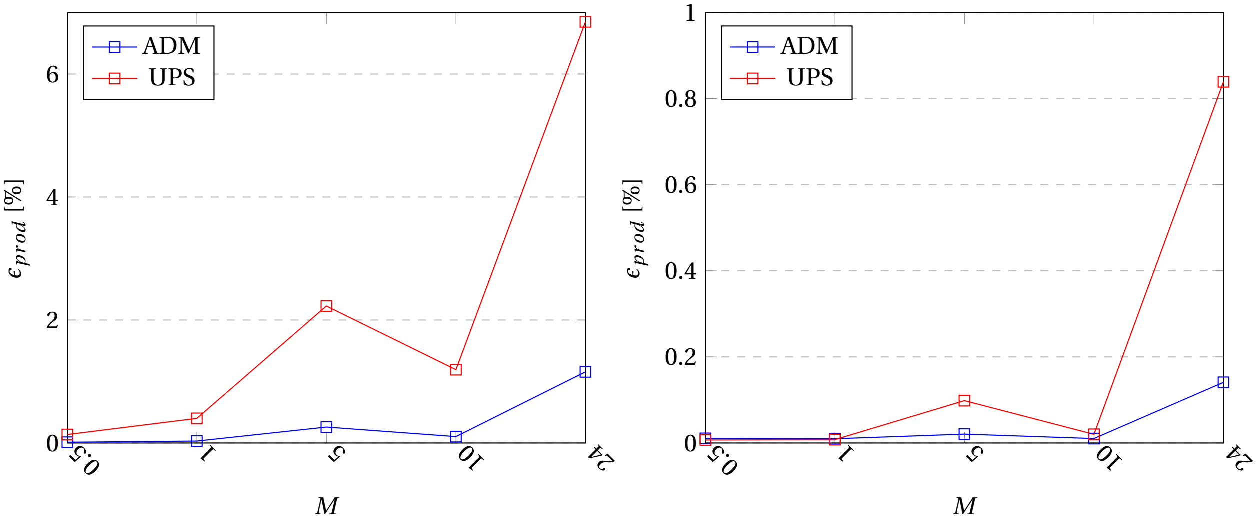

(a) 45° Permeability field: percentual mean error production.

(b) 98° Permeability field: percentual mean error production.

C

Third Appendix: Porosity Sensitivity

C.1. Simulation parameters

Table C.1: Parameters used for simulations.

Variable	**Value**	**Unit**
Temperature: T	323.15	K
Density CO_2: ρ_{CO_2}	280	kg/m^3
Density brine: ρ_{brine}	992	kg/m^3
Viscosity brine: μ_{brine}	$5.5 \cdot 10^{-5}$	$Pa \cdot sec$
Viscosity CO_2: μCO_2	$2.3 \cdot 10^{-5}$	$Pa \cdot sec$
Initial Reservoir Pressure: $P_{res,init}$	90	Bar
Initial CO_2 Saturation: S_{CO_2}	0.0	%
Initial Brine Saturation: S_{brine}	1.0	%
Fine Scale Resolution	99 × 99 × 1	(x,y,z) gridblocks
Level 1 Resolution	33 × 33 × 1	(x,y,z) gridblocks
Level 2 Resolution	11 × 11 × 1	(x,y,z) gridblocks
Simulation Time	12	days
Relative Permeability Curve	Quadratic	
ADM Pressure Interpolator	Multi-Scale	
Upscaling Pressure Interpolator	Constant	
Δ S Tolerance	0.07	
Injection Rate S Tolerance	1.5	Pore-Volumes

C.2. Active Cells ADM versus Upscaled Method

C.2.1. 15° Permeability field

Table C.2: Number of cells per level represented in C.1.

Porosity (ϕ)	**FS cells**		**Level 1 cells**		**Level 2 cells**	
	ADM	**UPS**	**ADM**	**UPS**	**ADM**	**UPS**
0.05: Absolute number of cells	3285	3476	339	316	43	43
% of Active FS cells	33.52%	35.47%	3.46%	3.22%	0.44%	0.44%
0.1: Absolute number of cells	3285	3476	339	316	43	43
% of Active FS cells	33.52%	35.47%	3.46%	3.22%	0.44%	0.44%
0.15: Absolute number of cells	3285	3476	339	316	43	43
% of Active FS cells	33.52%	35.47%	3.46%	3.22%	0.44%	0.44%
0.221: Absolute number of cells	3285	3476	339	316	43	43
% of Active FS cells	33.52%	35.46%	3.46%	3.22%	0.44%	0.44%
textbf0.3: Absolute number of cells	3285	3476	339	316	43	43
% of Active FS cells	33.52%	35.47%	3.46%	3.22%	0.44%	0.44%

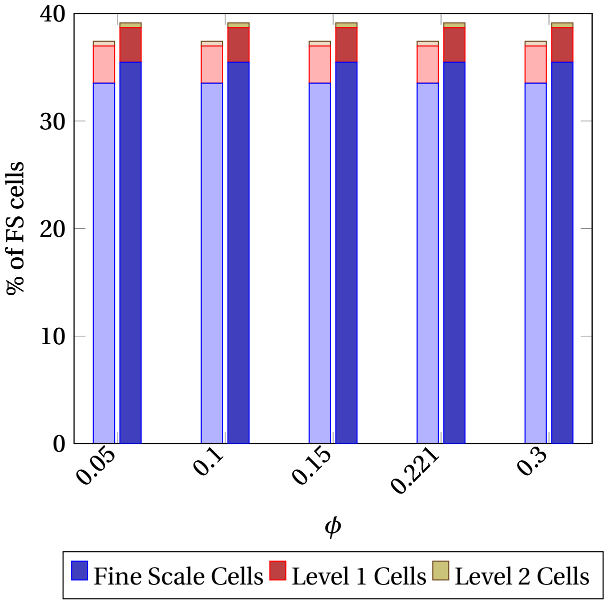

Figure C.1: 15° Permeability field: % of active cells of fine-scale simulation per Level ADM (left bar) vs Upscaling (right bar).

C.2.2. 30° **Permeability field**

Table C.3: Number of cells per level represented in C.2.

Porosity (ϕ)	**FS cells**		**Level 1 cells**		**Level 2 cells**	
	ADM	**UPS**	**ADM**	**UPS**	**ADM**	**UPS**
0.05: Absolute number of cells	3743	3704	300	294	41	43
% of Active FS cells	38.19%	37.792%	3.06%	2.99%	0.42%	0.44%
0.1: Absolute number of cells	3743	3704	300	294	41	43
% of Active FS cells	38.19%	37.79%	3.06%	2.99%	0.42%	0.44%
0.15: Absolute number of cells	3743	3704	300	294	41	43
% of Active FS cells	38.19%	37.79%	3.06%	2.9%	0.42%	0.44%
0.221: Absolute number of cells	3743	3704	300	294	41	43
% of Active FS cells	38.19%	37.79%	3.06%	2.99%	0.42%	0.44%
0.3: Absolute number of cells	3743	3704	300	294	41	43
% of Active FS cells	38.19%	37.79%	3.06%	2.99%	0.42%	0.44%

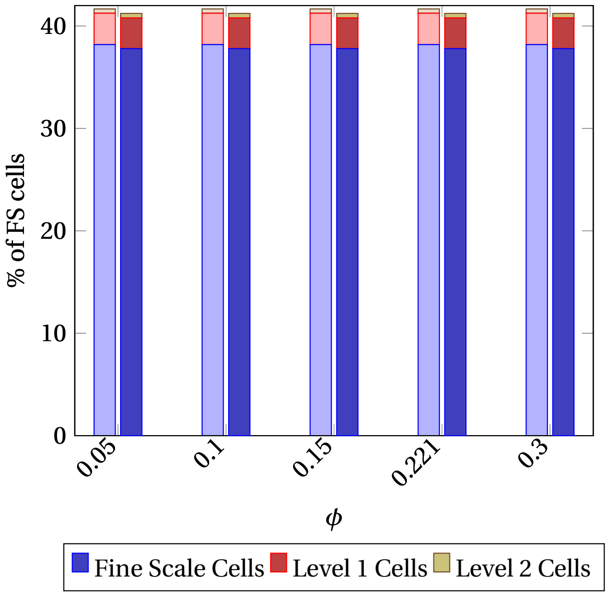

Figure C.2: 30° Permeability field: % of active cells of fine-scale simulation per Level ADM (left bar) vs Upscaling (right bar).

C.2.3. 45° **Permeability field**

Table C.4: Number of cells per level represented in C.3.

Porosity (ϕ)	**FS cells**		**Level 1 cells**		**Level 2 cells**	
	ADM	**UPS**	**ADM**	**UPS**	**ADM**	**UPS**
0.05: Absolute number of cells	4053	3691	270	302	41	42
% of Active FS cells	41.35 %	37.66 %	2.75 %	3.08 %	0.42 %	0.43 %
0.1: Absolute number of cells	4053	3691	270	302	41	42
% of Active FS cells	41.35 %	37.66 %	2.75%	3.08 %	0.42 %	0.43 %
0.15: Absolute number of cells	4053	3691	270	302	41	42
% of Active FS cells	41.35 %	37.66 %	2.75 %	3.08 %	0.42 %	0.43 %
0.221: Absolute number of cells	4053	3691	270	302	41	42
% of Active FS cells	41.35%	37.66 %	2.75 %	3.08 %	0.42 %	0.43 %
textbf0.3: Absolute number of cells	4053	3691	270	302	41	42
% of Active FS cells	41.35 %	37.66 %	2.75 %	3.08 %	0.42 %	0.43 %

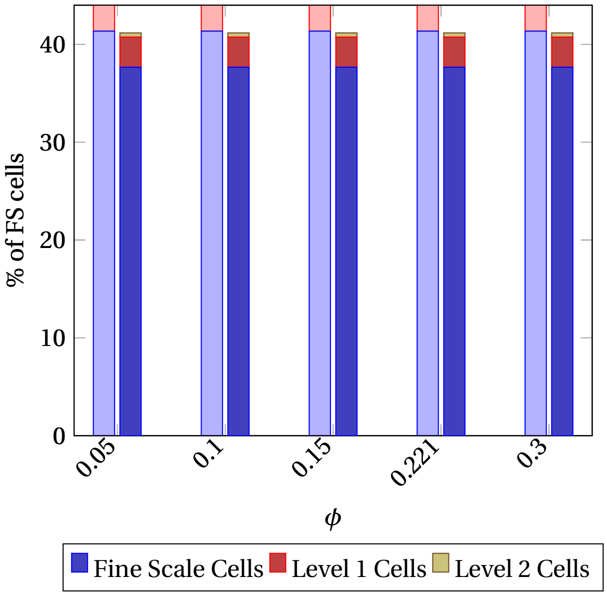

Figure C.3: 45° Permeability field: % of active cells of fine-scale simulation per Level ADM (left bar) vs Upscaling (right bar).

C.2.4. 98° **Permeability field**

Table C.5: Number of cells per level represented in B.4.

Porosity (ϕ)	**FS cells**		**Level 1 cells**		**Level 2 cells**	
	ADM	**UPS**	**ADM**	**UPS**	**ADM**	**UPS**
0.05: Absolute number of cells	3868	3689	276	296	43	43
% of Active FS cells	39.46%	37.64%	2.82%	3.02%	0.44%	0.44%
0.1: Absolute number of cells	3868	3689	276	296	43	43
% of Active FS cells	39.47%	37.64%	2.82%	3.02%	0.44%	0.44%
0.15: Absolute number of cells	3868	3689	276	296	43	43
% of Active FS cells	39.47%	37.64%	2.82%	3.02%	0.44%	0.44%
0.221: Absolute number of cells	3868	3689	276	296	43	43
% of Active FS cells	39.47%	37.64%	2.82%	3.02%	0.44%	0.44%
textbf0.3: Absolute number of cells	3868	3689	276	296	43	43
% of Active FS cells	39.47%	37.64%	2.82%	3.02%	0.44%	0.44%

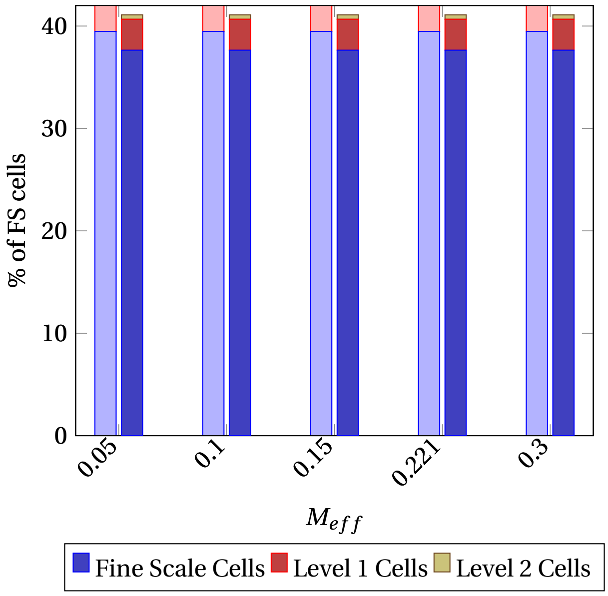

Figure C.4: 98° Permeability field: % of active cells of fine-scale simulation per Level ADM (left bar) vs Upscaling (right bar).

C.3. Pressure & saturation error results

C.3.1. 15° Permeability field

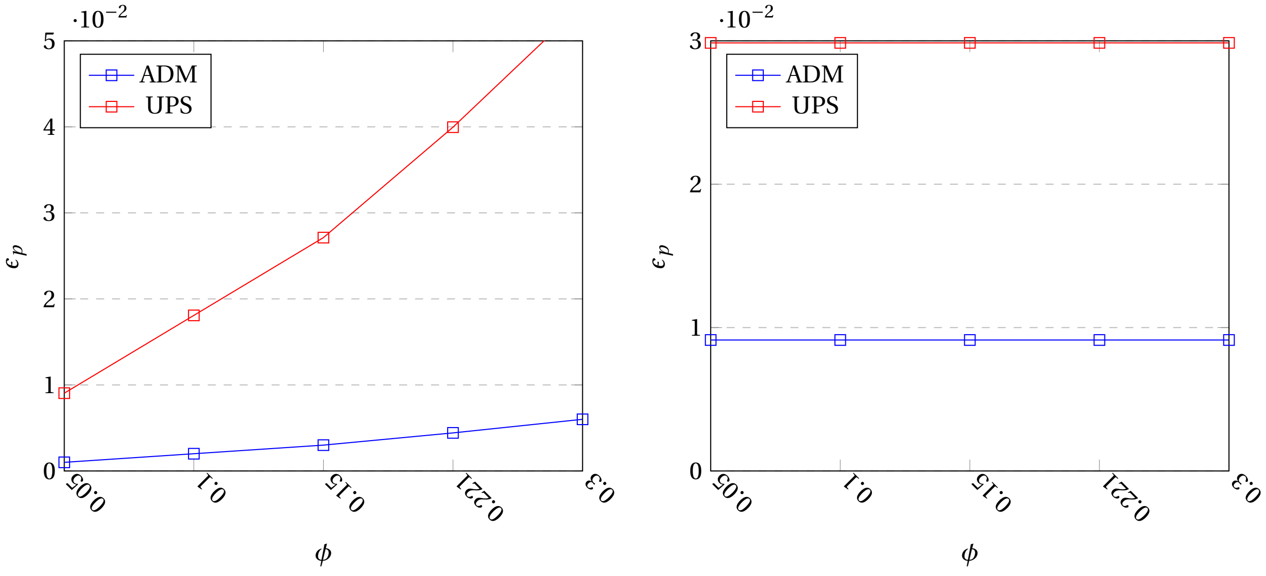

(a) 15° Permeability field: mean error pressure

(b) 15° Permeability field: mean error saturation

Figure C.5: Pressure and saturation error.

C.3.2. 30° Permeability field

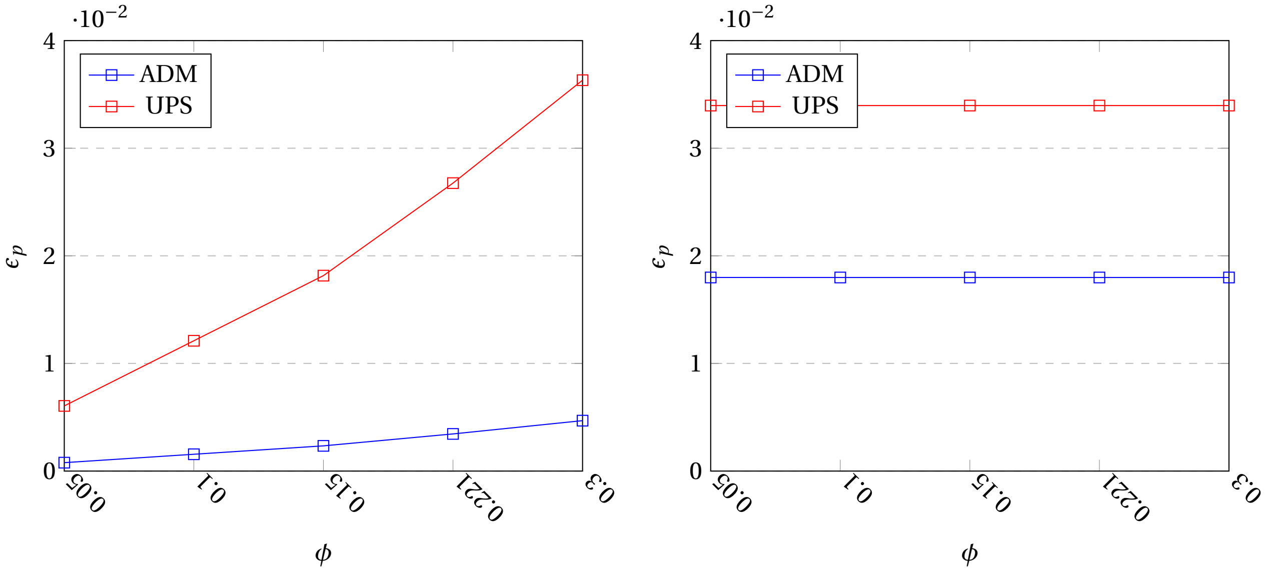

(a) 30° Permeability field: mean error pressure

(b) 30° Permeability field: mean error saturation

Figure C.6: Pressure and saturation error.

C.3.3. 45° **Permeability field**

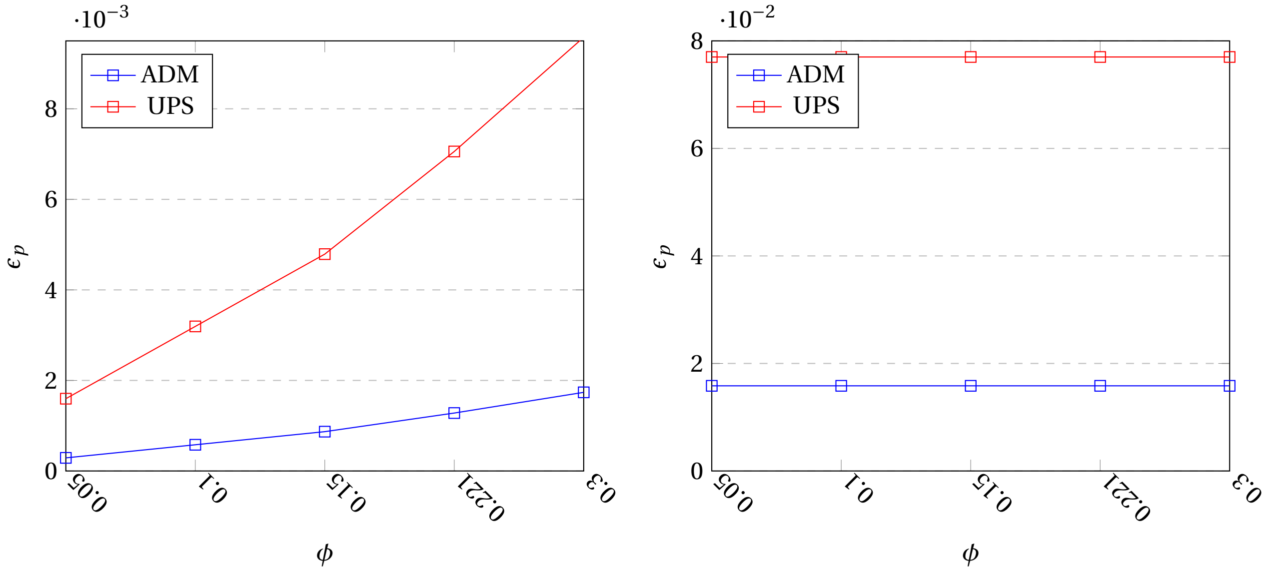

(a) 45° Permeability field: mean error pressure

(b) 45° Permeability field: mean error saturation

Figure C.7: Pressure and saturation error.

C.3.4. 98° **Permeability field**

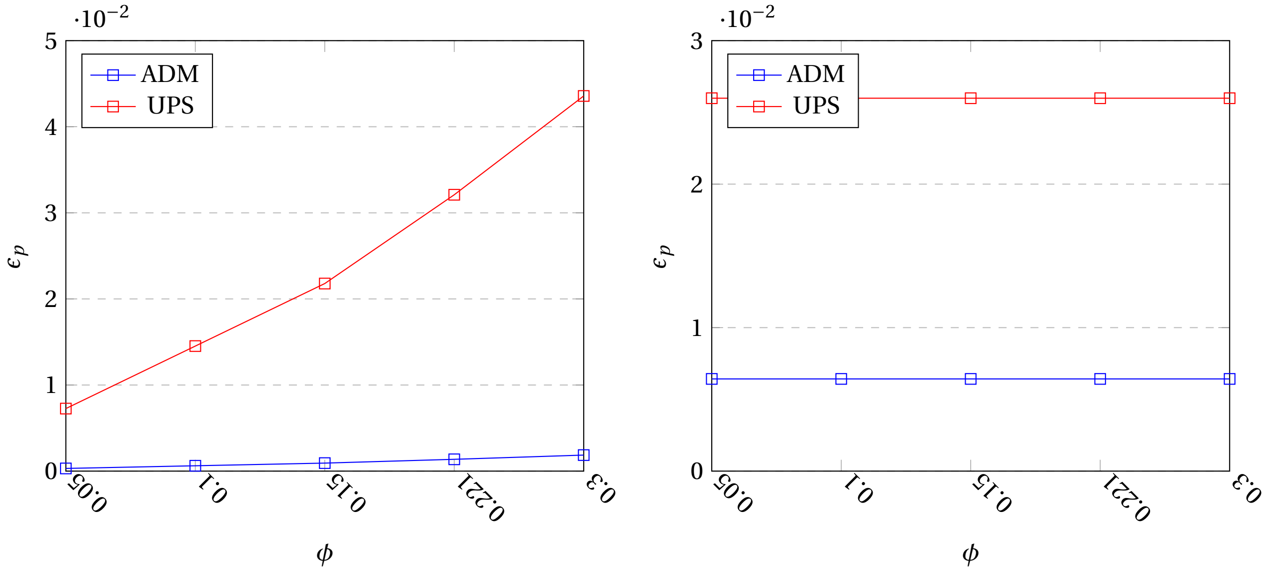

(a) 98° Permeability field: mean error pressure

(b) 98° Permeability field: mean error saturation

Figure C.8: Pressure and saturation error.

C.4. Production error results

C.4.1. 15° & 30° Permeability field

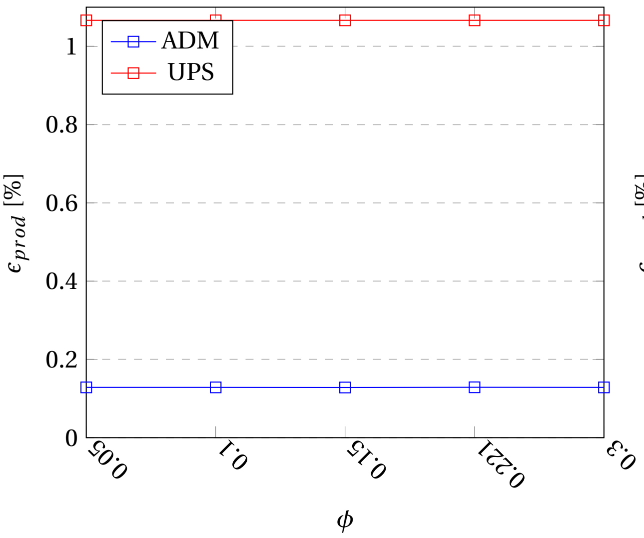

(a) 15° Permeability field: percentual mean error production.

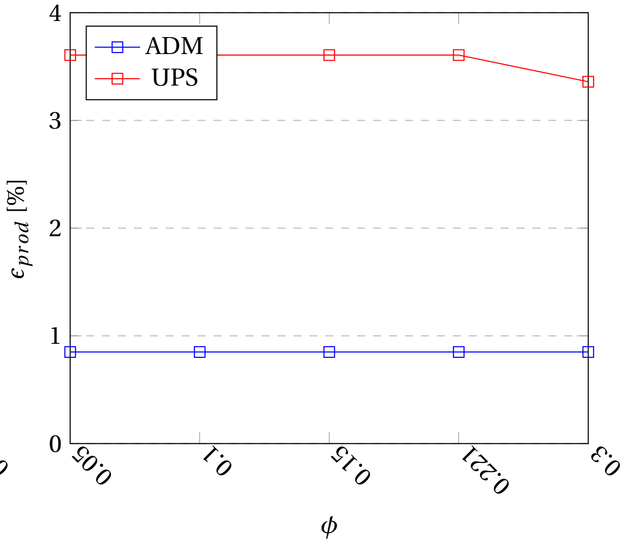

(b) 30° Permeability field: percentual mean error production.

C.4.2. 45° & 98° Permeability field

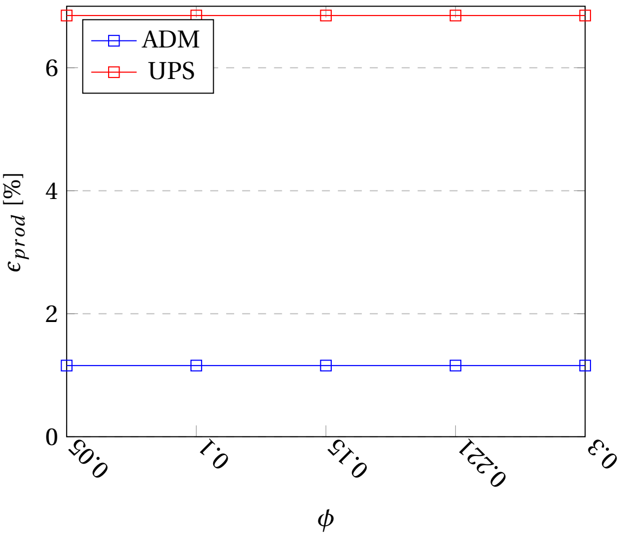

(a) 45° Permeability field: percentual mean error production.

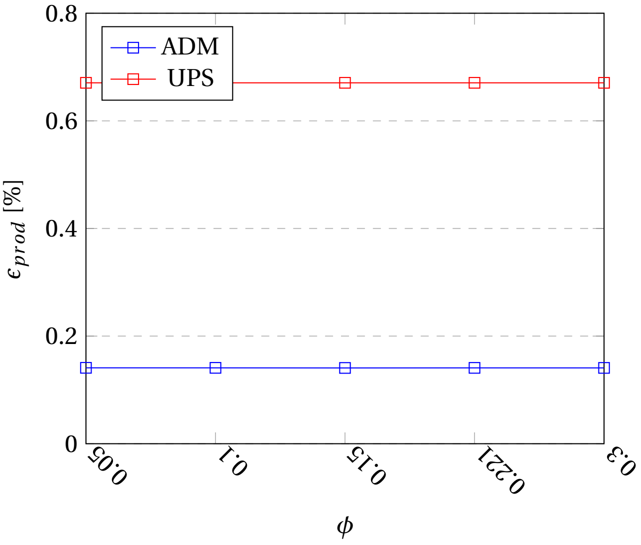

(b) 30° Permeability field: percentual mean error production.

D

Fourth Appendix: Injecting Wetting Phase

D.1. Simulation parameters

Table D.1: Parameters used for simulations.

Variable	**Value**	**Unit**
Temperature: T	323.15	K
Density brine: ρ_{brine}	992	kg/m^3
Viscosity CO_2: μCO_2	$2.3 \cdot 10^{-5}$	$Pa \cdot sec$
Initial Reservoir Pressure: $P_{res,init}$	90	Bar
Initial CO_2 Saturation phase 1	0.0	%
Initial Brine Saturation: S_{brine}	1.0	%
Fine Scale Resolution	99 × 99 × 1	(x,y,z) gridblocks
Level 1 Resolution	33 × 33 × 1	(x,y,z) gridblocks
Level 2 Resolution	11 × 11 × 1	(x,y,z) gridblocks
Simulation Time	12	days
Relative Permeability Curve	Quadratic	
ADM Pressure Interpolator	Multi-Scale	
Upscaling Pressure Interpolator	Constant	
Δ S Tolerance	0.07	
Injection Rate S Tolerance	1.5	Pore-Volumes

D.2. Active Cells ADM versus Upscaled Method

D.2.1. 15° Permeability field

Table D.2: Number of cells per level represented in D.1.

Oil Type	FS cells		Level 1 cells		Level 2 cells	
	ADM	**UPS**	**ADM**	**UPS**	**ADM**	**UPS**
Brent Blend: Absolute number of cells	3738	3722	296	288	42	43
% of Active FS cells	38.14%	37.98%	3.02%	2.94%	0.43%	0.44%
Arabian Medium: Absolute number of cells	3720	3589	284	289	43	44
% of Active FS cells	37.96%	36.62%	2.89%	2.95%	0.44%	0.45%
BCF-17: Absolute number of cells	651	589	222	211	88	90
% of Active FS cells	6.64%	6.01%	2.27%	2.15%	0.90%	0.92%
Boscan: Absolute number of cells	370	364	169	168	97	98
% of Active FS cells	3.78%	3.71%	1.72%	1.71%	0.99%	0.99%

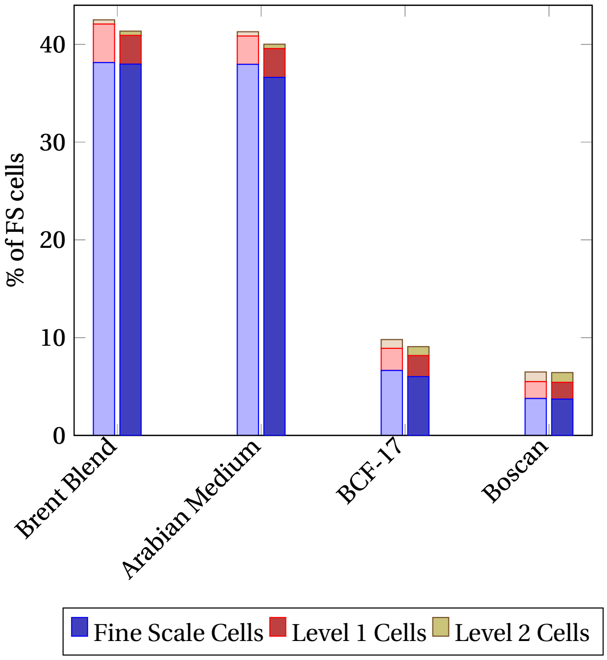

Figure D.1: 15° Permeability field: % of active cells of fine-scale simulation per level ADM (left bar) vs Upscaling (right bar).

D.2.2. 30° **Permeability field**

Table D.3: Number of cells per level represented in D.2.

Oil Type	**FS cells**		**Level 1 cells**		**Level 2 cells**	
	ADM	**UPS**	**ADM**	**UPS**	**ADM**	**UPS**
Brent Blend: Absolute number of cells	3738	3722	296	288	42	43
% of Active FS cells	38.14%	37.98%	3.02%	2.94%	0.43%	0.44%
Arabian Medium: Absolute number of cells	3743	3704	300	294	41	43
% of Active FS cells	37.96%	36.62%	2.90%	2.95%	0.44%	0.45%
BCF-17: Absolute number of cells	651	589	222	211	88	90
% of Active FS cells	6.64%	6.01%	2.27%	2.15 %	0.90%	0.92%
Boscan: Absolute number of cells	3743	3704	300	294	41	43
% of Active FS cells	3.78%	3.71%	1.72%	1.71%	0.99%	0.99%

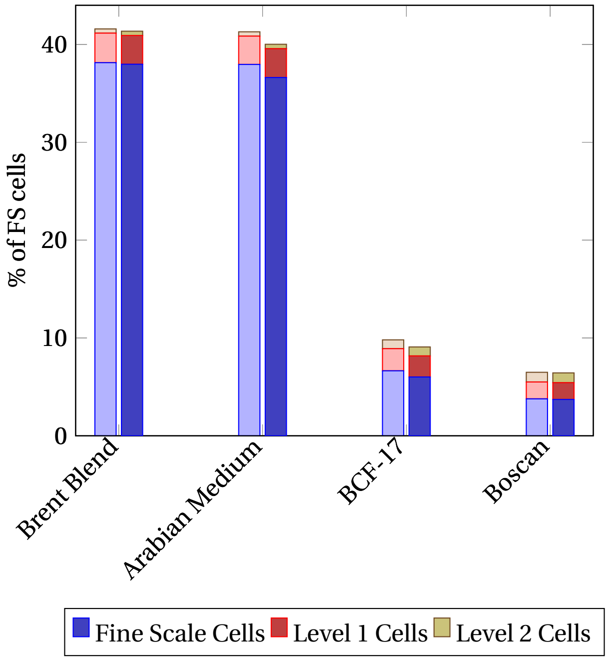

Figure D.2: 30° Permeability field: % of active cells of fine-scale simulation per level ADM (left bar) vs Upscaling (right bar).

D.2.3. 45° Permeability field

Table D.4: Number of cells per level represented in D.3.

Oil Type	FS cells		Level 1 cells		Level 2 cells	
	ADM	**UPS**	**ADM**	**UPS**	**ADM**	**UPS**
Brent Blend: Absolute number of cells	4032	3629	265	303	42	43
% of Active FS cells	41.14 %	37.03 %	2.70 %	3.09 %	0.43 %	0.44 %
Arabian Medium: Absolute number of cells	3927	3504	265	297	43	44
% of Active FS cells	40.07 %	35.75 %	2.70 %	3.03 %	0.44 %	0.45 %
BCF-17: Absolute number of cells	645	611	228	218	88	89
% of Active FS cells	6.581 %	6.23%	2.33 %	2.22 %	0.90 %	0.91 %
Boscan: Absolute number of cells	377	382	173	171	97	97
% of Active FS cells	3.85 %	3.90 %	1.77 %	1.7447 %	0.99 %	0.99 %

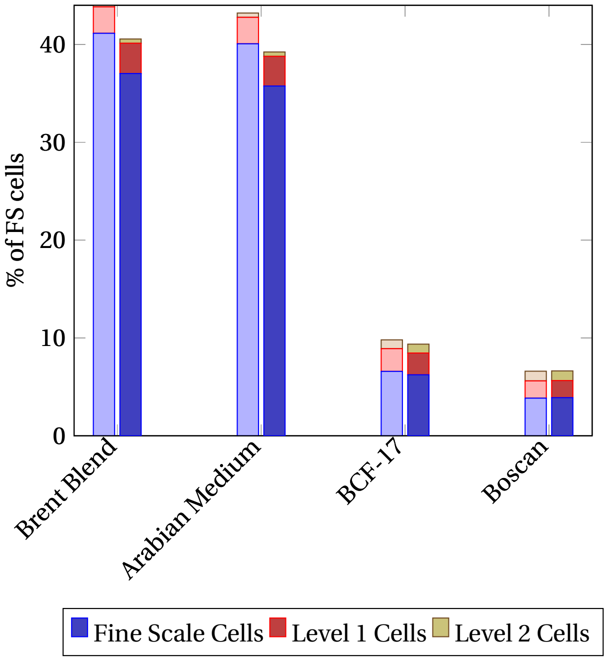

Figure D.3: 45° Permeability field: % of active cells of fine-scale simulation per level ADM (left bar) vs Upscaling (right bar).

D.2.4. 98° **Permeability field**

Table D.5: Number of cells per level represented in D.4.

Oil Type	**FS cells**		**Level 1 cells**		**Level 2 cells**	
	ADM	**UPS**	**ADM**	**UPS**	**ADM**	**UPS**
Brent Blend: Absolute number of cells	3933	3793	260	275	44	44
% of Active FS cells	40.13%	38.7%	2.65%	2.81%	0.45%	0.45%
Arabian Medium: Absolute number of cells	3822	3641	260	282	45	45
% of Active FS cells	38.99%	37.15%	2.65%	2.88%	0.46%	0.46%
BCF-17: Absolute number of cells	663	650	206	207	90	90
% of Active FS cells	6.76%	6.63%	2.10%	2.11%	0.92%	0.92%
Boscan: Absolute number of cells	377	386	167	168	98	97
% of Active FS cells	3.85%	3.93%	1.70%	1.71%	0.99%	0.99%

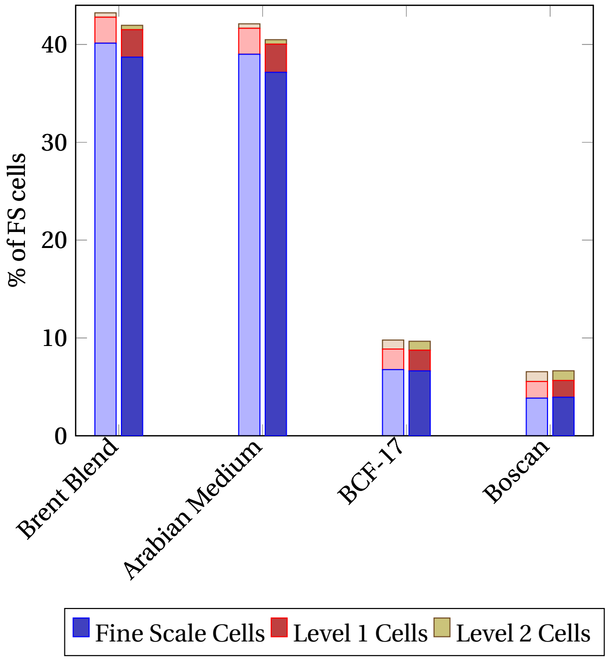

Figure D.4: 98° Permeability field: % of active cells of fine-scale simulation per level ADM (left bar) vs Upscaling (right bar).

D.3. Pressure & saturation error results

D.3.1. 15° Permeability field

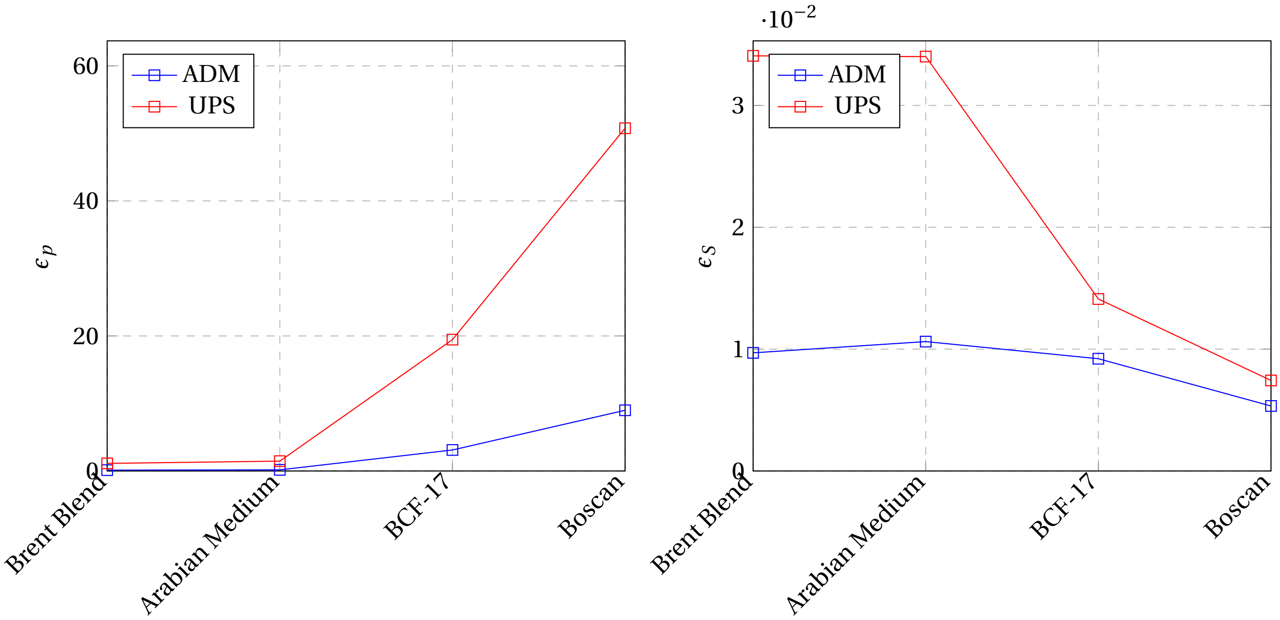

(a) 15° Permeability field: mean error pressure

(b) 15° Permeability field: mean error saturation.

Figure D.5: Pressure and Saturation Error.

D.3.2. 30° Permeability field

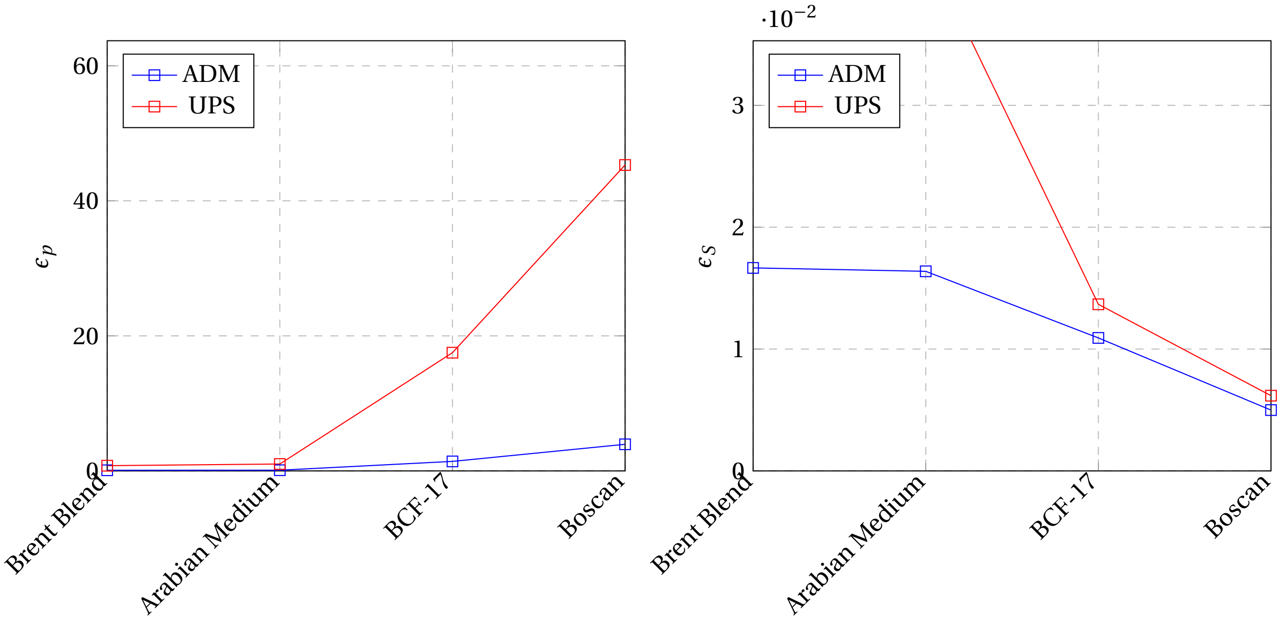

(a) 30° Permeability field: mean error pressure

(b) 30° Permeability field: mean error saturation

Figure D.6: Pressure and saturation error.

D.3.3. 45° Permeability field

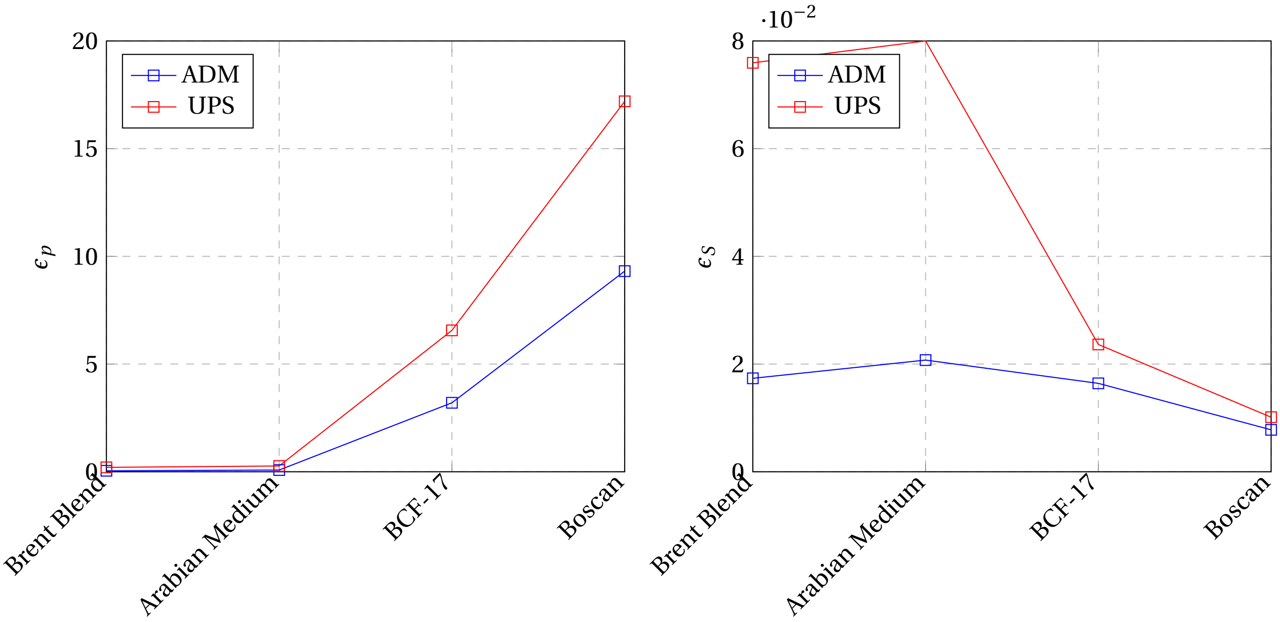

(a) 45° Permeability field: mean error pressure (b) 45° Permeability field: Mean error saturation

Figure D.7: Pressure and saturation error.

D.3.4. 98° Permeability field

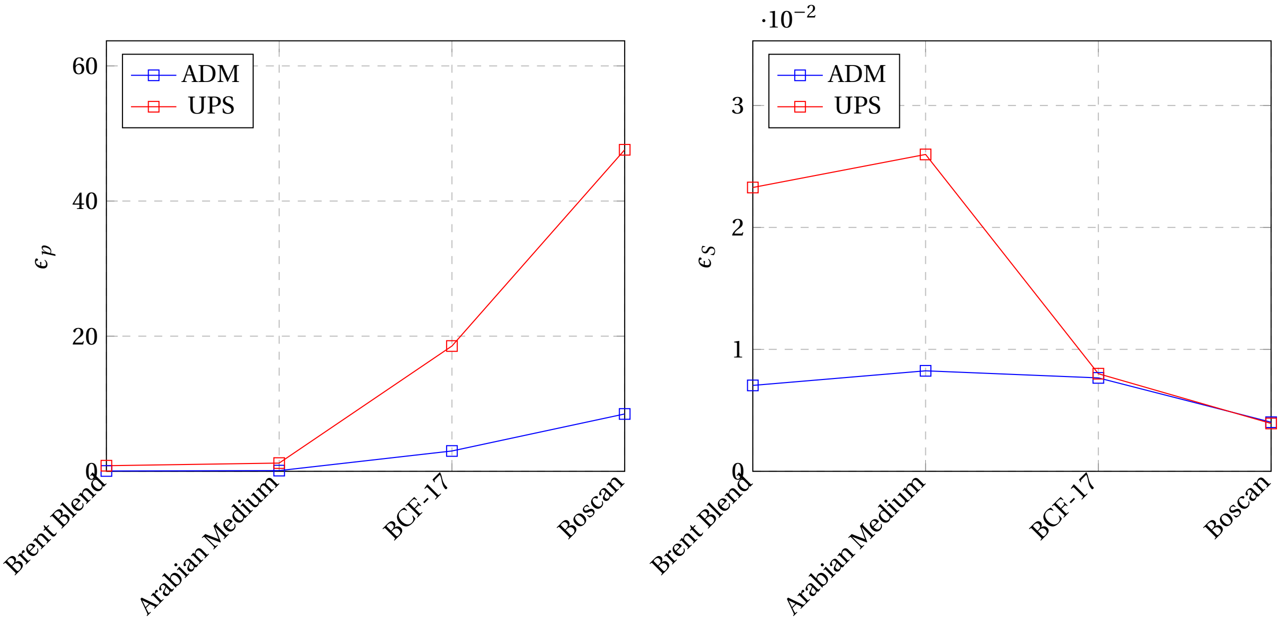

(a) 98° Permeability field: mean error pressure (b) 98° Permeability field: mean error saturation

Figure D.8: Pressure and saturation error.

D.4. Production error results

D.4.1. 15° & 30°

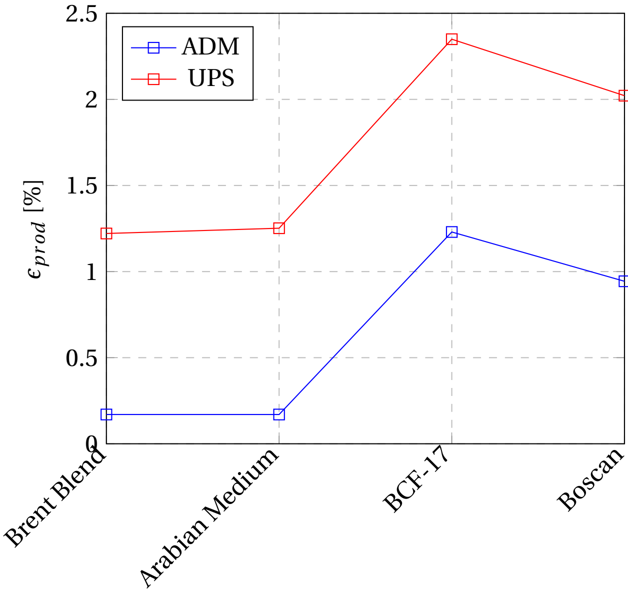

(a) 15° Permeability field: percentual mean error production.

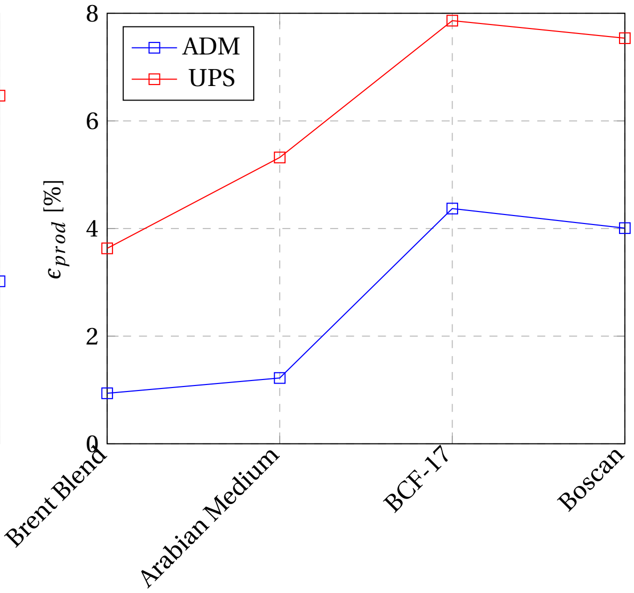

(b) 30° Permeability field: percentual mean error production.

D.4.2. 45° & 98°

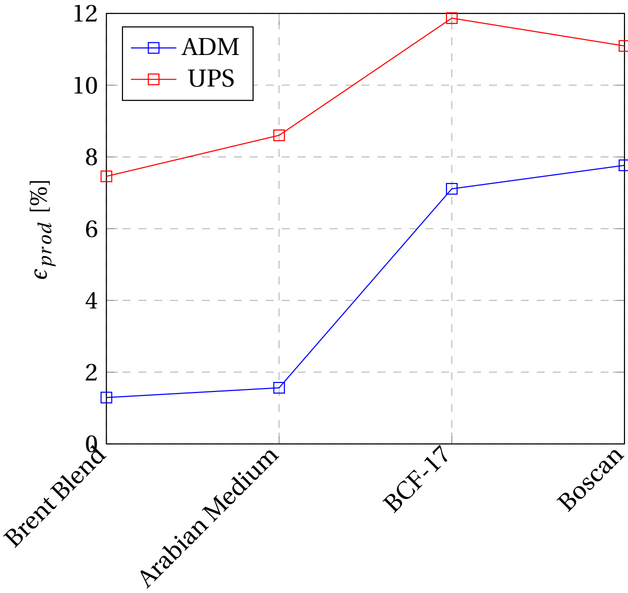

(a) 45° Permeability field: percentual mean error production.

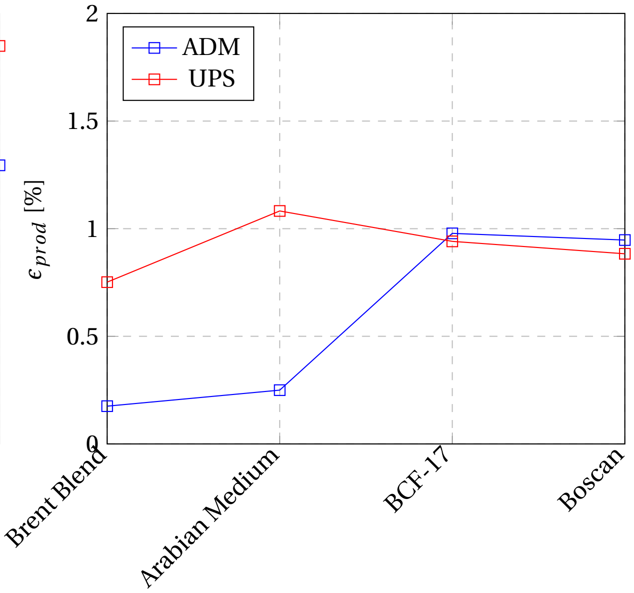

(b) 30° Permeability field: percentual mean error production.

E

Fifth Appendix: Mixing Processes

E.1. Homogeneous medium

E.1.1. Simulation parameters

Table E.1: Parameters used for simulations.

Variable	**Value**	**Unit**
Porosity: ϕ	0.221	volume fraction (%)
Temperature: T	323.15	K
Density CO_2: ρ_{CO_2}	1000	kg/m^3
Density brine: ρ_{brine}	1000	kg/m^3
Viscosity CO_2: μ_{CO_2}	$2.3 \cdot 10^{-5}$	$Pa \cdot sec$
Viscosity brine: μ_{brine}	$5.5 \cdot 10^{-5}$	$Pa \cdot sec$
Initial Reservoir Pressure: $P_{res,init}$	90	Bar
Initial CO_2 Saturation: S_{CO_2}	0.0	%
Initial Brine Saturation: S_{brine}	0.1	%
Simulation Time	800	days
Injection Rate	0.001	PV/day
Relative Permeability Curve	Linear	
ADM Pressure Interpolator	Multi-Scale	
Upscaling Pressure Interpolator	Constant	
Reservoir Dimensions	$1 \times 1 \times 1 (x, y, z)$	m

E.1.2. Active cells

(a) Number of cells per level represented in E.1a.

Δ S Threshold Value	**FS cells**		**Level 1 cells**		**Level 2 cells**	
	ADM	**UPS**	**ADM**	**UPS**	**ADM**	**UPS**
0.03: Absolute number of cells	6109	6033	336	343	8	8
% of Active FS cells	62.33%	61.55%	3.42%	3.49%	0.081%	0.081%
0.07: Absolute number of cells	5899	5762	354	367	9	9
% of Active FS cells	60.18%	58.79%	3.61%	3.74%	0.091%	0.091%
0.1: Absolute number of cells	5797	5630	363	380	9	9
% of Active FS cells	59.14%	57.44%	3.70%	3.87%	0.091%	0.091%

(b) Number of cells per level represented in E.1b.

Δ S Threshold Value	**FS cells**		**Level 1 cells**		**Level 2 cells**	
	ADM	**UPS**	**ADM**	**UPS**	**ADM**	**UPS**
0.03: Absolute number of cells	18614	17563	1178	1206	123	123
% of Active FS cells	47.48%	44.79%	3.00%	3.07%	0.31%	0.31%
0.07: Absolute number of cells	17554	16167	1244	1283	129	142
% of Active FS cells	44.77%	41.23%	3.17%	3.27%	0.32%	0.36%
0.1: Absolute number of cells	16925	15256	1286	1325	132	148
% of Active FS cells	43.17%	38.91%	3.28%	3.37%	0.33%	0.37%

(a) Number of cells per level represented in E.1c.

Δ S Threshold Value	**FS cells**		**Level 1 cells**		**Level 2 cells**	
	ADM	**UPS**	**ADM**	**UPS**	**ADM**	**UPS**
0.03: Absolute number of cells	5770	5723	370	375	9	9
% of Active FS cells	58.87%	58.39%	3.77%	3.82%	0.091%	0.091%
0.07: Absolute number of cells	5453	5352	399	409	9	9
% of Active FS cells	55.63%	54.60%	4.07%	4.17%	0.091%	0.091%
0.1: Absolute number of cells	5288	5168	414	427	10	10
% of Active FS cells	53.95%	52.73%	4.22%	4.35%	0.10%	0.10%

(b) Number of cells per level represented in E.1d.

Δ S Threshold Value	**FS cells**		**Level 1 cells**		**Level 2 cells**	
	ADM	**UPS**	**ADM**	**UPS**	**ADM**	**UPS**
0.03: Absolute number of cells	16501	15676	1260	1294	140	147
% of Active FS cells	42.09%	39.98%	3.21%	3.30%	0.35%	0.37%
0.07: Absolute number of cells	14957	13498	1342	1395	150	162
% of Active FS cells	38.15%	34.43%	3.42%	3.55%	0.38%	0.41%
0.1: Absolute number of cells	14099	11691	1388	1485	156	175
% of Active FS cells	35.96%	29.82%	3.54%	3.78%	0.39%	0.44%

(a) Number of cells per level represented in E.1e.

Δ S Threshold Value	**FS cells**		**Level 1 cells**		**Level 2 cells**	
	ADM	**UPS**	**ADM**	**UPS**	**ADM**	**UPS**
0.03: Absolute number of cells	5787	5776	369	370	9	9
% of Active FS cells	59.04%	58.93%	3.76%	3.77%	0.091%	0.091%
0.07: Absolute number of cells	5133	5111	433	435	10	10
% of Active FS cells	52.37%	52.14%	4.41%	4.43%	0.10%	0.10%
0.1: Absolute number of cells	4737	4695	472	477	10	10
% of Active FS cells	48.33%	47.90%	4.81%	4.86%	0.10%	0.10%

(b) Number of cells per level represented in E.1f.

Δ S Threshold Value	**FS cells**		**Level 1 cells**		**Level 2 cells**	
	ADM	**UPS**	**ADM**	**UPS**	**ADM**	**UPS**
0.03: Absolute number of cells	15777	15705	1273	1276	148	148
% of Active FS cells	40.24%	40.06%	3.24%	3.25%	0.37%	0.37%
0.07: Absolute number of cells	11687	11506	1461	1472	177	178
% of Active FS cells	29.81%	29.34%	3.72%	3.75%	0.45%	0.45%
0.1: Absolute number of cells	9227	8961	1595	1622	193	193
% of Active FS cells	23.53%	22.85%	4.06%	4.13%	0.49%	0.49%

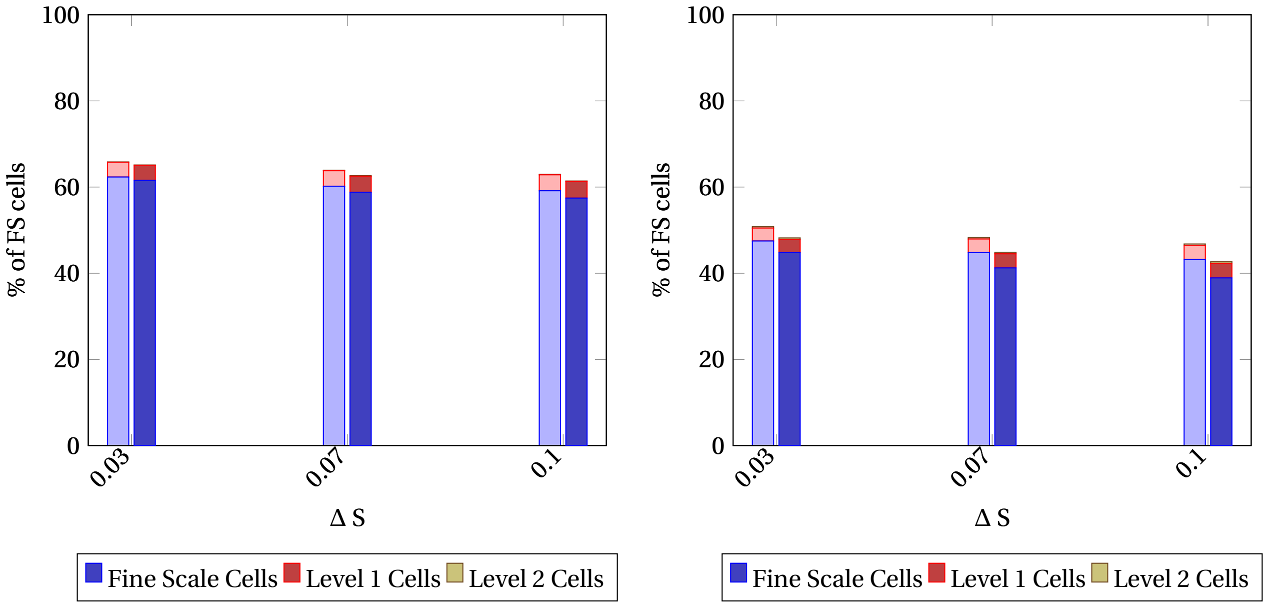

(a) no dispersion 99x99 resolution

(b) no dispersion 198x198 resolution

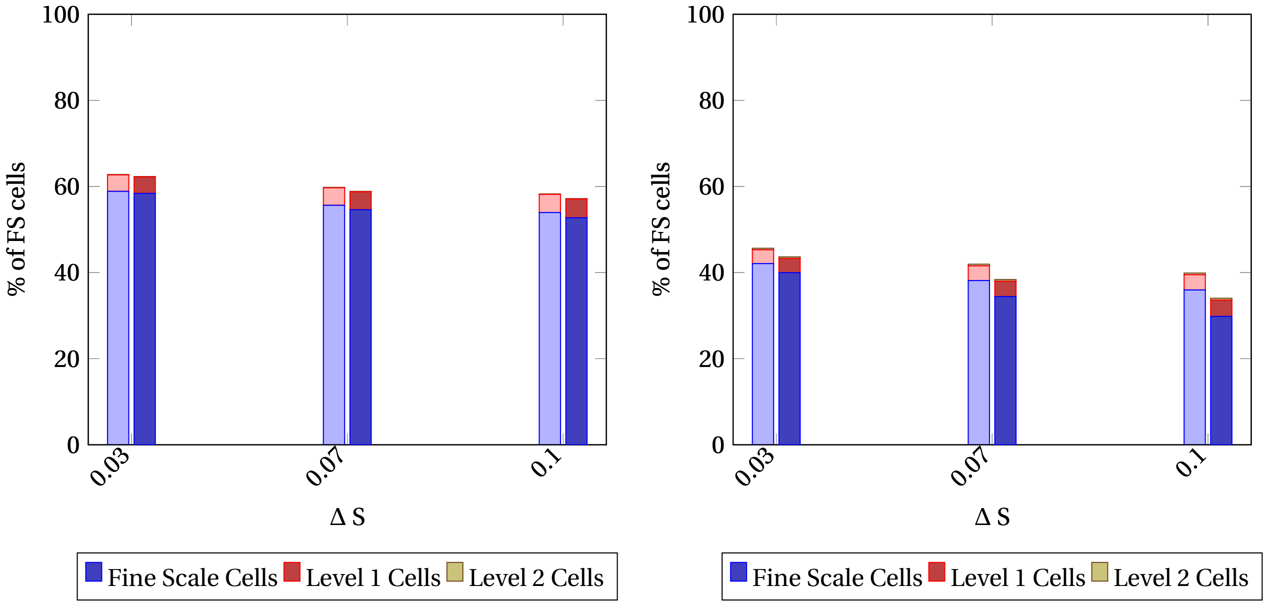

(c) medium dispersion 99x99 resolution

(d) medium dispersion 198x198 resolution

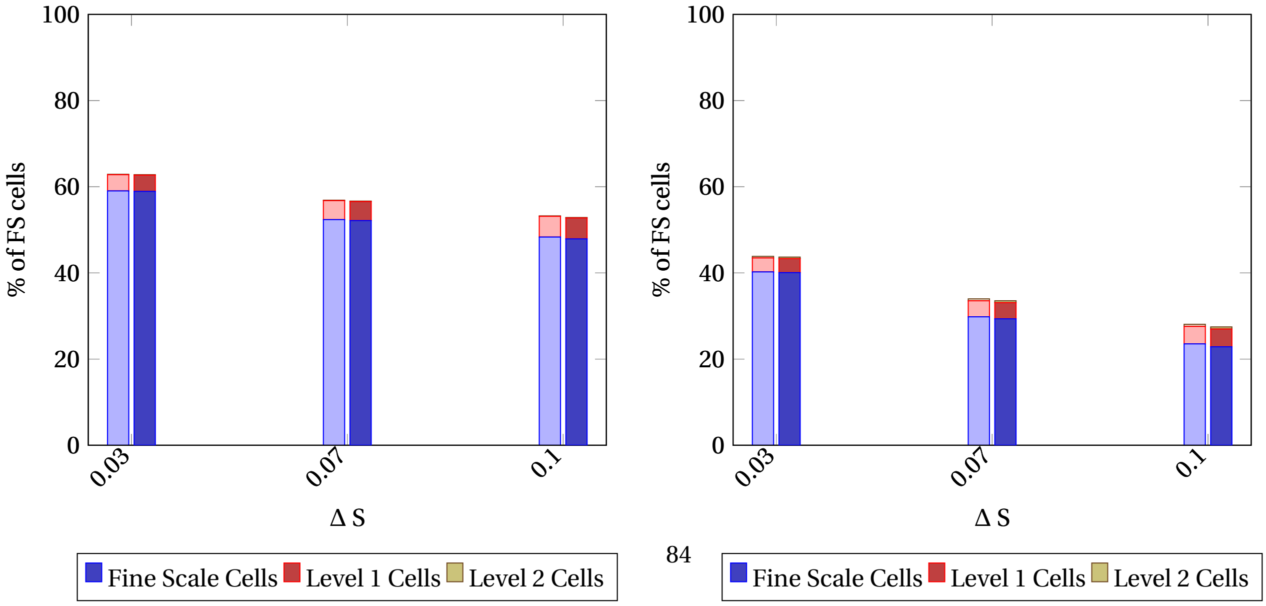

(e) high dispersion 99x99 resolution

(f) high dispersion 198x198 resolution

Figure E.1: % of Active cells of fine-scale simulation per level ADM (left bar) vs Upscaling (right bar).

E.1.3. Pressure & saturation error

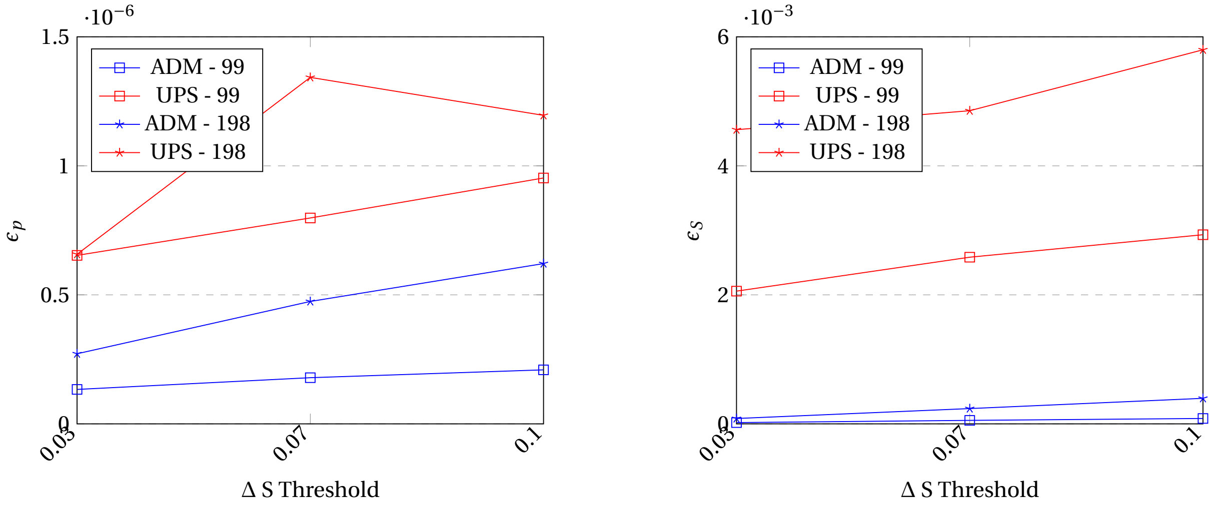

(a) No dispersion: mean error pressure

(b) No dispersion: mean error saturation

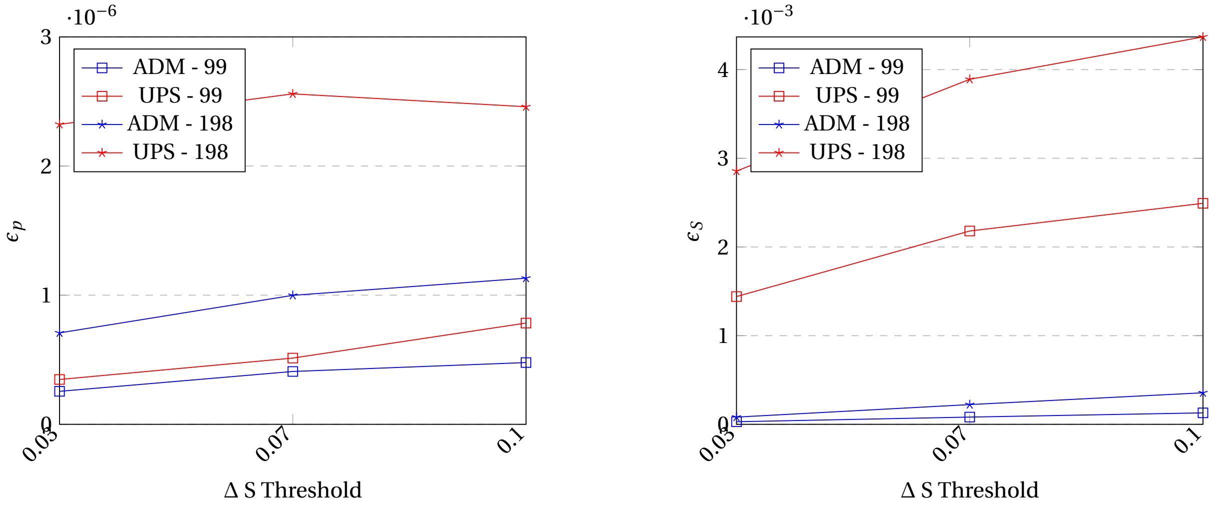

(c) Medium dispersion: mean error pressure

(d) Medium dispersion: mean error saturation

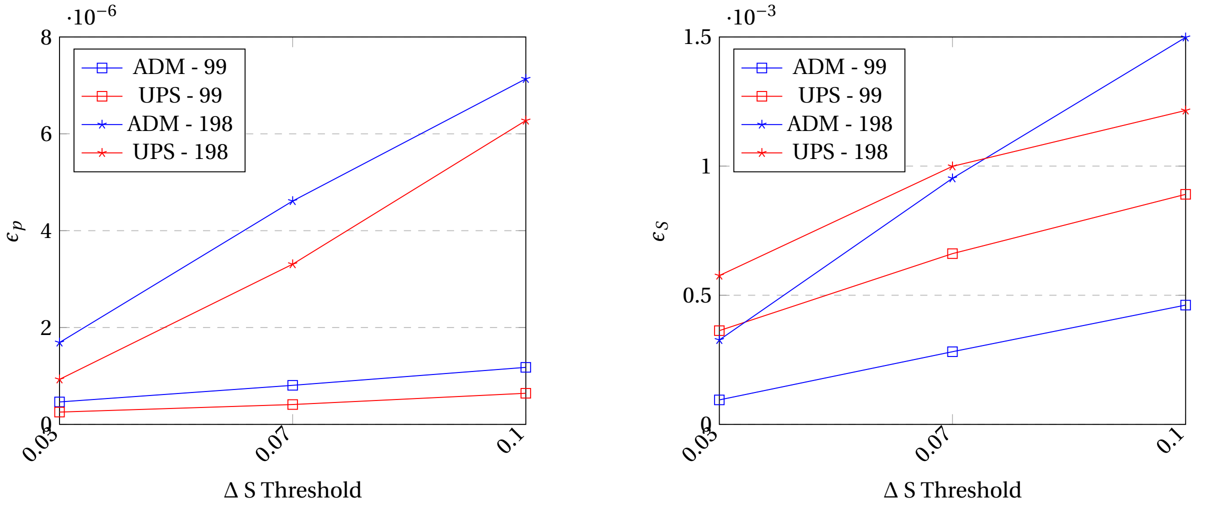

(e) High dispersion: mean error pressure

(f) High dispersion: Mean Error Saturation

Figure E.2: Pressure and saturation error for cases with and without capillarity and decreasing capillary numbers.

E.1.4. Production error

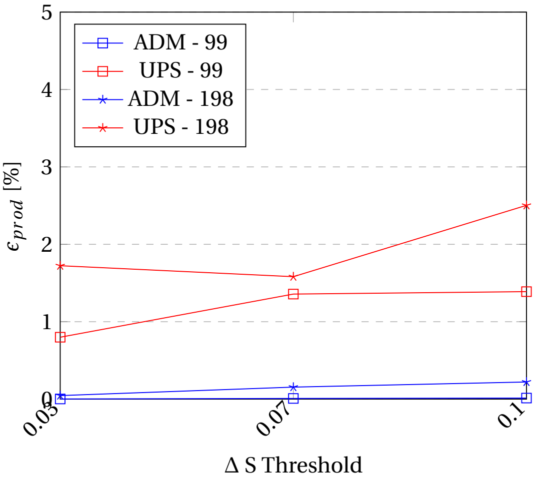

(a) No dispersion: percentual mean error production.

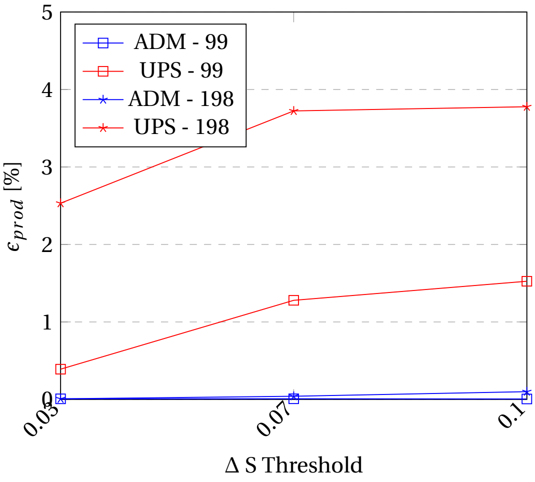

(b) Medium dispersion: percentual mean error production.

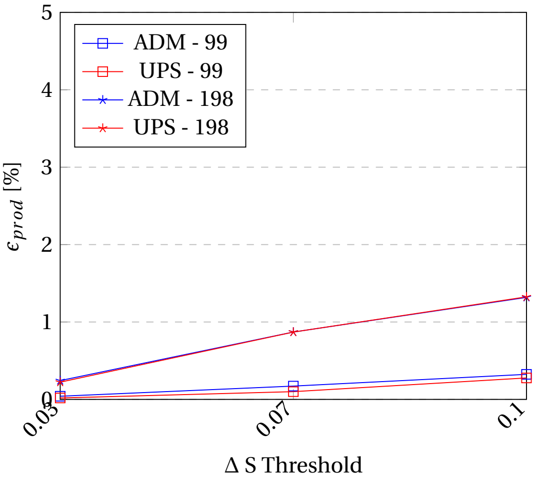

(c) High dispersion: percentual mean error production.

Figure E.3: Percentual mean error production for different resolutions and Péclet numbers

E.2. Heterogeneous medium

E.2.1. Active cells

(a) Number of cells per level represented in E.4a.

Δ S Threshold Value	FS cells		Level 1 cells		Level 2 cells	
	ADM	**UPS**	**ADM**	**UPS**	**ADM**	**UPS**
0.03: Absolute number of cells	17412	17425	588	536	83	88
% of Active FS cells	59.22%	59.26%	2.00%	1.82%	0.28%	0.30%
0.07: Absolute number of cells	15939	16587	689	631	90	88
% of Active FS cells	54.21%	56.41%	2.34%	2.15%	0.31%	0.30%
0.1: Absolute number of cells	15336	15654	758	706	89	91
% of Active FS cells	52.16%	53.24%	2.58%	2.40%	0.30%	0.31%

(b) Number of cells per level represented in E.4b.

Δ S Threshold Value	FS cells		Level 1 cells		Level 2 cells	
	ADM	**UPS**	**ADM**	**UPS**	**ADM**	**UPS**
0.03: Absolute number of cells	20767	20598	542	468	46	57
% of Active FS cells	70.63%	70.05%	1.84%	1.59%	0.16%	0.19%
0.07: Absolute number of cells	19540	19554	647	559	50	59
% of Active FS cells	66.46%	66.50%	2.20%	1.90%	0.17%	0.20%
0.1: Absolute number of cells	19077	18741	705	629	49	62
% of Active FS cells	64.88%	63.74%	2.40%	2.14%	0.17%	0.21%

(c) Number of cells per level represented in E.4c.

Δ S Threshold Value	FS cells		Level 1 cells		Level 2 cells	
	ADM	**UPS**	**ADM**	**UPS**	**ADM**	**UPS**
0.03: Absolute number of cells	21100	21181	531	445	43	52
% of Active FS cells	71.76%	72.04%	1.81%	1.51%	0.15%	0.18%
0.07: Absolute number of cells	20056	19834	627	553	46	57
% of Active FS cells	68.21%	67.46%	2.13%	1.88%	0.16%	0.19%
0.1: Absolute number of cells	19518	19299	683	607	46	57
% of Active FS cells	66.38%	65.64%	2.32%	2.06%	0.16%	0.19%

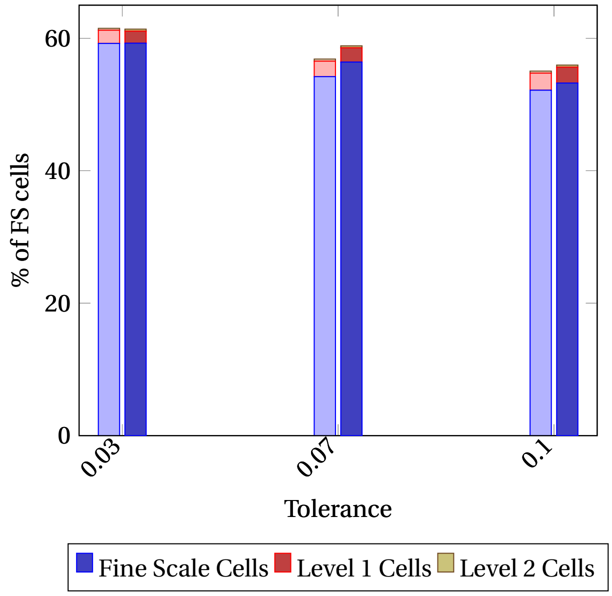

(a) Mixing processes in heterogeneous medium - $Pe = 1000$: % of active cells of fine-scale simulation per Level ADM (left bar) vs Upscaling (right bar).

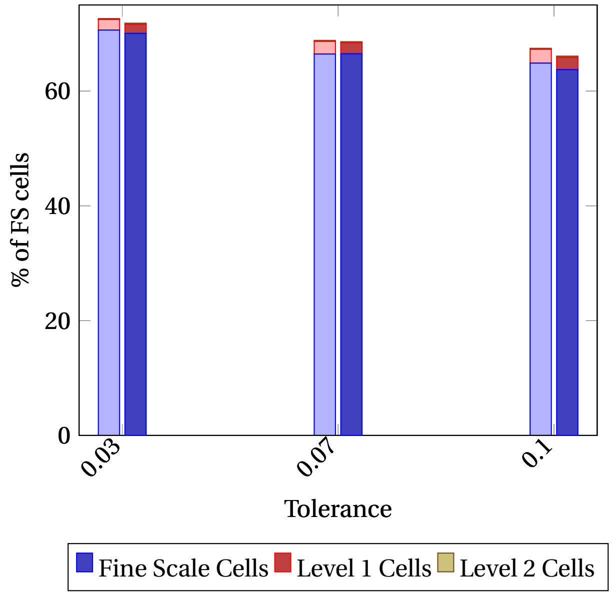

(b) Mixing processes in heterogeneous medium - $Pe = 10.000$: % of active cells of fine-scale simulation per level ADM (left bar) vs Upscaling (right bar).

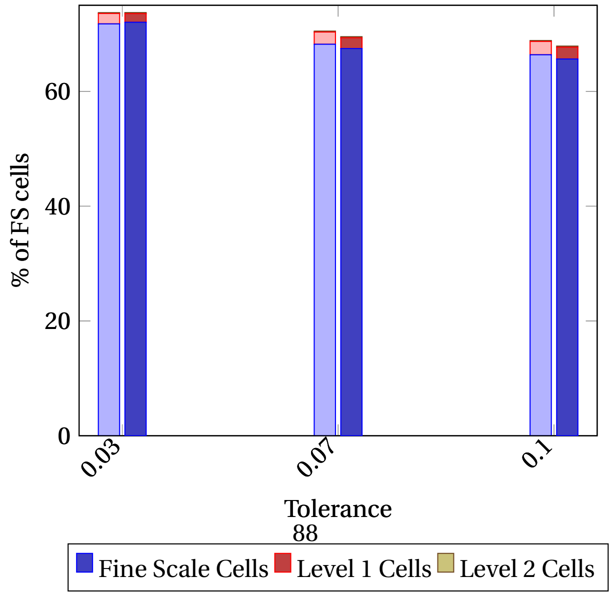

(c) Mixing processes in heterogeneous medium - $Pe = \infty$: % of active cells of fine-scale simulation per level ADM (left bar) vs Upscaling (right bar).

E.2.2. Pressure & saturation error

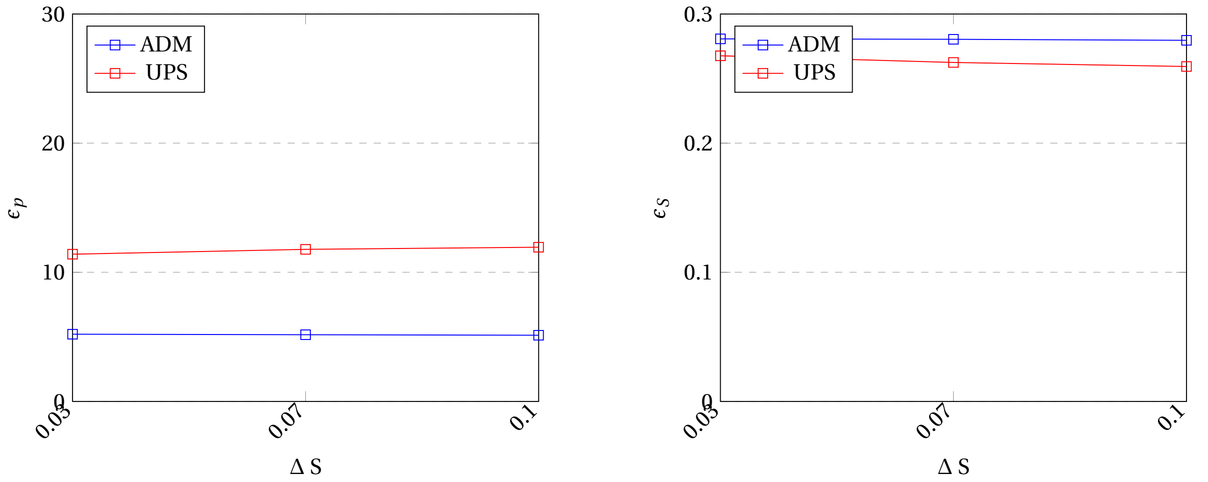

(a) Mixing processes - $Pe = 1000$: mean error pressure (b) Mixing processes - $Pe = 1000$: mean error saturation

Figure E.5: Pressure and saturation error: Pe =1000.

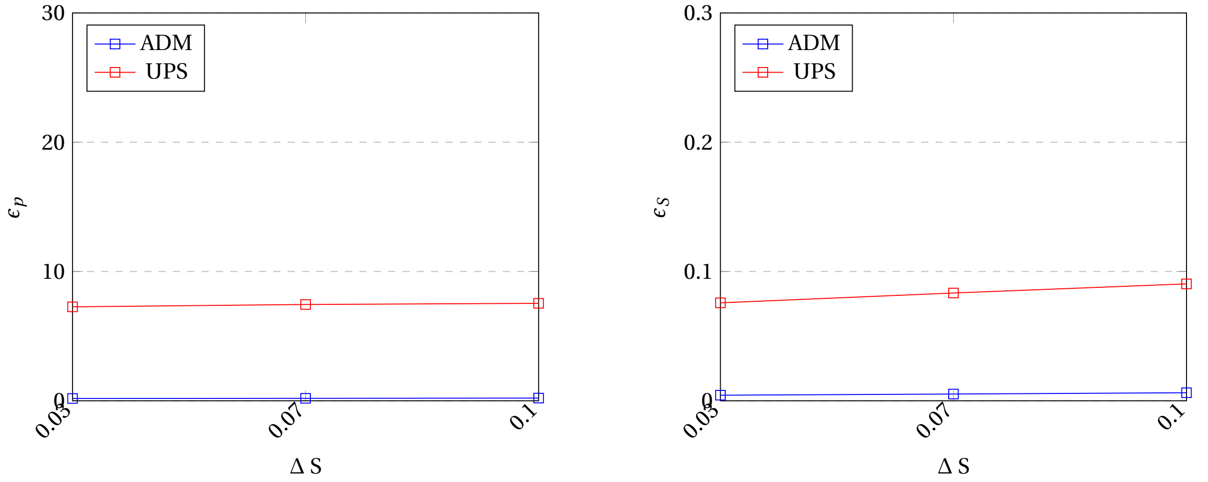

(a) Mixing processes - $Pe = 10.000$: mean error pressure (b) Mixing processes - $Pe = 10.000$: mean error saturation

Figure E.6: Pressure and saturation error: Pe = 10.000.

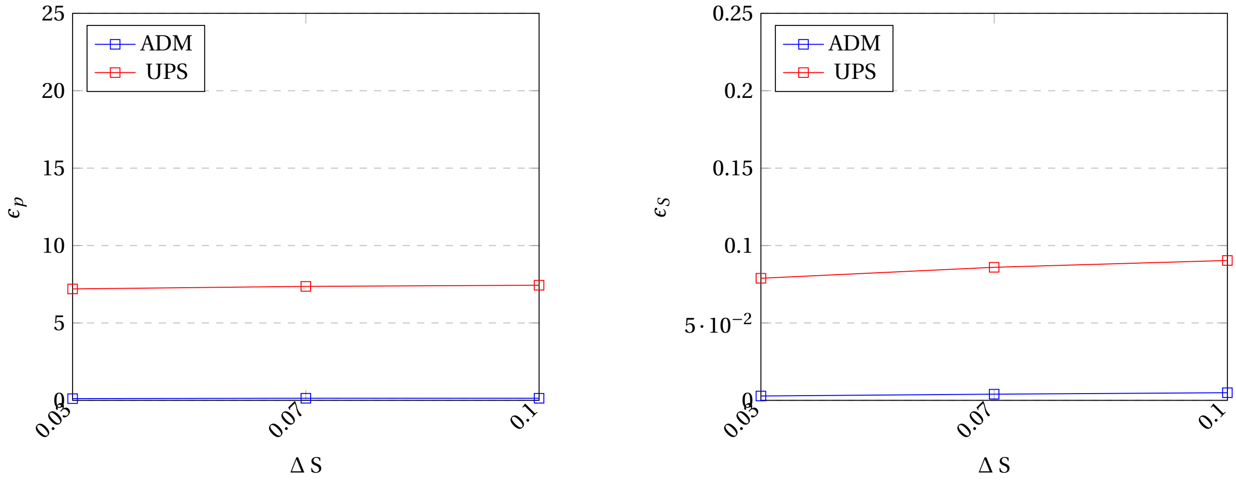

(a) Mixing processes - $Pe = \infty$: mean error pressure (b) Mixing processes - $Pe = \infty$: mean error saturation

Figure E.7: Pressure and saturation error: $Pe = \infty$.

E.2.3. Production error

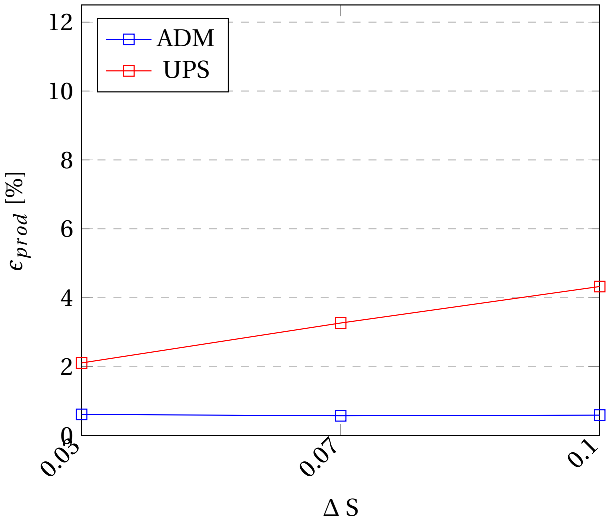

(a) Mixing processes in heterogeneous medium - $Pe = 1000$: percentual mean error production.

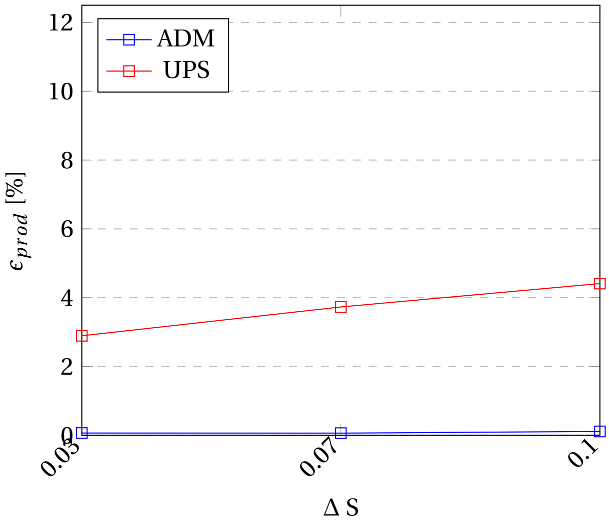

(b) Mixing processes in heterogeneous medium - $Pe = 10.000$: percentual mean error production.

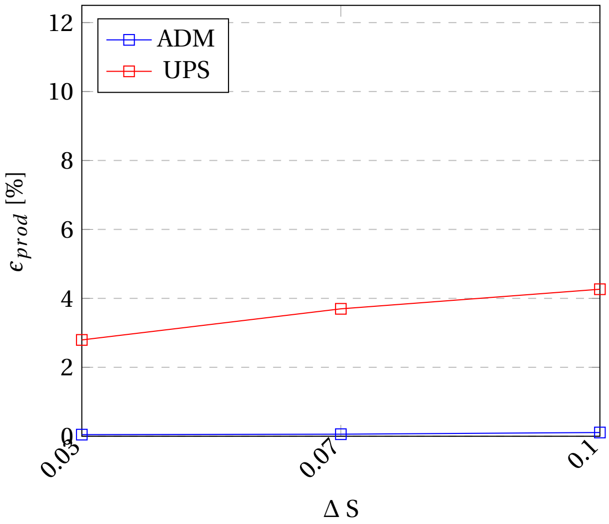

(c) Mixing Processes in heterogeneous medium - $Pe = \infty$: percentual mean error production.